

# Pluto's Volatile and Climate Cycles on Short and Long Timescales

**Leslie A. Young**

*Southwest Research Institute*

**Tanguy Bertrand**

*NASA Ames Research Center*

**Laurence M. Trafton**

*McDonald Observatory, University of Texas at Austin*

**Francois Forget**

*Laboratoire de Météorologie Dynamique (LMD/IPSL), Sorbonne Universités*

**Alissa M. Earle**

*Massachusetts Institute of Technology*

**Bruno Sicardy**

*LESIA, Observatoire de Paris, Université PSL, CNRS, Sorbonne Université,  
Univ. Paris Diderot, Sorbonne Paris Cité*

The volatiles on Pluto's surface, N<sub>2</sub>, CH<sub>4</sub>, and CO, are present in its atmosphere as well. The movement of volatiles affects Pluto's surface and atmosphere on multiple timescales. On diurnal timescales, N<sub>2</sub> is transported from areas of high to low insolation, and the latent heat of sublimation or condensation maintains a nearly isobaric atmosphere. On seasonal (orbital) timescales, Pluto's atmosphere changes its pressure by orders of magnitude, but most models predict that it is unlikely to collapse even at aphelion due to the equatorial N<sub>2</sub> source in Sputnik Planitia and the high thermal inertia of the subsurface. On seasonal timescales, meters of N<sub>2</sub> ice are transported across Pluto's surface, but it is not yet clear from models how much of this transport is between areas which maintain N<sub>2</sub> over an entire year (such as Sputnik Planitia) and to what extent deposition creates new volatile-covered areas (of either N<sub>2</sub>-rich or CH<sub>4</sub>-rich ice) or sublimation reveals underlying terrain. Pluto's orbit and obliquity variations on ~3 Myr timescales (a Milankovitch cycle) induce considerable climate changes along with local accumulation or erosion of m-to-km thick layers of volatile ice. In a non-cyclical process, volatiles filled the large depression that is now Sputnik Planitia.

## 1. Introduction

Much of Pluto's surface and atmosphere can be understood by considering its volatile and climate cycles (e.g., Spencer et al. 1997). Pluto has three volatile ices on its surface and in its atmosphere: N<sub>2</sub>,

CH<sub>4</sub>, and CO. N<sub>2</sub> is the main constituent in Pluto's atmosphere, and is present on large areas of its surface. Unlike Earth, Venus, or Titan, Pluto's main atmospheric constituent is able to condense on its surface. This leads to important interactions between the atmosphere and surface, via relaxation to solid-gas equilibrium. There are similarities with other atmospheres whose main constituent is also solid on the surface: Mars; Triton; Io (e.g., Trafton et al. 1988), to some extent; and probably other volatile-bearing dwarf planets in the Kuiper Belt, at some point in their orbits (e.g., Young et al. 2020). Despite their differences in temperature, surface pressure, composition, and miscibility of the main and secondary constituents, these vapor-pressure-equilibrium atmospheres share three important characteristics. First, because pressure is very sensitive to temperature, and temperature is sensitive to insolation, albedo, and volatile distribution, we find that vapor-pressure-equilibrium atmospheres vary widely over time. For example, the Martian surface pressure varies by ~30% over its year (e.g., Hourdin et al. 1993), while those of Pluto and Triton vary by orders of magnitude (e.g., Trafton et al. 1988). Second, because of latent heat exchanges, sublimation and condensation can make up for energy imbalances between insolation and thermal emission, so there is transport of volatiles keeping a globally near-uniform surface pressure if the atmosphere is thick enough (Leighton & Murray 1966; Trafton & Stern 1983). Third, because the ices are subliming and condensing, they are inherently out of thermodynamic equilibrium. The atmospheres supported by vapor pressure are sensitive to departures of the volatile system from thermal equilibrium, which is otherwise prescribed by the equilibrium phase diagram.

Insolation differences across Pluto's surface are the major driver for the sublimation and condensation of volatiles (See Section 3.1), their transport across Pluto, and the net exchange of volatiles between the surface and atmosphere. The volatile cycle evolves over different timescales. Diurnal sublimation and condensation occurs over Pluto's 6.4-day rotation. Seasonal transport and large pressure changes occur over Pluto's 248-year orbit, made more pronounced by Pluto's large eccentricity of 0.25 and obliquity of 119.6°. The character of its seasonal behavior changes over its ~3 Million year (Myr) Milankovitch-like cycles in the orbit and pole orientation (Dobrovolskis et al. 1997). Finally, Pluto experiences changes over the 4.5 Billion years (Gyr) of solar system history.

These continual cycles of sublimation and condensation of volatile ices induce geological processes such as resurfacing, glacial flow, bladed terrain, and pit formation, and contribute indirectly to dunes of ice and perhaps to the erosion of the water ice bedrock (e.g., on Al-Idrisi, Section 5.2). Because of the volatile cycles, parts of Pluto's surface are among the youngest in the solar system. (See Chapter by Moore and Howard). The volatile cycles also are key drivers of Pluto's atmosphere dynamics, as the condensation and sublimation of N<sub>2</sub> induced winds that strongly impact the general circulation (See Chapter by Forget et al.).

Several properties of Pluto's surface and subsurface affect and complicate the volatile cycles (Section 3). Unlike H<sub>2</sub>O and CO<sub>2</sub> ice on Mars, Pluto's volatile ices (N<sub>2</sub>, CH<sub>4</sub>, CO) mix together to form solid solutions. There is no pure phase for these species on Pluto, owing to their attraction at the molecular level. In thermodynamic equilibrium, the state of Pluto's volatiles thus depends on a ternary phase diagram. Changes in the composition of these mixtures impact the volatile cycles (see Section 3.1). In addition, the ices are contaminated by the accumulation of dark materials from sedimentation of haze particles or from processing of the surface by UV irradiation or energetic particles. N<sub>2</sub> is likely to transition

between its current  $\beta$  crystalline phase to the colder  $\alpha$  crystalline phase on seasonal timescales, affecting its emissivity and other properties (Stansberry & Yelle 1999). New Horizons also revealed that the topography is playing a significant role in the distribution of volatile ice (see Section 3), as  $N_2$ -rich ice is mostly found in the depressions, whereas  $CH_4$ -rich ice has been detected at higher altitude, particularly in the equatorial regions. Finally, climate modeling studies have highlighted how sensitive the sublimation-condensation rates of volatile ices are to the surface albedo, emissivity, thermal inertia, and the solid phase of the ice. These properties of the volatile ices lead to complex interactions between the  $N_2$  and  $CH_4$  cycles involving positive or negative feedbacks between changes of surface properties and sublimation-condensation rates.

A clearer insight into the processes controlling Pluto's volatile cycles can help us understand the complex present-day Pluto, the Pluto of the past, and make testable predictions for Pluto's near future. Models have been used to simulate Pluto's volatile cycles at different timescales, with different levels of simplification.

We review the observations relevant to volatile and climate cycles in Section 2, and cover the basic physics of volatile cycles in Section 3. In Section 4, we review various models, and then present the volatile cycles over diurnal, seasonal, and longer scales in Section 5. We explore open questions and future work in Section 6.

## 2. Observations

### 2.1. Earth-based observations

Observations made by ground-based telescopes, or space-based observatories such as the Hubble Space Telescope (HST), are important for volatile cycles even in the post-flyby era. They provide the setting for the history of work on Pluto's volatile cycles; some observations are only possible from Earth-based telescopes; and telescopic observations are the only means of assessing long-term changes on Pluto.

#### 2.1.1 Albedo and color maps

While New Horizons cameras resolved geological features over much of Pluto's surface, they could not image the southern latitudes that were in darkness during the New Horizons flyby. In addition, because New Horizons was a flyby, it only observed a snapshot in time of Pluto. For changes over decades and for southern coverage, both important for volatile cycles, we turn to maps from Earth-based telescopes or HST, even though their resolutions to date are at best 250 to 500 km per resolution element, or a few resolution elements across Pluto's 2380-km diameter. Buie et al. (1997) reviewed mapping efforts prior to 1996. Buie et al. (2010b) provided important mapping improvements.

The first maps were constructed from the changes in the mean brightness and amplitude of rotational lightcurves since 1954, or from the series of Pluto and Charon transits and eclipses—collectively termed *mutual events*—that occurred within a few years of Pluto's 1987 equinox. (Mutual events also gave the first good constraints on Pluto's radius, e.g.,  $1178 \pm 23$  km when limb darkening is included; Young & Binzel 1994, See Tholen & Buie 1997). Subsequently, Pluto maps were constructed from direct imaging

110 with HST in 1994 and 2002-2003. The most complete analyses from rotational lightcurves was by Drish et al. (1995); from mutual events was by Young et al. (1999, 2001b; Fig 1, left); and from HST maps was by Buie et al. (2010b; Fig 1, right). Pluto's disk was also marginally resolved by modern speckle imaging (Howell et al. 2012), but no maps have been constructed yet from speckle data.

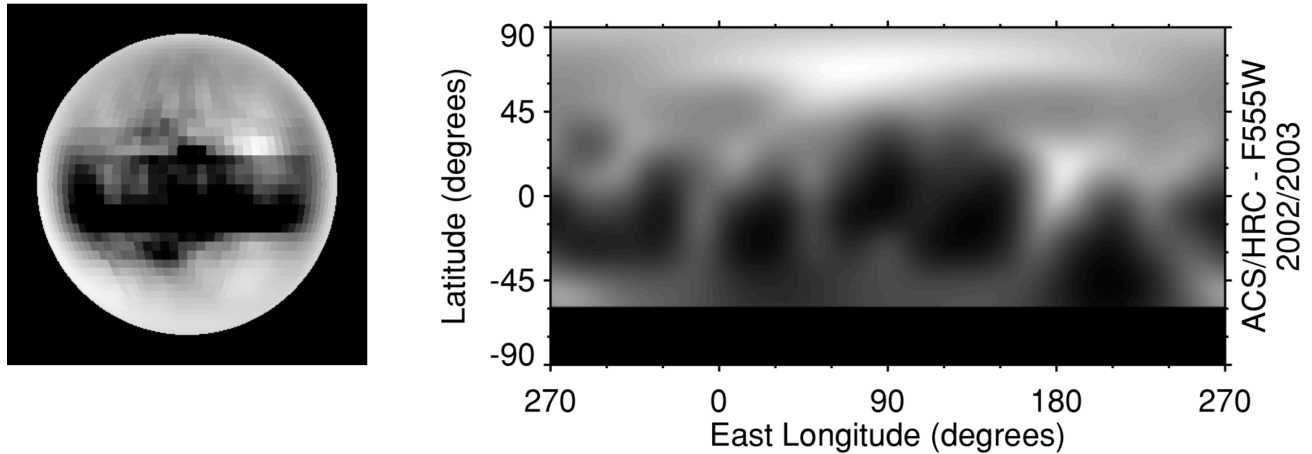


**Fig. 1.** Pre-encounter maps of Pluto. Left: Map of the sub-Charon hemisphere centered on  $0^\circ$  longitude,  $0^\circ$  latitude ca. 1987 (Young et al. 1999). Right: Maps of all longitudes (centered on  $90^\circ$  E), and latitudes north of  $60^\circ$  S, ca. 2002-2003 (Buie et al. 2010).

120 Pluto's changing rotational lightcurve gives clear evidence for a bright southern pole prior to the most recent equinox (Andersson & Fix 1973; Buie & Tholin 1989; Drish et al 1995; Buie et al. 1992). Between 1954 and 1986, when the sub-Earth latitude changed from  $55^\circ$  S to  $3^\circ$  S, Pluto's rotational lightcurve decreased in brightness and generally increased in amplitude, as would occur if a bright and uniform southern pole were seen more directly in 1954 than in 1986, and a variegated darker equator were seen more directly in 1986 than 1954. (The IAU, the New Horizons mission, and many Pluto researchers all now use the rotational north pole, see Zangari 2015.) The conclusion of a bright southern pole depends very little on underlying model assumptions, particularly Pluto's radius. As discussed in Drish et al. (1995), all maps that use the 1954 rotational lightcurve include a bright southern pole. For example, the anti-Charon hemisphere (latitude  $180^\circ$ ) of Buie et al. (1992) is based on rotational lightcurves, and presents a bright southern pole for that hemisphere. Mutual events also showed bright southern terrains on the sub-Charon hemisphere centered at  $0^\circ$  longitude (Young et al. 1999; 2001b; Buie et al. 1992). Some of the bright southern terrains presented in the mutual event maps may be affected by the then-uncertain radii and limb-darkening parameters of Pluto and Charon. For example, the mutual event map of Young et al. (1999) shows brighter albedos near the limb for  $\sim 1/5$  of the projected radius (Fig 1, left), raising concerns about the accuracy of the derived albedos of southern-most latitudes. By the time of the HST observations in 1992 (sub-Earth latitude  $12.7^\circ$  N), the southern polar region was more foreshortened and therefore difficult to image; HST-derived maps for 1992 indicated that the terrains at the southern terminator,  $45^\circ$ S to  $78^\circ$ S, were bright at the sub-Charon hemisphere ( $0^\circ$  longitude), but dark at the anti-Charon hemisphere. The HST observations of 2002-2003 (sub-Earth latitude near  $30^\circ$ N) showed even less of the southern terrains, and similar longitudinal variation at the southern terminator.

130

140 The HST maps and rotational lightcurves suggest changes in Pluto's surface albedo pattern (not just  
 changes due to viewing geometry, as discussed in Buie et al. 2010b). Pluto darkened by 5% between 1933  
 and 1954 in the *B* filter (445 nm); since the sub-Earth latitude was near 53° S for both epochs, this implies  
 real darkening of the southern terrains, not a mere geometric effect (Schaefer et al. 2008). Drish et al.  
 (1995) were unable to make a single static map consistent with rotational lightcurves from 1954 to 1986;  
 in particular, snapshot maps using data 1980-1986 did not show a bright and extended southern cap, but  
 this snapshot included only a 10° change in sub-observer latitude. Buratti et al. (2003) compared rotational  
 lightcurves from 1954 to 1999 with FOC HST maps (Stern et al. 1997), and concluded that lightcurve  
 amplitudes were consistent with a static model; they also noted that the observed 1999 lightcurve was  
 darker than models predict, but they took this as only weak evidence for volatile transport. Buie et al.  
 (2010b) saw evidence for a reddening trend from 2000 through 2002/2003, and darkening in *B* between  
 2002 and 2003, although a static model was consistent with the data in *V* (551 nm) over the year of data  
 150 collection. Buratti et al. (2015) show a decrease in the lightcurve amplitude from primarily 2013  
 observations that were much smaller than predicted from the FOC HST maps. New or newly remeasured  
 photometry now exist from 1930-1951 (Buie & Folkner 2015); 1961-1966 (Eglitis et al. 2018); 1990-  
 1993, 1999, and 2013 (Buratti et al. 2003, 2015). All these datasets can be usefully reassessed, now that  
 radii, orbits, photometric properties (e.g., limb-darkening), and a snapshot of a high-resolution map are  
 better known from the New Horizons encounter.

### 2.1.2 Surface composition and temperature

160 Cruikshank et al. (2015) and the Chapter by Cruickshank et al. review the spectroscopy and  
 composition of Pluto's surface. As with albedo maps, ground-based and HST observations are useful for  
 historical context, for spectral resolution and spectral ranges not reached by New Horizons, and for time  
 variability. Spectra with  $\lambda/\Delta\lambda \sim 350$ , similar to that of LEISA on New Horizons, gave the first evidence  
 for N<sub>2</sub> as a major species, with CO and CH<sub>4</sub> as minor species (Owen et al. 1993). Many of the observations  
 of Pluto's ices have been taken in the near-IR (e.g., Grundy et al. 2013, Cruikshank et al. 2015; Cruikshank  
 et al, this volume), but CH<sub>4</sub> is also detectable at visible wavelengths, which gives a longer timebase of  
 observations (e.g., beginning in 1980, Grundy & Fink 1996). Observations in the mid-IR give constraints  
 on the fraction of pure N<sub>2</sub> ice, the nature of the tholins on the surface, and the mixing state of CH<sub>4</sub> (Olkin  
 et al. 2007). Pre-encounter observations were often of the combined spectra of Pluto and Charon. There  
 are no published spectra that resolve the disk of Pluto (although the potential exists, as the OSIRIS  
 instrument on Keck has resolution comparable to the visible HST maps; Holler et al. 2017). Rather, many  
 programs obtain longitudinal information by observing how the spectrum changes as Pluto rotates  
 170 (Grundy et al. 2013). In Pluto's near-IR spectrum, CH<sub>4</sub> dominates, N<sub>2</sub> is detectable at 2.15 μm, and CO  
 bands are seen at 1.58 and 2.35 μm. H<sub>2</sub>O was not detected pre-encounter (Grundy & Buie 2002). Ethane  
 (C<sub>2</sub>H<sub>6</sub>) and tholins were also detected spectroscopically prior to New Horizons (DeMeo et al. 2010; Olkin  
 et al. 2007). Non-volatiles, such as H<sub>2</sub>O, C<sub>2</sub>H<sub>6</sub>, and tholins, affect the volatile cycles indirectly; while these  
 components are not available for volatile sublimation, the non-volatile surface albedos and temperatures  
 control which areas available for volatile condensation. CO<sub>2</sub>-rich ice has not been detected on Pluto, or

elsewhere in the Kuiper Belt. A near-IR spectrum of Pluto is presented in the Chapter by Cruikshank et al.

180 CH<sub>4</sub>-ice on Pluto is seen to be in two states: diluted in N<sub>2</sub>-rich ice or as CH<sub>4</sub>-rich ice. These can be distinguished in three ways. First, the bands of CH<sub>4</sub> diluted in N<sub>2</sub> are shifted to shorter wavelengths by about 4 to 6 nm in H and K bands compared to pure CH<sub>4</sub> or CH<sub>4</sub>-rich ice (Douté et al. 1999; Protopapa et al. 2015). Second, there is a feature at 1.69 μm that is only present in pure CH<sub>4</sub> ice or CH<sub>4</sub>-rich ice (Douté et al. 1999, Protopapa et al. 2015). Third, the spectrum of dilute CH<sub>4</sub> has a shallower slope from 2.9 to 3.2 μm than pure CH<sub>4</sub>, and presumably shallower than CH<sub>4</sub>-rich ice as well (Olkin et al. 2007).

Modeling of spectra has typically found roughly equal areas of fine-grained CH<sub>4</sub>-rich ice and larger-grained N<sub>2</sub>-rich ice. The amount of CH<sub>4</sub> diluted in the large-grained N<sub>2</sub>-rich ice has been modeled at 0.36% to 0.5% (Douté et al. 1999, Olkin et al. 2007, Protopapa et al. 2008, Merlin et al. 2010). Laboratory work shows N<sub>2</sub> becomes saturated in CH<sub>4</sub>:N<sub>2</sub> ice at ~3% at Pluto temperatures (Prokhvatilov and Yantsevich 1983; see phase diagram in the Chapter by Cruikshank et al.). At these small amounts, the effect of the diluted N<sub>2</sub> is not detectable in the spectrum of the fine-grained CH<sub>4</sub>-rich ice. Although many early papers  
190 (e.g., Douté et al. 1999) refer to areas of “pure CH<sub>4</sub> ice,” spectroscopically, these ices can be either pure CH<sub>4</sub> or CH<sub>4</sub>-rich. Thermodynamic arguments suggest that all the areas described as “pure CH<sub>4</sub>” are actually CH<sub>4</sub>-rich (see Section 3.1.1).

Pluto’s Earth-based disk-integrated spectrum shows a clear variation with sub-solar longitude, including a maximum in the N<sub>2</sub> and CO absorption signature at the longitudes now identified with Sputnik Planitia (e.g., Grundy & Buie 2001; Grundy et al. 2013). Compared to rotational variation, decade-long changes are subtle. To measure how Pluto’s surface changes with time requires monitoring with a consistent instrument and observing procedure to minimize systematic errors, and the careful removal of the rotational signature. Two such programs are Grundy & Fink (1996) and Grundy et al. (2013, 2014). Together, these show a long-term rise in the CH<sub>4</sub> absorption features, and a recent decline in the strength  
200 of the N<sub>2</sub> and CO absorption features. Grundy et al. (2014) argue that these changes are not explained by changes in viewing geometry alone, using pre-encounter albedo and composition maps. Future work is needed to determine if the observed decrease is due to the loss of N<sub>2</sub> and CO ices from the visible hemisphere, preferential sublimation of N<sub>2</sub> and CO in N<sub>2</sub>-rich ice, a change in the surface texture that decreases the absorption band, or if the changes are consistent with the New Horizons composition map and changing viewing geometry only.

The temperature of the N<sub>2</sub>-rich ice is critical for the study of volatile cycles, because the atmospheric surface pressure can be inferred from vapor-pressure equilibrium and the temperature of the N<sub>2</sub> ice. Tryka et al. (1994) report 40±2 K from the temperature-dependent N<sub>2</sub> band, implying pressures of 1.9 to 15.9 Pa (19 to 159 μbar). Certainly, N<sub>2</sub> is in its β crystalline phase. For pure N<sub>2</sub>, this implies a temperature above  
210 the 35.62 K phase transition (0.42 Pa). The temperature of the N<sub>2</sub> phase transition is lowered slightly when diluted with trace CH<sub>4</sub> (Prokhvatilov and Yantsevich, 1983) and raised slightly when diluted with trace CO (Tegler et al. 2019). A sideband of N<sub>2</sub> at 2.162 μm appears at temperatures colder than 41 K, and is apparent in Pluto’s spectrum. Thus, even though a correlation between grain size and temperature complicates temperature retrieval (Grundy 1995), near-IR spectra imply that the temperature of the surface

N<sub>2</sub> ice is between 35.62 and 41 K. This is consistent with the surface pressure observed by the New Horizons radio occultations (see Section 2.2).

In thermal emission, Pluto's brightness temperature is seen to be colder at longer wavelengths (Stern et al. 1993; Jewitt 1994; Sykes et al. 1987; Aumann and Walker 1987; Lellouch et al. 2000, 2011, 2016; Butler et al. 2019), which is explained by a combination of Pluto's variegated terrain and a wavelength-dependent spectral emissivity (Lellouch et al. 2011, 2016). Data from ISO, Spitzer, and Herschel measured Pluto's thermal emission across its emission peak, near 100  $\mu\text{m}$ . These data show rotational variation, with colder brightness temperatures at 180° E to 240° E, the longitudes associated with bright albedos and N<sub>2</sub> absorption (Lellouch et al. 2000, 2011, 2016). These measurements imply N<sub>2</sub> temperatures near 37 K, and low thermal inertia values within the diurnal skin depth (i.e., the uppermost few cm) for the CH<sub>4</sub>-rich and volatile-free terrains of  $\sim 20\text{-}30 \text{ J m}^{-2} \text{ s}^{-0.5} \text{ K}^{-1}$  (hereafter  $\tau_{\text{th}}$ , for thermal inertial units, as introduced by Putzig 2006). The low thermal inertia implies a porous structure for the top few cm, which are affected by the diurnal temperature cycle. As with albedo and IR spectra, decade-long changes in thermal emission are much more subtle than rotational changes. Observations were taken prior to equinox and perihelion at  $\sim 100 \mu\text{m}$  (Sykes et al. 1987; Aumann and Walker 1987) and at mm/sub-mm (Stern et al. 1993, Jewitt 1994), but these were not rotationally resolved. Models based on pre-encounter composition maps were able to match ISO and Spitzer data with static composition maps and thermophysical parameters of bolometric Bond albedo, emissivity, and thermal inertia that were static from 1997 to 2004 (Lellouch et al. 2011). Hints of change between 2004 and 2007 (Lellouch et al. 2011) were not supported by later data from 2012 (Lellouch et al. 2016). No further observations of Pluto near its emission peak have been made since 2012, although observations at 0.8 mm to 0.9 cm have been taken from ALMA, SMA, and VLA (Butler et al. 2020).

### 2.1.3 Atmospheric structure, composition, and variation

Stellar occultations observed from Earth have proven to be a powerful technique to probe the changes in Pluto's atmosphere over the span of decades, occasionally at high spatial resolution. Stellar occultations are more sensitive than near-IR spectra for detecting changes in N<sub>2</sub>-ice temperature (under the assumption of vapor-pressure equilibrium). More information can be found in the Chapter by Summers et al. Stellar occultations work as follows: The differential refraction of stellar rays causes a drop of flux which can be used to retrieve the vertical refractivity profile of the atmosphere via an inversion technique for observations with high enough cadence and signal-to-noise ratio. Assuming a composition (a predominately N<sub>2</sub> atmosphere in the case of Pluto), plus the ideal gas law and hydrostatic equilibrium, local profiles of density, pressure and temperature can be derived (see e.g. Vapillon et al. 1973; Elliot & Olkin 1996; Elliot, Person & Qu 2003), often at a vertical resolution of a few km or better. For lower quality light curves, typically a temperature and pressure at a reference altitude can be derived through forward modeling.

Due to refraction effects, the deepest atmospheric layers accessible to ground-based occultations of Pluto do not reach the surface, but probe the atmosphere down to typically 10-20 km altitude (pressure  $\sim 1$  Pa). For high quality light curves, levels up to 380 km altitude ( $\sim 1$  mPa) can be probed.

Pluto’s atmosphere was first glimpsed during a stellar occultation in 1985 (Brosch 1995) and fully recognized as such after a high-quality occultation was observed by multiple sites in 1988 (Hubbard et al. 1988; Elliot et al. 1989). Beginning in 2002, Pluto started to move in front of the Galactic center, increasing the rate of successful events to a few per year.

260 As of 2016, more than 20 stellar occultations by Pluto have been documented (Young 2013; Bosh et al. 2015; Meza et al. 2019; Desmars et al. 2019). Some occultations had sufficient quality to provide a good assessment of the global pressure changes over time. For instance, an occultation observed in 2002 showed that Pluto’s atmosphere underwent an increase in pressure by a factor of about two between 1988 and 2002 (Elliot et al. 2003, Sicardy et al. 2003). This increase was confirmed as more occultations were observed (Elliot et al. 2007, Olkin et al. 2015, Sicardy et al. 2016). As Pluto had continuously receded from the Sun since its perihelion in 1989, clearly, more complex effects were at work besides heliocentric distance (see Section 4.2).

270 Studies of the changes in Pluto’s climate were confounded by a fundamental uncertainty in the nature of Pluto’s lower atmosphere, and by differences in analysis technique (see Bosh et al. 2015 for a review of these complications). The first complication is that Pluto’s radius was not directly measured until the New Horizons flyby of 2015 (as noted, stellar occultations do not probe to Pluto’s surface). Occultation work prior to the flyby performed presented results as a function of radius (distance to Pluto center) rather than altitude (distance to Pluto surface). A second complication is the unknown cause of the low fluxes reached by the occultation lightcurves, corresponding to the lower tens of km in Pluto’s atmosphere, affecting fluxes below half-light in 1988 or roughly quarter-light in 2002 and beyond (that is, the portions of the lightcurve where the stellar flux is less than half or a quarter of its unocculted value). While the upper portions of the lightcurves were well described by a clear atmosphere with at most a small thermal gradient, the lower fluxes were modeled as caused by haze absorption (“haze/no-steep-gradient”; Elliot et al. 1989), a steep thermal gradient below ~1215 km radius (“clear/steep-gradient”; Hubbard et al. 1990; Elliot et al. 2003; Dias-Oliveira et al. 2015), or a hybrid.

280 One solution to the haze/thermal-gradient puzzle is to focus on only the upper portions of the lightcurve, sidestepping the haze/gradient question. Even this is problematic, as described by Bosh et al. (2015). By one measurement—the radius in Pluto’s shadow at which the stellar flux drops to half its unocculted value—the large increase between 1988 and 2002 had effectively leveled off after 2002 (Bosh et al. 2015). By another measurement—a 2- or 3-parameter model of pressure and temperature and optional (small) thermal gradient at a reference radius (typically 1275 km), fit to only the upper portions of the lightcurve—the pressure has increased steadily at 3.5% to 7.5% per year since 1988 (Bosh et al. 2015; Olkin et al. 2015).

290 Other approaches look for changes using the entire lightcurve. For very high-quality data, the lightcurve can be inverted to derive temperature, pressure, and density vs. radius, under the assumptions of a clear N<sub>2</sub>-atmosphere and hydrostatic equilibrium (e.g., Elliot, Person & Qu 2003; Sicardy et al. 2003; Young et al. 2008). For data of high or moderate quality, Elliot and Young (1992) developed a 6-parameter model that included the 3 upper-atmosphere parameters describing (i) temperature, (ii) a small temperature gradient, (iii) a reference pressure, plus 3 parameters describing a haze with (iv) an onset radius, (v) an onset absorption coefficient, and (vi) a haze scale height. This “EY92” model was applied to many

300 observations from 1988 and beyond (Elliot & Young 1992; Young et al. 2008; Gulbis et al. 2015). While the EY92 model matched the shape of many lightcurves, it failed to reproduce the central flash sometimes observed near the center of Pluto's shadow, and did not allow for the ~60 K drop in temperature from the upper atmosphere to a surface near 40 K (see below). Other researchers (Hubbard et al 1990; Zelucha et al. 2011) constructed thermal profiles from physically motivated radiative-conductive models, dependent on the surface radius (again, this was unknown before the New Horizons flyby) and CH<sub>4</sub> or CO mixing ratios. A difficulty with applying physically motivated models is that the energetics of Pluto's atmosphere is not well understood (see the Chapter by Summers et al.).

310 A promising approach is the technique of fitting with a temperature template, which has several advantages: it uses the entire lightcurve, it can describe even the central portions of the occultation lightcurve (unlike the EY92 model), and it does not rely on an accurate understanding of Pluto's atmospheric energy balance. Dias-Oliveira et al. (2015) constructed a temperature template from a high-quality occultation light curve, which was able to be fit to various occultation events assuming no significant haze absorption (Fig 2). The template includes a steep thermal gradient below ~1215 km; a maximum near 1215 km; and a mild negative gradient of  $dT/dr = -0.2 \text{ K km}^{-1}$  between 1215 and 1390 km. Above 1400 km, the temperature is poorly constrained, and the template adopts an isothermal upper atmosphere at  $81 \pm 6 \text{ K}$ . The shape of the temperature template is shown in Dias-Oliveira et al. 2015, their Fig 13. This 10-parameter temperature-template model (9 temperature parameters plus a reference pressure) gives a good agreement between the pressures derived from Earth in 2015 (Sicardy et al. 2016, Meza et al. 2019) and from the REX experiment on-board New Horizons (Hinson et al. 2017), which validates the applicability of the temperature template. In the most comprehensive occultation survey made to date, Meza et al. (2019) used the temperature template to trace back Pluto's atmospheric changes between 1988 and 2016, revealing an increase in pressure by a factor of about three during that period.

Pluto occultation July 18, 2012, VLT/NACO H-band

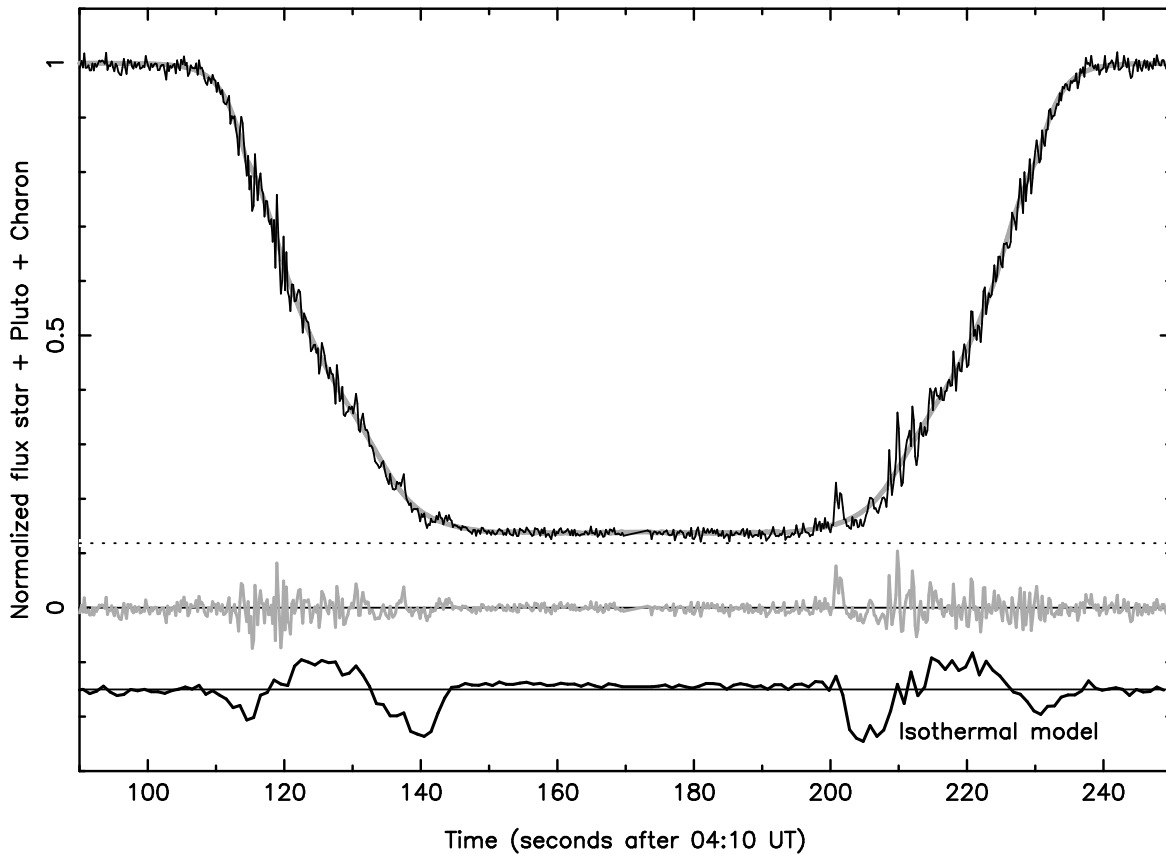


**Fig. 2.** Pluto occultation from Paranal on 2012 July 18, adapted from Dias-Oliveira et al. 2015 (converted to gray-scale). The gray curve is from the template thermal profile. The data plotted spans about 3 minutes (see the UT time plotted along the horizontal axis) and includes flux from Pluto, Charon and the star. From top to bottom, the horizontal lines indicate (i) the measured zero stellar flux (dotted), (ii) the zero flux, together with the residuals (data minus model), (iii) the residuals (shifted by  $-0.15$  for better viewing) obtained by forcing an isothermal mesosphere at  $95.5$  K above the stratopause, near  $1215$  km. The large discrepancy then observed shows that a mesosphere with a mild negative temperature gradient is necessary to explain the data. This result is independent of the particular isothermal mesosphere considered (here at  $95.5$  K), as the same kind of discrepancies appear with isothermal mesospheres at other temperatures.

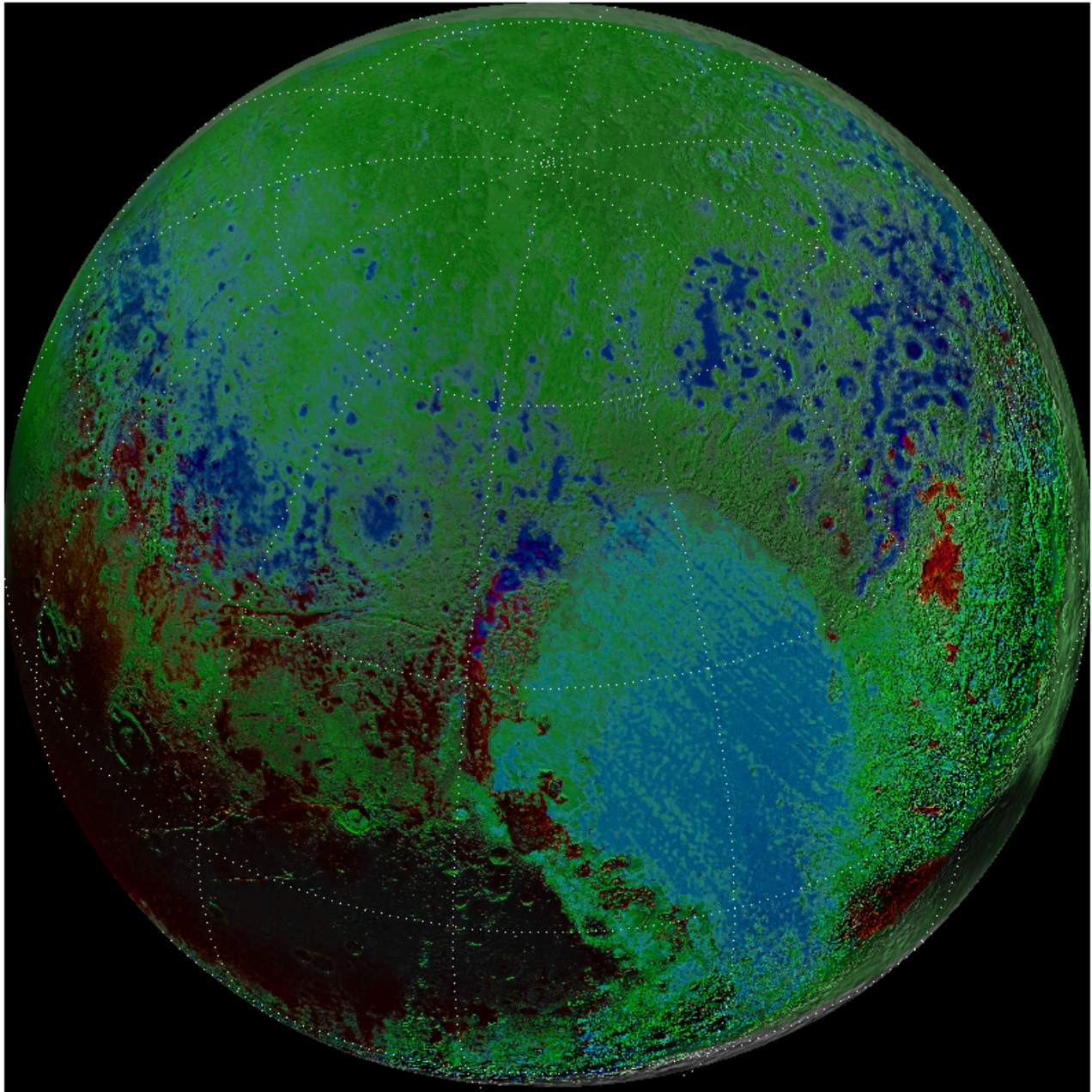
Stellar occultations have proven the most sensitive way of measuring seasonal change in Pluto's atmosphere. This in turn allowed modelers to constrain certain physical parameters that enter into models of seasonal volatile transport (Bertrand & Forget 2016; Johnson et al. 2020; Bertrand et al. 2018; See Section 4.3). These models predict that Pluto's atmosphere is near its maximum pressure, and will start to decline in the upcoming decades. Thus, it is important to continue observing stellar occultations from Earth or Earth orbit to confirm that prediction. Unfortunately, as Pluto moves in front of more depleted stellar fields, such occultations have already become rarer.

340 Ground-based observations confirmed CH<sub>4</sub> as a minor species from IR spectroscopy at high spectral resolution (Young et al. 1997; Lellouch et al. 2009, 2011a, 2015), and CO as a minor species from IR and radio spectroscopy (Young et al. 2001a; Bockelée-Morvan et al. 2001; Lellouch et al. 2010; Greaves et al. 2011; Lellouch et al. 2017), as well as the detection of HCN (Lellouch et al. 2016). Because the total surface pressure was not known pre-encounter, the derived mixing ratio of the minor species was also uncertain. For N<sub>2</sub> pressures of 6.5-24 μbar, the best-fit mixing ratios are 0.06% to 0.53% for CH<sub>4</sub> (with a preferred value of 0.44%), and 0.04% to 0.07% for CO (Lellouch et al. 2011a; 2015). The precision has not yet been good enough to detect changes with time. This may change, with new telescopes or instrumentation, and also now that we can use New Horizons measurements of the temperature structure to improve models of CH<sub>4</sub> line absorption.

## 2.2. New Horizons Observations

350 The New Horizons spacecraft made many observations relevant to volatile transport. Other chapters cover this in detail: geology (White et al.), the geologic evidence for sublimation processes (Moore and Howard), photometric properties and color (Olkin et al.), volatile distributions (Cruikshank et al.), and atmospheric structure (Summers et al.). New Horizons observations revealed latitudinal variation in albedo and composition, and albedo variations larger than any in the solar system apart from Iapetus, as well as dramatic topography, glaciers, and a range of surface ages. The presence of the deep N<sub>2</sub> plains of Sputnik Planitia was completely unexpected, and dominates much of the post-encounter thinking about volatile transport and volatile cycles.

360 New Horizons measurements yielded surface radii and pressures, ending years of ambiguous interpretation of near-surface conditions from ground-based stellar occultations. The mean radius from imaging is 1188.3±1.6 km (Nimmo et al. 2017). The observed topography on Pluto varies about this mean by roughly ±5 km (Schenk et al. 2018). Specifically, the radii probed with precision by the REX radio occultation were 1187.4 ± 3.6 km at ingress and 1192.4 ± 3.6 km at egress (Hinson et al. 2017). The mean pressure at 1189.9 km was 1.15±0.07 Pa (Hinson et al. 2017), and the variation between ingress and egress is as expected given their different altitudes. The pressure of 1.15±0.07 Pa is consistent with N<sub>2</sub>-ice in equilibrium at 36.9±0.1 K (Fray and Schmitt 2008). The CH<sub>4</sub> number density was measured by solar occultation (Young et al. 2018). Models were needed to extrapolate CH<sub>4</sub> number density to the surface from 80 km, the lowest altitude at which CH<sub>4</sub> was last well measured, resulting in a CH<sub>4</sub> surface mixing ratio of 0.28-0.35%.



370 **Fig. 3.** Orthographic views of the encounter hemisphere of Pluto, centered on 160° E, 45° N, with 30° lines of latitude and longitude. Hue and saturation indicate composition, and brightness is set by the basemap (Schenk et al. 2018). The red channel is the H<sub>2</sub>O spectral index of Schmitt et al. (2017) scaled from -0.00 to 0.25. The blue channel is from the N<sub>2</sub> spectral index of Schmitt et al. (2017) scaled from -0.005 to 0.105. The green channel is the average of the 1.7- $\mu$ m CH<sub>4</sub>

spectral index of Schmitt et al. (2017) scaled from -0.05 to 0.41 and the 0.89- $\mu\text{m}$   $\text{CH}_4$  spectral index of Earle et al. (2018b) scaled from -3 to 4.

380 Sputnik Planitia is a feature spanning roughly 1200 km in longitude and 2000 km in latitude, centered at roughly  $15^\circ$  N and  $180^\circ$  E (Fig 3), depressed several km below the surrounding terrain. It covers 5% of Pluto's surface (White et al. 2017) and is likely to be 3-10 km deep (McKinnon et al. 2016; Trowbridge et al. 2016), which makes it the major reservoir of  $\text{N}_2$  on Pluto (Glein & Waite 2018), with a mass equivalent to a global layer  $\sim 60$  to 500 m deep ( $6 \times 10^4$  to  $5 \times 10^5$   $\text{kg m}^{-2}$ ). Both  $\text{N}_2$ -rich and  $\text{CH}_4$ -rich ice phases are present in Sputnik Planitia (Protopapa et al. 2017), with traces of CO (Grundy et al. 2016; Schmitt et al. 2017). Consistent with ground-based spectra, the  $\text{CH}_4$  is seen at only 0.3 to 0.5% in the  $\text{N}_2$ -rich ice, which is much lower than its saturation limit (See Section 3.1). There is a gradient of properties within Sputnik Planitia, with the northwest area having a smaller grain size or path-length, and relatively less  $\text{N}_2$  (Protopapa et al 2017).

390 Outside of Sputnik Planitia, Pluto's surface shows strong latitudinal patterns in albedo (Schenk et al. 2018), color (Olkin et al. 2017; Earle et al. 2018) and composition (Protopapa et al. 2017; Schmitt et al. 2017; Earle et al. 2018; Gabasova et al. 2020). Near the equator, Pluto's surface shows high albedo contrast, with Cthulhu and other dark, reddish areas girdling the equator to roughly  $10^\circ$  N. These dark areas are mostly volatile free, most likely covered by tholins (See Cruikshank chapter), but New Horizons detected  $\text{CH}_4$ -rich ice at some high-altitude ridgetops and northward slopes within these dark areas. At low-to-mid northern latitudes ( $10^\circ$  N to  $35^\circ$  N), LEISA detected abundant  $\text{CH}_4$ -rich ice in the same pixels as  $\text{H}_2\text{O}$  ice. The  $\text{CH}_4$ -rich Bladed Terrain is also at these latitudes. In the mid latitudes ( $35^\circ$  N to  $55^\circ$  N),  $\text{N}_2$ -rich ice is common. In both the mid-latitudes and the Bladed Terrain,  $\text{N}_2$  favors low altitudes (Lewis et al. 2020). In the  $\text{N}_2$ -rich ice, trace amounts of CO are present, and the  $\text{CH}_4$  is diluted at well below its saturation value, typically 0.1% to 0.5% (Protopapa et al. 2017). At high latitudes ( $55^\circ$  N to  $90^\circ$  N), there is increasingly more  $\text{CH}_4$ -rich ice with increasing northern latitude. The presence or amount of  $\text{N}_2$  in the  $\text{CH}_4$ -rich ice is not measurable. The composition of terrains south of the dark equatorial areas is difficult to measure in the New Horizons data.

400 For all volatile ices, inside or outside of Sputnik Planitia, the derived grain sizes for the  $\text{CH}_4$ -rich ice is relatively small, 0.2 to 1 mm, while the derived grain sizes for the  $\text{N}_2$ -rich ice is quite large, 0.1 to 1 m (Protopapa et al. 2017). Ground-based observations also found small  $\text{CH}_4$  grains and large  $\text{N}_2$  grains (Merlin et al 2010; Grundy & Buie 2001; Douté et al. 1999). The large  $\text{N}_2$  grain sizes reported in these works are more usefully thought of as distances between scattering centers than the size of an individual grain (Grundy & Buie 2001).

Ethane could not be detected by LEISA because the spectral resolution is too low to observe its weak signature at 2.405  $\mu\text{m}$ . Although  $\text{CO}_2$  is present on Triton, this non-volatile ice is not detected on Pluto.

### 3. Characteristics of the volatile cycles on Pluto

#### 3.1. Generalities

410 Several bodies in the solar system have atmospheres supported hydrostatically by the vapor pressure of ices on the surface, including Mars, Triton, and Pluto. On Pluto, global hydrostatic equilibrium at a nearly uniform temperature of the N<sub>2</sub>-rich ice is enforced primarily by the high volatility of N<sub>2</sub>. Since the ice temperature drives the vapor pressure that determines the bulk of the atmosphere, Pluto's diurnal, seasonal, and longer-term volatile cycles are sensitive to the geographically changing insolation.

##### 3.1.1 Pure ices and ice mixtures

420 The equilibrium vapor pressure of the ice phase of a pure species is determined uniquely by its temperature according to the Clausius-Clapeyron equation. This pressure is often useful in scenarios that depart from equilibrium as well, such as the situation on Pluto of subliming or condensing ice, as long as the temperature is stable. At the low temperatures of Triton and Pluto, the volatile species are N<sub>2</sub>, CO, and CH<sub>4</sub>, in descending order of volatility (Fig. 4). The contrast between the volatile pressures of these three ices becomes more extreme with decreasing temperature. At 40 K, The N<sub>2</sub> equilibrium pressure is 6.55 Pa and the CO and CH<sub>4</sub> pressures are smaller by factors of 0.16 and 1.2 x 10<sup>-4</sup>, respectively (using the compilation of Fray & Schmitt, 2009). At 36.9 K, in equilibrium with the 1.15 Pa from the New Horizons radio occultation, the CO and CH<sub>4</sub> pressures are smaller than that of N<sub>2</sub> by factors of 0.12 and 6.0 x 10<sup>-5</sup>, respectively.

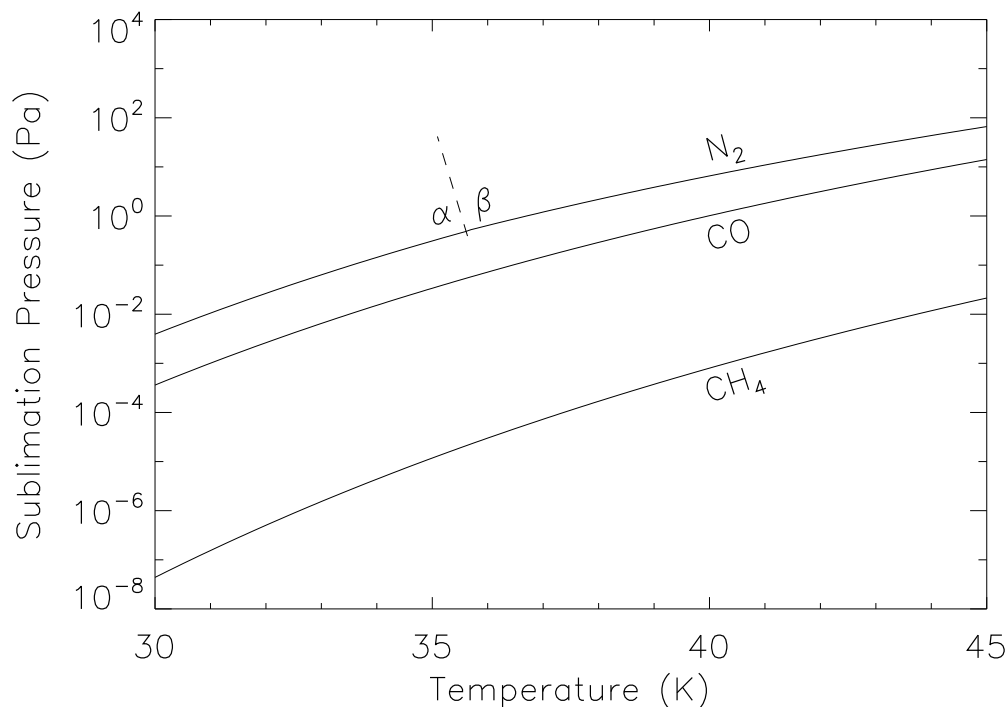


**Fig 4.** Equilibrium vapor pressure vs. ice temperature over pure ices, from Fray & Schmitt (2009).

These vapor pressures are extremely sensitive functions of temperature. For example, at 37 K, an increase of only 0.16 K (0.4%) increases the N<sub>2</sub> pressures by 10%. This is because of the large latent heat of sublimation,  $L$ , which in this temperature range is  $\sim 2.5 \times 10^5 \text{ J kg}^{-1}$ ,  $2.8 \times 10^5 \text{ J kg}^{-1}$ , and  $6.1 \times 10^5 \text{ J kg}^{-1}$  for N<sub>2</sub>, CO, and CH<sub>4</sub> respectively. The equilibrium pressure increases with temperature according to the Clausius-Clapeyron equation:  $dp_{eq}/dT_{eq} = (p_{eq}/T_{eq})(L/RT_{eq})$ , where  $R$  is the specific gas constant. For N<sub>2</sub>, the unitless ratio  $L/RT_{eq}$  is much larger than one, and ranges from 31 to 18 for  $T_{eq}$  between 30 and 45 K; for CO and CH<sub>4</sub>, the ratios are similarly large (32 to 21 for CO, and 39 to 26 for CH<sub>4</sub>).

Hydrostatically supported atmospheres demonstrate the different behavior of immiscible volatile ices (such as H<sub>2</sub>O and CO<sub>2</sub> on Mars) and miscible ones (such as N<sub>2</sub> and CH<sub>4</sub> on Pluto or Triton). When ice includes immiscible species, the total vapor pressure is the sum of the vapor pressures of the pure constituents. This is because their self-attraction at the molecular level is stronger than their mutual attraction. They therefore do not mix at the molecular level and so the species do not mutually perturb each other's energy levels. Their spectral lines thus remain unshifted. Their vapor pressure depends on a single thermodynamic variable, temperature, and it does not depend on the relative proportions of the species present.

Miscible species (e.g., N<sub>2</sub> and CH<sub>4</sub>), for which their mutual attraction at the molecular level is greater than their self-attraction, exhibit the opposite, and a more complicated, behavior. In the solid phase, these species are found to be mixed at the molecular level, forming a solid solution (Prokhvatilov & Yantsevich 1983; Trafton 2015)). This results in the perturbation of each other's molecular energy levels, with spectral lines of the participating species being shifted relative to the spectra of the pure solid species. In general, the total pressure will not be the sum of the partial pressures of the pure species, but will depend on the composition of the system through the equation of state. The thermodynamic state of the system determines the phases and the total vapor pressure, and in thermodynamic equilibrium, the state depends on the equilibrium phase diagram for the solid solution. In general, an equation of state (EOS) will be needed to calculate the equilibrium pressure and phase compositions. With three volatiles, a ternary phase diagram is needed to describe the phases of Pluto's solid solution (Tan & Kargel 2018). However, isobaric calculations of the ternary N<sub>2</sub>/CO/CH<sub>4</sub> diagram in Table 2 of Tan & Kargel 2018 show that the equilibrium composition of CO is insensitive to temperature changes. Moreover, CO and N<sub>2</sub> are similar in properties (e.g. molecular weight and sublimation pressure) and the phase behavior of their ices. This is the rationale for neglecting CO in Pluto's phase equilibrium and adopting the N<sub>2</sub>-CH<sub>4</sub> binary phase diagram for EOS calculations (Trafton, Tan, & Stansberry 2019).

The binary phase diagram (Prokhvatilov & Yantsevich 1983, also see Chapter by Cruikshank et al.) shows that the solubility of the solid solution (CH<sub>4</sub> in N<sub>2</sub>-rich ice, or N<sub>2</sub> in CH<sub>4</sub>-rich ice) is only a few percent at Pluto's low ice temperatures. If the solution were saturated, in equilibrium two separate solid phases would form: a N<sub>2</sub>-rich phase and a CH<sub>4</sub>-rich phase, each at the saturation concentration. No pure ice of either species would exist in thermodynamic equilibrium. The partial pressures at fixed temperature in equilibrium do not depend on the relative proportions of these phases, which is determined by the overall composition of the system. In this saturated case there are 2 species (N<sub>2</sub> and CH<sub>4</sub>) and 3 phases (N<sub>2</sub>-rich ice saturated with CH<sub>4</sub>, CH<sub>4</sub>-rich ice saturated with N<sub>2</sub>, and vapor), and Gibb's phase rule says

there should be only one degree of thermodynamic freedom. Temperature thus suffices to determine the equilibrium state of the system including the vapor pressure.

As described by Trafton (2015, his Section 5.2), in thermodynamic equilibrium, the 3-phase saturated solution might be expected to have some similarities to an immiscible solution, namely the dependence on a single thermodynamic variable. But, the component partial pressures fall short of those for the pure components as calculated by Tan and Kargel (2018, as tabulated in Young et al. 2019): in the saturated 3-phase system at 35.6 to 40.0 K, the ratio of an ice's partial pressure to its pure vapor pressure is 98% to 95% for N<sub>2</sub> and 74% to 79% for CH<sub>4</sub>. If the solid solution were unsaturated in thermodynamic equilibrium, then only a single solid phase would be present—a “homogeneous” phase that is either N<sub>2</sub>-rich or CH<sub>4</sub>-rich, analogous to the homogeneous gas phase. In this case (2 species, 2 phases), Gibb's phase rule says there should be two degrees of thermodynamic freedom, and the vapor pressure would depend on two thermodynamic variables; e.g., temperature and ice mole fraction,  $x_{\text{CH}_4}$  in N<sub>2</sub>-rich ice or  $x_{\text{N}_2}$  in CH<sub>4</sub>-rich ice.

A common approximation in lieu of the Equation of State (EOS) has been to use Raoult's law (Owen et al. 1993; Trafton et al. 1990; Forget et al. 2017; Bertrand et al. 2019), which states that the partial pressure of the dominant component of a solution is the vapor pressure of the pure component times its mole fraction in the solution. While Raoult's law also applies to solid solutions, it does not strictly apply to the minor component of the solution, especially when the phase changes with concentration, as for Pluto's volatiles. For minor components of a solution, Henry's law is more appropriate, which does not reference the pure species vapor pressure. Take, for example, N<sub>2</sub>-rich ice at 38 K with CH<sub>4</sub> undersaturated at  $x_{\text{CH}_4}=0.3\%$  (e.g., at the sublimation point, or at V-VS<sub>1</sub> boundary in the terminology of Tan & Kargel 2018), for which the application of Raoult's law as an approximation would predict a partial pressure of 0.5 μPa, while the EOS of Tan & Kargel (2018) predicts a partial pressure of 13 μPa. At the CH<sub>4</sub> saturation value of  $x_{\text{CH}_4}=3.9\%$ , the partial pressure via Raoult's law would be 6.6 μPa, vs. 130 μPa for the EOS. Similarly, for CH<sub>4</sub>-rich ice at 38 K with N<sub>2</sub> undersaturated (similarly, at the sublimation point, or at V-VS<sub>2</sub> boundary in the terminology of Tan & Kargel 2018), a partial pressure for N<sub>2</sub> of 0.045 Pa would be reached at  $x_{\text{N}_2} \approx 2.5\%$  applying Raoult's law but only  $x_{\text{N}_2} \approx 0.08\%$  using the EOS. However, as shown in Section 3.4.1, the historical misapplication of Raoult's law to approximate the vapor pressure of the minor component of the solution has little practical impact on calculations of mass fluxes.

### 3.1.2 Insolation at various timescales

The intensity and distribution of the incident solar flux depends on the instantaneous heliocentric distance and subsolar latitude (Levine et al. 1977). Since these parameters are well known, insolation on Pluto can be easily calculated before making any assumptions about thermal properties, surface composition and reflectivity, etc., thus making incident insolation one of the basic inputs for the various models described below. At the time of the New Horizons encounter, Pluto was at 32.9 AU from the sun, for a normal incident solar flux of 1263 mW m<sup>-2</sup>. Pluto was experiencing northern spring (Fig 5D), with its subsolar latitude at 52° N. During this time all latitudes South of 38° S were in constant winter shadow, while all areas north of 38° N received constant sunlight, with the maximum diurnal average insolation (995 mW m<sup>-2</sup>) occurring at the North Pole (Fig 6, top left and top right).

510 Pluto obliquity is currently  $119.51^\circ$  and the solar longitude at perihelion is  $\sim 3.8^\circ$ , which means that equinoxes occur near perihelion and aphelion (Fig 5D). Therefore, both hemispheres receive a similar distribution of insolation over Pluto's year (Earle et al., 2017; Fig 6, middle left and middle right). Each pole receives the same maximum insolation, and comparable latitudes spend the same amount of time in continuous darkness. Because Pluto has a high orbital eccentricity (approximately 0.25), its heliocentric distance varies from 29.6 to 49.9 AU, which leads to the normal incident solar flux varying by a factor of  $\sim 3$  over the course of its orbit (see review by Spencer et al., 1997).

When averaged over a full orbit, insolation is symmetric across the equator (Nadeau and McGehee, 2017; Hamilton et al. 2016; Fig 6, lower left and lower right). Due to Pluto's high obliquity, the average insolation over one Pluto year in its current orbit is highest at the poles and lowest at  $25^\circ$  N and  $25^\circ$  S.

520 Also shown (Fig 6) are the climate zones on Pluto as defined by Binzel et al. (2017). In Pluto's current orbit, the subsolar latitude reaches  $\pm 61^\circ$  at the solstices. Between these extremes are the *tropics*, where the sun is overhead at some time in the year, equivalent to Earth's tropics of Cancer and Capricorn. The complement, poleward of  $\pm 61^\circ$ , is termed the *polar climate zone*. Latitudes poleward of  $\pm 29^\circ$  experience days where the Sun never sets in the summer or never rises in the winter, otherwise known as the *arctic* (and the complement, between  $\pm 29^\circ$ , is termed *diurnal climate zone*). Unlike on Earth, the tropics and arctic latitudes overlap, for a *tropical arctic* climate zone. The climate zones appear associated with the gross geology of Pluto (Fig 7). In particular, the diurnal zone is a zone where albedo feedback is most favored, leading to strong albedo contrasts (Earle et al. 2018a).

530 The obliquity, solar longitude of perihelion, and eccentricity vary over timescales of several Myr (Eq 1a-f). This is known as a Milankovitch mechanism, which also occurs on other planetary bodies such as the Earth, Mars, and Titan. Recent years have emphasized the importance of these cycles, but have also introduced some elements of confusion. We present here the equations controlling the insolation at Pluto, using the equations Dobrovolskis et al. (1997). Earle (2018) showed that estimates of the important dynamical parameters (the principle moments of inertia, the semi-major axis of the Pluto-Charon system, and the radii and masses of Pluto and Charon), have changed by less than 6% since the work of Dobrovolskis et al. (1997). Until such time as the numerical integrations are repeated, we also use the numerical results from Dobrovolskis et al. (1997). We define an intermediate angle ( $\psi$ ), which varies with a period of  $360^\circ/(91^\circ \text{ Myr}^{-1}) = 3.96 \text{ Myr}$ ; and a phase angle ( $\phi$ ), defined as the angle, projected onto Pluto's orbital plane, between the ascending node on the invariable plane and Pluto's spin vector, which varies with a period of  $360^\circ/(130.2^\circ \text{ Myr}^{-1}) = 2.76 \text{ Myr}$ . From these we can calculate the eccentricity ( $e$ ), obliquity ( $\theta$ ), and the solar longitude of perihelion ( $L_{s,peri}$ , related to the parameters in Dobrovolskis et al. 1997 via  $L_{s,peri} = -\chi$ , where  $\chi$  is the angle, measured in Pluto's orbital plane, from Pluto's longitude of perihelion to its vernal equinox). The sub-solar latitude ( $\delta_s$ ) varies over Pluto's orbit depending on the true anomaly ( $\nu$ ). These can be expressed as a function of time ( $t$ ) in millions of years A.D (i.e., so flyby on July 14, 2015 was at  $t = 0.0020155$ ):

(Eq. 1a) 
$$\psi = 72.8^\circ + 91.0^\circ t$$

(Eq. 1b) 
$$\phi = 19.5^\circ + 130.2^\circ t$$

(Eq. 1c) 
$$e = 0.244^\circ + 0.022^\circ \cos \psi + 0.005^\circ \cos 3\psi$$

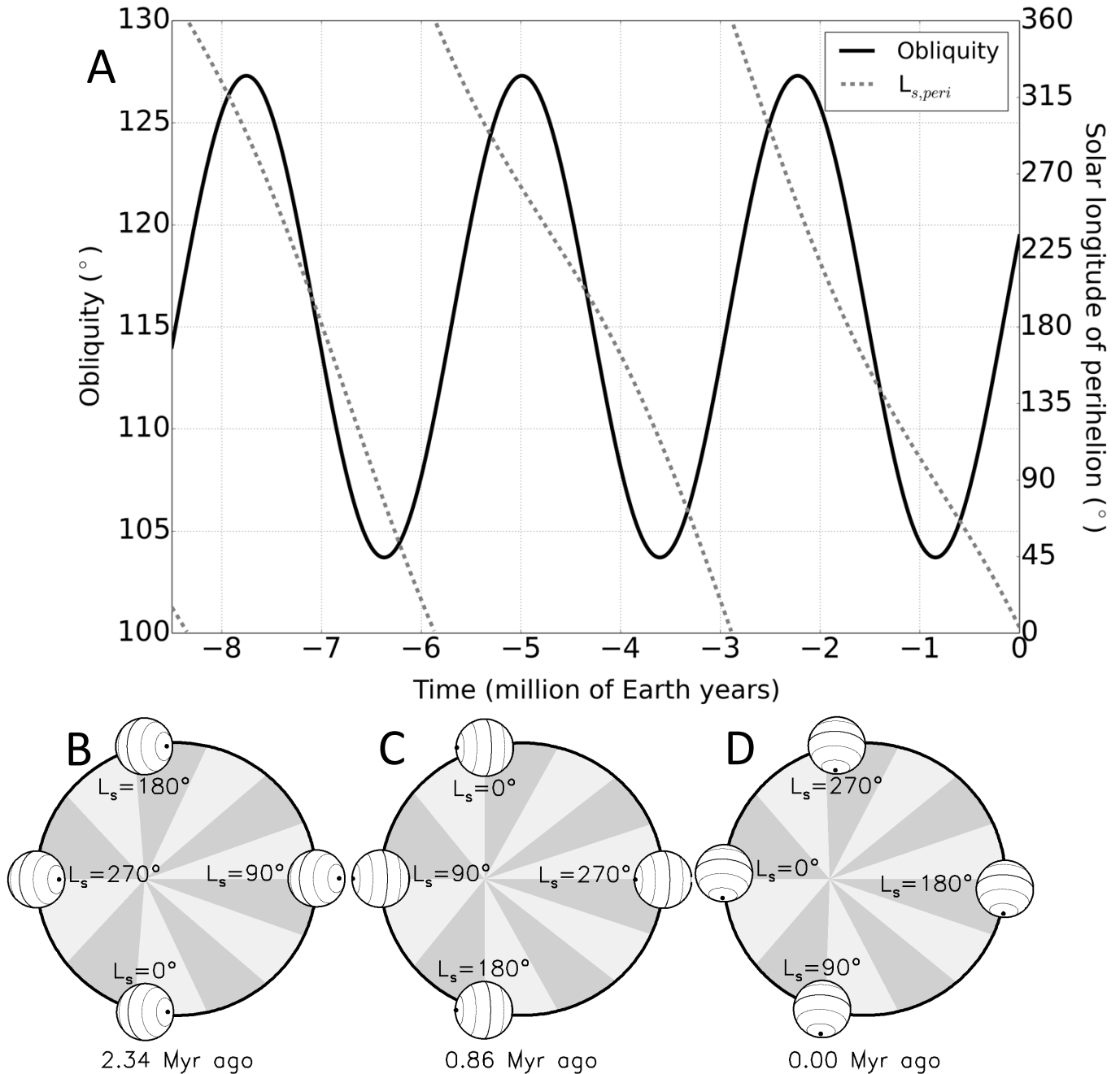
(Eq. 1d) 
$$\theta = 115.5^\circ + 11.8^\circ \sin \phi$$

(Eq. 1e) 
$$L_{s,peri} = -\phi + 24.0^\circ \sin \psi$$

(Eq. 1f) 
$$\sin \delta_S = \sin \theta \sin(\nu + L_{s,peri})$$

550 Pluto's obliquity varies by about  $23^\circ$  between  $104^\circ$  and  $127^\circ$  over a period of 2.8 Myr (Fig 5A), thus affecting the latitudes of the climate zones and the annually averaged insolation. Over 2.8-Myr timescales, the latitude of minimum insolation moves from  $\pm 30^\circ$  to the equator, and the difference between average insolation at the equator vs. the poles becomes more or less dramatic. The eccentricity oscillates between 0.222 and 0.266 with a 3.95 Myr period.

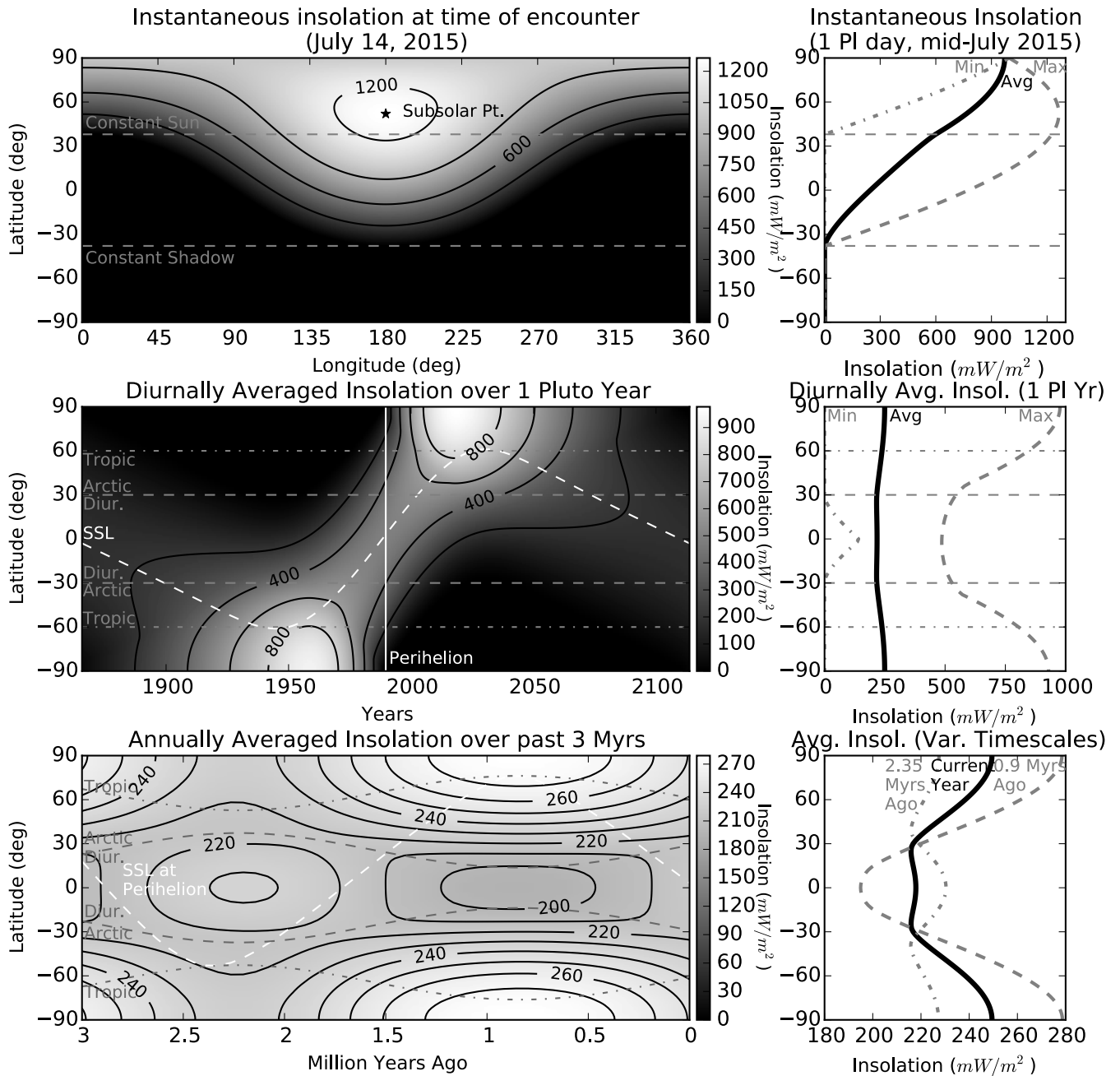
560 The longitude of the ascending node ( $\Omega$ ) regresses over  $360^\circ$  with a period of 3.7 Myr, given by  $\Omega = 111.428^\circ - 97.209^\circ t - 1.5^\circ \sin \psi$ , while the argument of perihelion ( $\omega_p$ ) librates with a period of 3.96 Myr. The longitude of perihelion, being the sum of  $\Omega$  and  $\omega_p$ , also regresses with a period of 3.7 Myr. However, these angles are of minor importance for the insolation at Pluto. Numerical integration shows Pluto's spin pole advancing with a precession period near 11.5 Myr (Dobrovolskis et al. 1997). This combines with the change in the longitude of the ascending node to result in a period for  $\phi$  of 2.76 Myr, which modifies the solar longitude of perihelion ( $L_{s,peri}$ ; Fig 5A). In Pluto's current orbit, the northern spring equinox was nearly coincident with perihelion ( $L_{s,peri} \approx 0^\circ$ ; Fig 5D). When a solstice is at perihelion ( $L_{s,peri} = 90^\circ$  for northern summer solstice at perihelion, Fig 5C, or  $L_{s,peri} = 270^\circ$  for southern, Fig 5B), one hemisphere experiences a short, intense summer and long winter, while the other hemisphere experiences a short winter and long, less intense summer. (Fig 8; also see Bertrand et al. 2019; their Fig 5). Because of the prominence of the  $N_2$  deposits in Sputnik Planitia near  $15^\circ$  N, the solar forcing of the  $N_2$ -rich ices is most extreme when northern solstice is at perihelion (Fig 8, upper) and nearly uniform when northern solstice is at aphelion (Fig 8, lower). Perihelion northern summer solstice ( $L_{s,peri} = \sim 90^\circ$ ) happens at times of high obliquity, and perihelion southern summer solstice ( $L_{s,peri} = \sim 270^\circ$ ) happens at times of low obliquity, with some small variation due to the  $24.0^\circ$  libration of  $\omega_p$  (Fig. 5).



570 **Fig. 5.** A: The astronomical cycles of Pluto during the past 8.5 Earth million years ( $\sim 3$  obliquity cycles). The solid curve indicates obliquity (left axis), and the dashed curve indicates the longitude of perihelion ( $L_{s,peri}$ , right axis). Over 2.8 Myr, Pluto's obliquity ranges between a high value (that is, closer to  $90^{\circ}$ ) of  $104^{\circ}$ , most recently occurring 0.9 Myrs ago, and a low value (that is, closer to  $180^{\circ}$ ) of  $127^{\circ}$ , occurring 2.35 Myrs ago.  $L_{s,peri}$  cycles over  $360^{\circ}$  over  $\sim 2.8$  Myr as well. The slight curvature of  $L_{s,peri}$  is due to  $24^{\circ}$  of modulation by the 3.96 Myr libration of the argument of perihelion. B-D. Pluto's orbit and polar orientation as seen from above the plane of the orbit. The thick ellipse represents Pluto's orbit. Pluto orbits counter-clockwise. The gray wedges show 12 equally spaced divisions in time (roughly 20.7 yr per division). Pluto's obliquity

580

is greater than  $90^\circ$ , so the southern pole is indicated, as well as latitudes  $-60^\circ$ ,  $-30^\circ$ , the equator (bolder), and  $30^\circ$ . Pluto's location is indicated for four solar longitudes ( $L_S$ ):  $L_S = 0^\circ$  (Northern spring),  $L_S = 90^\circ$  (Northern summer),  $L_S = 180^\circ$  (Northern fall), and  $L_S = 270^\circ$  (Northern winter). B: 2.34 Myr ago, Pluto experienced southern summer at perihelion. C: 0.86 Myr ago, Pluto experienced northern summer at perihelion. D: In its current orbit, Pluto experiences northern spring equinox near perihelion.



590 **Fig. 6.** Incident solar flux (insolation) on Pluto at various timescales. Solid curves are contours, labeled in  $\text{mW m}^{-2}$ . (Top left) Insolation over one Pluto rotation at the time of New Horizons flyby, with longitudes relative to midnight. The star indicates the subsolar point at a relative longitude of  $180^\circ$  (e.g., noon) and a subsolar latitude of  $52^\circ \text{ N}$ . The thin dashed lines indicate the latitudes of constant sunlight (northward of  $38^\circ \text{ N}$ ) or constant shadow (southward of  $38^\circ \text{ S}$ ) at flyby. (Top Right) The thick gray dashed curve shows the maximum instantaneous insolation during a Pluto day, and the thick gray dash-dot curve shows the minimum. The thick black solid curve shows the diurnal average. The thin dashed lines indicate the latitudes of constant sunlight and constant shadow, as in the top left plot. (Middle left) Diurnally averaged insolation over the current Pluto year, as a function of Earth year AD. The white dashed curve indicates the subsolar latitude (SSL). The thin gray dot-dashed lines indicate the tropics at  $\pm 61^\circ$ , between which the sun is overhead at some time in Pluto's year. The thin gray dashed lines indicate the arctic/diurnal division at  $\pm 29^\circ$ , between which sun rises and sets every day of Pluto's year. Latitudes north of  $29^\circ \text{ N}$  or south of  $29^\circ \text{ S}$  experience arctic night sometime during Pluto's year. The thin solid vertical line marks the time of perihelion. At perihelion, Pluto's subsolar latitude was close to  $0^\circ$ . (Middle right) The thick gray dashed curve shows the maximum diurnally averaged insolation during a Pluto year, and the thick gray dash-dot curve shows the minimum. The thick black solid curve shows the annual average. The thin gray dot-dashed lines indicate the tropics, and the thin gray dashed lines indicate the arctic/diurnal division, as in the middle left plot. (Lower left) Annually averaged insolation as a function of time before the present. The white dashed curve indicates the subsolar latitude (SSL) at perihelion. The thin gray dot-dashed curves indicate the latitudes of the tropics, and the thin gray dashed curves indicate the latitudes of the arctic/diurnal division. The latitudes of the tropics and the arctic/diurnal division both vary over Milankovitch cycles. (Lower right) The thick gray dashed curve shows the average insolation from 0.9 million years ago to the present day, and the dash-dotted curve shows the average insolation from 2.35 million years ago to the present day. The thick black solid curve shows the annual average for the current Pluto year, identical to the thick black solid curve in the middle right.

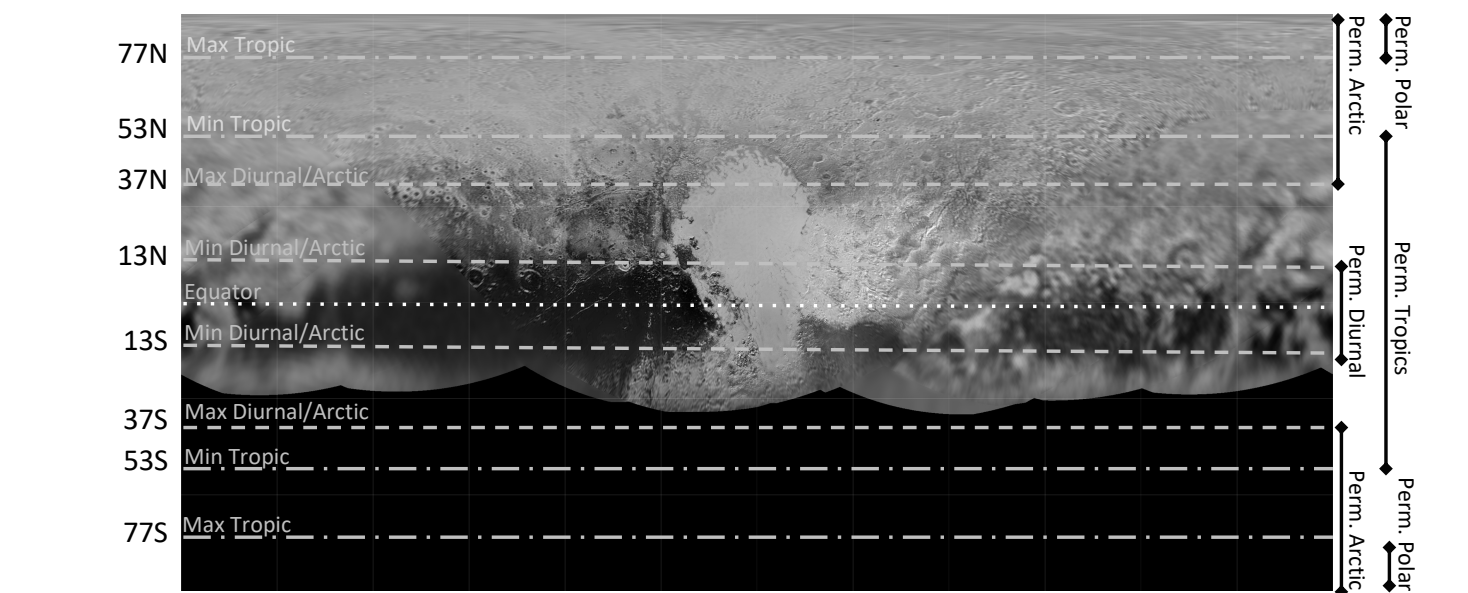


**Fig. 7.** Climate zones on Pluto and their geographic expression. Over the last Milankovitch cycle, the division between the arctic and diurnal climate zones (dashed lines) oscillates between  $\pm 13^\circ$

620 and  $\pm 37^\circ$ , and the division between the tropic and polar climate zones (dash-dot lines) oscillates between  $\pm 53^\circ$  and  $\pm 77^\circ$ . The area between  $\pm 13^\circ$  is a permanent diurnal zone, which experiences sunrise and sunset every Pluto day. The area between  $\pm 53^\circ$  is the zone of permanent tropics, where the Sun always reaches the zenith at least once per orbit. Poleward of  $\pm 37^\circ$  is the permanent arctic zone, which always experiences arctic seasons, up to century-long summers and winters during each orbit. Poleward of  $\pm 77^\circ$  is the permanent polar zone, where the Sun never reaches zenith over any orbital period. Adapted from Binzel et al. (2017; see larger figure in the Chapter by Moore & Howard).

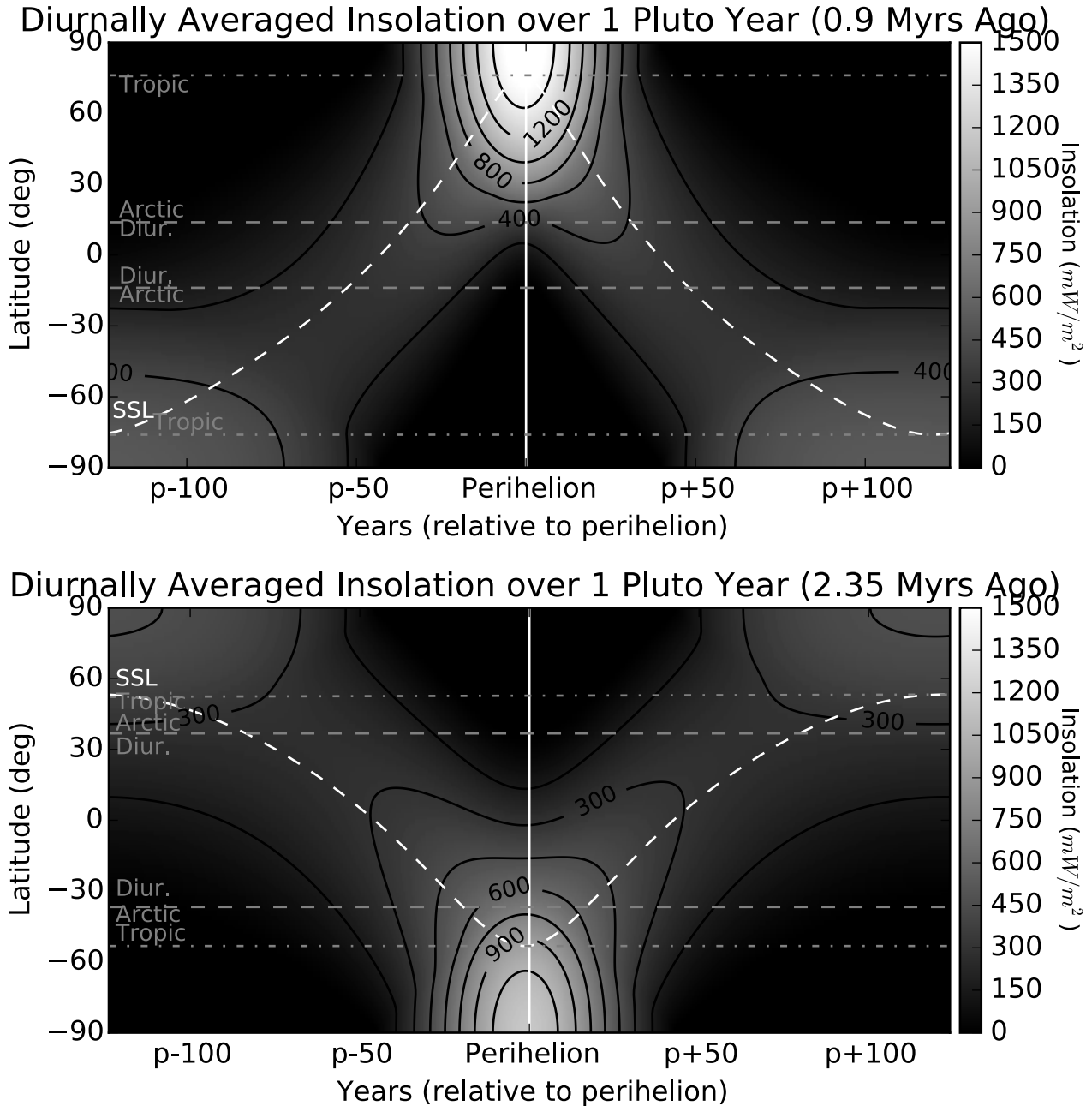


**Fig. 8.** Diurnally averaged insolation over one Pluto year for two different epochs, as a function of Earth years since perihelion. Curves and lines are as in Fig 6, middle left. Top: Northern

630 summer solstice at perihelion ( $L_{s,peri} = 90^\circ$ ) at a time of high obliquity. Bottom: Southern summer  
 solstice at perihelion ( $L_{s,peri} = 270^\circ$ ) at a time of low obliquity. The white dashed curve indicates  
 the subsolar latitude (SSL). The thin gray dot-dashed lines indicate the tropics, between which  
 the sun is overhead at some time in Pluto's year. The thin gray dashed lines indicate the  
 arctic/diurnal division, between which sun rises and sets every day of Pluto's year. The thin solid  
 vertical line marks the time of perihelion.

### 3.1.3 Thermal inertia

Surface temperatures depend on more than just the average insolation. The substrate is able to store the  
 heat accumulated during the day or summer and release it during night or winter, an ability quantified by  
 640 its thermal inertia. Thermal inertia dampens and retards the response of the surface temperature to  
 insolation, and raises the mean temperatures (Spencer 1989). The effects are very different on diurnal and  
 seasonal timescales. Using the definition of Spencer (1989), the sub-surface thermal wave has a  
 characteristic skin depth  $Z = \Gamma/(\rho c \sqrt{\omega})$ , where  $\Gamma$  is the thermal inertia,  $\rho$  is density,  $c$  is the specific heat,  
 and  $\omega$  is frequency ( $2\pi/\text{period}$ ). The importance of the thermal inertia is parameterized by  $\Theta =$   
 $\Gamma\sqrt{\omega}/(\varepsilon\sigma T_{SS}^3)$ , where  $\varepsilon$  is emissivity,  $\sigma$  is the Stephan-Boltzmann constant, and  $T_{SS}$  is the temperature in  
 instantaneous equilibrium with the normal insolation (Spencer 1989). For small values of  $\Theta$  ( $\Theta \ll 1$ ), the  
 temperature responds quickly to changes in insolation, and little heat is conducted into or out of the  
 subsurface. For large values of  $\Theta$  ( $\Theta \gg 4$ ), subsurface conduction is comparable to the peak-to-peak  
 variation in the solar heating, and the amplitude of the temperature variation is small. While  $\Gamma$ ,  $\rho$ , and  $c$   
 650 are properties of the material (including porosity),  $Z$  and  $\Theta$  additionally depend on the forcing timescale.

From the change in observed thermal emission as Pluto rotates, Lellouch et al. (2011, 2016) reported  
 low diurnal thermal inertia of  $\Gamma = 16\text{-}26 \text{ J s}^{-1/2} \text{ m}^{-2} \text{ K}^{-1}$  (tiu) for the  $\text{CH}_4$ -rich and non-volatile terrain types.  
 The thermal inertia for the  $\text{N}_2$ -rich terrain types could not be measured from this data, since the  
 temperature of the  $\text{N}_2$ -rich terrain are nearly isothermal over a Pluto day, regardless of the thermal inertia  
 (e.g., Young 2012). The thermal inertia derived for the  $\text{CH}_4$ -rich and non-volatile terrains was much  
 smaller than the thermal inertia for solid ices near 40 K (Spencer & Moore 1992), whether  $\text{H}_2\text{O}$  (2200  
 tiu),  $\text{N}_2$  (530 tiu), or  $\text{CH}_4$  (630 tiu). The diurnal skin depths are  $\sim 1$  cm (for a near-surface thermal inertial  
 of 20 tiu), and so the reported thermal inertia relates to the thermophysical properties of the top-most  
 layers. The small thermal inertia implies a substrate with high porosity at the top-most layers of Pluto's  
 660 surface (Carson et al. 2005). The seasonal thermal wave penetrates deeper into the substrate, below this  
 high-porosity crust. Several models predict much larger thermal inertias at the depths probed by the  
 seasonal wave. For example, Bertrand and Forget 2016 favor 800 tiu, for which the seasonal skin depth is  
 40 m.

For the diurnal thermal wave near perihelion, the thermal parameter  $\Theta$  is about 4.5-6 for the  $\text{CH}_4$ -rich  
 and non-volatile terrain types (Lellouch et al. 2016). Surprisingly, for seasonal thermal wave, the thermal  
 parameter is likely to be similar. Pluto's year is  $1.4 \times 10^4$  times longer than its day, so  $\sqrt{\omega}$  is 118 times  
 smaller, which should decrease  $\Theta$ . Countering this is the fact that the thermal inertia is larger at the depths  
 probed by the seasonal wave than at the depths probed by the diurnal wave, and that the relevant

670 temperature is not the subsolar temperature,  $T_{SS}$  (as in Spencer 1989), but rather the colder global  $N_2$  temperature (as in Young 2012). Near the times of maximum insolation, the thermal conduction is comparable to the energy lost by thermal emission for thermal parameters greater than about unity. When there is no insolation (e.g., during polar winter), the heat stored in the substrate can have a significant effect.

### 3.1.4 Atmospheric effects on surface energy balance

680 Pluto's atmosphere is so transparent and rarefied that any atmospheric processes (clouds, hazes, convection, radiative transfer within the atmosphere) have no significant impact on the radiative thermal and conductive balance at the surface (Stansberry et al. 1994; Forget et al. 2017). Thermal conduction to the surface given a near-surface gradient of  $\sim 5 \text{ K km}^{-1}$  (Hinson et al. 2017) is only  $\sim 0.02 \text{ mW m}^{-2}$ , and the heat transfer through turbulent diffusion is only a few  $\text{mW m}^{-2}$  (Stansberry et al. 1992), so the ambient atmospheric temperature hardly affects the local surface temperature. In addition, most of Pluto's thermal emission is longward of  $52 \mu\text{m}$ , which is not absorbed by the atmosphere. Nevertheless, the atmosphere affects the surface energy balance through changes to the albedo (as newly deposited ice is likely to be bright), or to the thermal inertia (as the sublimation and condensation can affect porosity). Most significantly, the atmosphere affects surface temperatures through latent heat of sublimation, particularly of  $N_2$ -rich ice, and is the medium for  $N_2$  moving from sublimating spots to condensing locations (see Chapter by Forget).

## 3.2 $N_2$ cycle

690 It is useful to begin with the simple picture of Pluto's  $N_2$  atmosphere in global balance with its surface  $N_2$  ice (e.g., Spencer et al. 1997). For a high-enough surface pressure, the pressure at a near-surface reference altitude will be nearly the same everywhere, and the surface pressures and temperatures of the  $N_2$  ice will be close to vapor-pressure equilibrium. For a surface without topography, the  $N_2$  ice temperatures will be close to isothermal across the surface, at a value that is determined by the radiative balance between the absorbed insolation and thermal radiation from all of the  $N_2$  ice. Sublimation occurs from areas of high insolation, with condensation onto areas of low insolation, and the sublimation winds transport mass and latent heat of sublimation from areas of net sublimation to areas of net condensation. Because  $N_2$  is so much more volatile than  $CO$  or  $CH_4$ , the small amount of  $CH_4$  or  $CO$  diluted in the  $N_2$ -rich ice does not change this basic picture.

Putting these considerations into equation form, the local energy balance can be written (Eq. 2):

$$(Eq. 2) \quad c_s \frac{dT}{dt} = \mu(1 - A) \frac{S_{1AU}}{\Delta^2} - \varepsilon\sigma T^4 - k \frac{dT}{dz} - L\dot{m}$$

700 where  $c_s$  is the surface heat capacity (in  $\text{J m}^{-2} \text{K}^{-1}$ ; see Forget et al. 2017; Hansen & Paige 1996),  $t$  is time,  $\mu$  is the cosine of the incidence angle,  $A$  is the bolometric Bond albedo,  $S_{1AU}$  is the solar constant (that is, the normal solar flux at 1 AU,  $1361 \text{ W m}^{-2}$ ),  $\Delta$  is the heliocentric distance in AU,  $\varepsilon$  is the emissivity,  $\sigma$  is the Stefan-Boltzmann constant,  $k$  is the conductivity,  $z$  is the substrate depth (0 at the surface, negative below),  $L$  is the latent heat of sublimation, and  $\dot{m}$  is the net is the net sublimation rate of  $N_2$  ice ( $\text{kg m}^{-2} \text{s}^{-1}$ )

1). Locally, the mass fluxes for N<sub>2</sub> are energy limited, and the left-hand side is small compared with the other terms, so that  $L\dot{m}$  balances insolation, thermal emission, and conduction to the subsurface. Globally, what goes up mainly comes down; on seasonal timescales, and sometimes on diurnal timescales, the global average of  $L\dot{m}$  can be neglected (e.g., Young 2012).

710 Consider an ideal Pluto. If Pluto's atmosphere were always dense enough to ensure efficient global transport of N<sub>2</sub>, if the surface were entirely covered by N<sub>2</sub>, if the thermal inertia were negligible, if the global average of  $L\dot{m}$  can be neglected, and if there were no topography, then the global average of Eq. 2 would simplify to:  $\varepsilon\sigma T_{eq}^4 \approx \bar{\mu}(1 - A)S_{1AU}/\Delta^2$ , where  $\bar{\mu} = 1/4$  for spatially uniform ice. To first order, the N<sub>2</sub> frost temperature depends on  $(1 - A)/\varepsilon$ . However, the real Pluto deviates from this ideal because the atmosphere may or may not occasionally be non-global, Pluto's surface is heterogeneous, thermal inertia is likely to be significant on diurnal and seasonal timescales, and New Horizons detected significant topography on Pluto (e.g., Trafton 1990, 2015; Trafton et al. 1998; 2015; Grundy & Buie 2002; Hansen and Paige 1996; Stern et al. 2015). We deal with each of these items in turn.

### 3.2.1 Departure from global equilibrium (or "Will Pluto's atmosphere collapse?")

720 For the New Horizons flyby conditions (subsolar latitude = 51.6°,  $p = 1.15$  Pa,  $T_{eq} = 36.9$  K), Pluto's N<sub>2</sub> ice temperatures should be nearly isothermal across the globe, and the N<sub>2</sub> ice should be nearly in equilibrium with the atmosphere, despite local sublimation or condensation and the variation of insolation with time. Near-equilibrium is a consequence of the high volatility and latent heat of sublimation of N<sub>2</sub> at Pluto's temperatures, as can be demonstrated several ways. First, the number of molecules leaving the N<sub>2</sub>-rich ice nearly equals the number of molecules impinging on and sticking to it. That is, the net sublimation or condensation rate is much smaller than the one-way upward or downward flux. Roughly estimating the mass flux by  $L\dot{m} \approx \varepsilon\sigma T^4$  gives  $\dot{m} \approx 4.2 \times 10^{-7}$  kg m<sup>-2</sup> s<sup>-1</sup>. By kinetic theory (the Knudsen-Langmuir equation), and assuming unit sticking coefficient, the one-way upward mass flux is  $\dot{m}_{up} = p_{eq}/\sqrt{2\pi RT}$  (where, as in Eq. 3.1.1,  $R$  is the specific gas constant). At flyby conditions, this gives  $\dot{m}_{up} = 4.4 \times 10^{-3}$  kg m<sup>-2</sup> s<sup>-1</sup>, about 10,000 times larger than the net flux. Second, the timescale for N<sub>2</sub> to relax toward an equilibrium pressure is very short. By hydrostatic equilibrium and kinetic theory,  $dp/dt = g\dot{m} =$   
 730  $-(p - p_{eq})g/\sqrt{2\pi RT}$ , where  $g$  is the surface gravity. This equation is one of relaxation to an equilibrium,  $p = p_{eq} + (p(t_0) - p_{eq})\exp(-(t - t_0)/\tau)$ , with a timescale  $\tau = \sqrt{2\pi RT}/g$ . For Pluto's flyby conditions, this timescale is 7 minutes, about 1300 times shorter than Pluto's 6.4-day rotation. Third, the isothermality of the surface requires that the sublimation wind,  $v_{sw}$ , be much smaller than the sound speed,  $v_s = \sqrt{\gamma RT}$ , where  $\gamma$  is the adiabatic constant (Trafton & Stern 1983; Spencer et al. 1997). The sublimation wind is the wind needed to transport atmosphere from areas of greater to lesser insolation. For an ideal surface covered uniformly with N<sub>2</sub> ice, if the sub-solar latitude is at the pole, then the sublimation wind can be calculated by imagining a girdle at the equator with area equal to the circumference times the scale height (Trafton & Stern 1983; Spencer et al. 1997). Multiplying this area  
 740 by the number density and sublimation wind speed gives a mass flux, which must equal the net condensation in the winter hemisphere. Different subsolar latitudes and different choices of where to place the girdle affects the calculated sublimation wind. The maximum sublimation wind is smaller for equator-

to-pole flow than for pole-to-pole flow. This effect can be expressed by  $v_{sw} = 4\xi\epsilon\sigma T^4 r_0 g / (Lp_{eq})$ , where  $r_0$  is Pluto's surface radius, and  $\xi$  is a unitless constant that varies between 0.044 and 0.30 depending on illumination (Young et al. 2019; Stern & Trafton 2008), giving  $v_{sw} \approx 0.20 \text{ m s}^{-1}$  at the flyby, in rough agreement with the meridional speeds in Forget et al. (2017). At  $T = 36.9 \text{ K}$ , the sound speed,  $v_s$ , is  $123 \text{ m s}^{-1}$ , or  $\sim 550$  times larger than the sublimation speed.

750 This picture of an isothermal, isobaric surface breaks down with lower temperatures and pressures. Spencer et al. (1997) and Trafton & Stern (1983) described the breakdown of the global atmosphere at temperatures below  $\sim 30.5 \text{ K}$ , for  $p_{eq} = 6.4 \text{ mPa}$  for pole-to-pole flow (e.g., from the sub-solar to the anti-solar point). At that temperature, the atmosphere is still in local equilibrium with the ice: the timescale for equilibrating is still only 7 minutes, and the imbalance between the upward and downward mass flux is only 1 part in 150. However,  $\text{N}_2$  still must flow from latitudes of greater insolation to latitudes of lesser insolation. A thinner atmosphere requires faster sublimation winds to transport the same mass. For a surface covered completely with volatiles, at  $30.5 \text{ K}$ , the sound speed is only  $\sim 5$  times larger than the sublimation wind, which is too small to maintain an isothermal surface (Stern & Trafton 1983; Trafton 1984). At these low pressures, the conditions are more like Io's atmosphere, where the atmosphere is collisional, super-sonic winds flow, and the principle volatile is transported across the globe, but the rate of transport is not enough to regulate the surface temperature. For such cases, simplified hydrodynamics  
 760 equations can be applied, as has been done for Io (Ingersoll et al. 1985), Eris (Hofgartner et al. 2019), and previously for Pluto and Triton under the assumption of a thick  $\text{CH}_4$  atmosphere (Trafton & Stern 1983; Trafton 1984). As we discuss in Section 4, for many assumptions of albedo, emissivity, and thermal inertia, Pluto's atmosphere stays global throughout its entire orbit.

### 3.2.2 Surface heterogeneity and the $\text{N}_2$ cycle

It was well established that Pluto's surface was varied in albedo and composition before the New Horizons flyby, and confirmed spectacularly by the LORRI and Ralph instruments of New Horizons. An inhomogeneous  $\text{N}_2$  ice distribution lowers the pressure at which an atmosphere transitions from global to local, because a smaller net sublimation or condensation flux needs to move across the planet.

770 Because Pluto's  $\text{N}_2$  ice is not spatially uniform, the mean insolation onto the  $\text{N}_2$  ice varies with subsolar latitude and longitude, altering  $\bar{\mu}$ . On diurnal timescales, the energy balance is controlled by the diurnally averaged insolation onto the  $\text{N}_2$  ice, not the instantaneous insolation, because the latent heat required to increase the column mass of the atmosphere in response to the changing surface temperature dampens how quickly temperatures can change over a rotation. Young (2014, 2017) defined a unitless parameter analogous to the Spencer thermal parameter that dampens the change in surface temperature because of the "atmospheric breathing," which can be written as  $\Theta_A = (\omega/fg)(d \ln p_{eq}/d \ln T)Lp_{eq}/(\epsilon\sigma T^4)$ , where  $f$  is the fraction of the surface covered by volatiles. For the conditions at flyby, and using  $f \approx 1/2$ ,  $\Theta_A \approx 2300$ . Even near the limit of a global atmosphere, at  $6.4 \text{ mPa}$ ,  $\Theta_A \sim 40$ . For large  $\Theta_A$ , the peak-to-peak temperature is smaller by a factor of  $4/\Theta_A$  compared with what it would be if the thermal emission were in instantaneous equilibrium with the average insolation. In Pluto's current configuration, the  $\text{N}_2$  ice  
 780 temperatures warm up and cool off by only mK as Sputnik Planitia—the bulk of Pluto's known  $\text{N}_2$ —approaches local noon or midnight.

On seasonal timescales, the mean insolation on the N<sub>2</sub> ice is greatly influenced by the large reservoir of N<sub>2</sub> in Sputnik Planitia, which is primarily in the northern hemisphere, centered on 15° N. In Pluto's current orbit, this implies the greatest insolation happens partway between perihelion and summer solstice, near the time of maximum insolation at 15° N (e.g., Johnson et al. 2020; see Fig 6, middle left).

When perihelion coincided with northern summer solstice, 0.9 My ago, each Pluto orbit experienced a period of short and intense insolation onto Sputnik Planitia. In contrast, when perihelion coincided with southern summer solstice, 2.3 My ago, the competing effects of heliocentric distance and subsolar latitude nearly balance, leading to mild changes in temperatures over a Pluto orbit.

790 And how do volatile cycles lead to Pluto's surface heterogeneity? The areas not covered by N<sub>2</sub> are seen by New Horizons to be CH<sub>4</sub>-rich (Section 3.4), or covered by the non-volatiles: H<sub>2</sub>O and a dark material, presumably tholin (Section 3.5). Areas covered with N<sub>2</sub>-rich ice can lose N<sub>2</sub> through preferential sublimation, first becoming CH<sub>4</sub>-rich ice and then revealing a substrate of H<sub>2</sub>O or other material. Sublimation and processing by UV or energetic particles could, perhaps, form a surface lag deposit of non-volatile organics. Conversely, areas will become new N<sub>2</sub> condensation sites if they become colder than the equilibrium N<sub>2</sub> temperature for the local surface pressure (See Section 3.5). Because N<sub>2</sub> ice has high albedo and the non-volatiles are generally low albedo, heterogeneity, once established, maintains itself in a positive feedback (Young 1993; Earle et al. 2018a).

### 3.2.3 Impact of topography on the N<sub>2</sub> cycle

800 If Pluto's surface were entirely flat (i.e., had no topographic relief), then those areas that were covered by N<sub>2</sub> ice would be nearly isothermal across the globe, due to the transport of latent heat of sublimation from areas with more insolation to areas with less insolation. But Pluto is far from flat, as revealed by New Horizons imaging (Stern et al. 2015; Moore et al. 2016; Schenk et al. 2018), with altitudes as much as 5 km above and below the mean level (see Section 2.2). The altitude compared to the mean level affects the stability of N<sub>2</sub> ice. Hydrostatic equilibrium requires that the surface pressure is higher at lower altitudes, and so therefore is the equilibrium ice temperature. Since the N<sub>2</sub> ice and gas reach equilibrium quickly, the actual N<sub>2</sub> ice temperature will also be warmer at low altitudes and cooler at high altitudes. The warmer, low-altitude N<sub>2</sub> ice radiates more heat to space than does the cooler, high-altitude N<sub>2</sub> ice. To maintain local conservation of energy, vapor-pressure equilibrium, and hydrostatic equilibrium, the difference in thermal radiation needs to be balanced by latent heat of sublimation through the increased deposition of volatile ice at low altitude and the increased sublimation at high altitude. Consequently, N<sub>2</sub> ice tends to accumulate and be more stable at low altitude.

810 This atmospheric-topographic process explains why N<sub>2</sub> ice preferentially accumulates in the depressions on Pluto. The atmospheric-topographic process was described by Trafton et al. (1998) and Stansberry et al. (2014), and was used by Trafton & Stansberry (2015), Bertrand & Forget (2016), Bertrand et al. (2018, 2019), and Young et al (2017). Trafton and Stansberry (2015) quantified the effect of topography by considering idealized mountains and valleys, based on preliminary topographic relief results from the New Horizons flyby.

820 Table 1 updates the results of Trafton and Stansberry (2015) using improved parameters from New Horizons, illustrating the above processes and the extension of volatile transport to the vertical dimension

for day-night, seasonal, or astronomical cycles. Table 1 shows the ice temperature and mass transport flux for topographic relief of  $\pm 4$  km at the subsolar point and dark side (night or winter) at perihelion, during the New Horizons flyby, and at 42 AU. In the model, Pluto's atmosphere is supported by the vapor pressure of  $N_2$  ice in global radiative equilibrium at a reference level taken to be near the mean of the topographic radial variations (approximating that of the mean level of volatile ice) with parameters determined from the New Horizons flyby and adjusted for other solar distances, as needed. The topographic variations are measured with respect to a  $N_2$  atmospheric reference level at  $p_{ref} = 1.15$  Pa (Hinson et al. 2017), which, in the absence of topographic relief, would correspond to an isothermal ice surface in global radiative balance and vapor phase equilibrium near 36.9 K. The atmospheric pressure at the topographic ice surface is evaluated by  $p_s = p_{ref} \exp(-h/H_{ref})$ .  $H_{ref}$  is the effective pressure scale height spanning the approximately isothermal topographic relief and  $h$  is the displacement of the surface from the reference layer, positive upwards.  $H_{ref} = 18$  km during the New Horizons flyby (Hinson et al. 2017). The temperature at the reference level  $T_{ref}$  is determined from  $p_{ref} = p_{eq}(T_{ref})$ ; but for other solar distances,  $T_{ref}$  and the scale height are varied according to the insolation flux (weighted by Tryka et al. 1993; 1994 near perihelion). The temperature just above the surface,  $T_s$ , is determined by  $p_s = p_{eq}(T_s)$  since the atmospheric column is supported hydrostatically by the ice equilibrium vapor pressure.  $T_i$  is the local ice temperature. Unit emissivity is assumed, and an ice albedo  $A = 0.85$  (Burrati et al. 2017). The equation that balances the difference between the one-way thermal fluxes from ice evaporation and sticking atmospheric gas against the difference between the local absorbed insolation and ice radiation fluxes is given, for a unit sticking coefficient, by Eq (3):

$$(Eq. 3) \quad L\dot{m} = L \left( \frac{p_{eq}(T_i)}{\sqrt{2\pi RT_i}} - \frac{p_{eq}(T_s)}{\sqrt{2\pi RT_s}} \right) = \mu(1 - A) \frac{S_{1AU}}{\Delta^2} - \epsilon \sigma T_i^4$$

The cosine of the incidence angle,  $\mu$ , is 1 for the subsolar point and 0 for the dark side (night or arctic winter).

Table 1. Topographic temperature differences and transport of  $N_2$  ice on Pluto

	Perihelion: $T_{ref} = 38$ K		31.9 AU: $T_{ref} = 36.9$ K		42 AU: $T_{ref} = 32.2$ K	
Dark side	$T_i$ (K)	$\dot{m}$ ( $kg\ m^{-2}\ s^{-1}$ )	$T_i$ (K)	$\dot{m}$ ( $kg\ m^{-2}\ s^{-1}$ )	$T_i$ (K)	$\dot{m}$ ( $kg\ m^{-2}\ s^{-1}$ )
Mountain (+4 km)	37.6203	$-0.45 \times 10^{-6}$	36.5361	$-0.40 \times 10^{-6}$	31.8647	$-0.23 \times 10^{-6}$
Valley (-4 km)	38.3874	$-0.48 \times 10^{-6}$	37.2791	$-0.43 \times 10^{-6}$	32.4563	$-0.25 \times 10^{-6}$
Sub-solar	$T_i$ (K)	$\dot{m}$ ( $kg\ m^{-2}\ s^{-1}$ )	$T_i$ (K)	$\dot{m}$ ( $kg\ m^{-2}\ s^{-1}$ )	$T_i$ (K)	$\dot{m}$ ( $kg\ m^{-2}\ s^{-1}$ )
Mountain (+4 km)	37.6205	$0.44 \times 10^{-6}$	36.5365	$0.40 \times 10^{-6}$	31.8700	$0.23 \times 10^{-6}$
Valley (-4 km)	38.3875	$0.40 \times 10^{-6}$	37.2793	$0.36 \times 10^{-6}$	32.4595	$0.21 \times 10^{-6}$

Table column headings are the ice temperature ( $T_i$ ), and the local vertical mass flux ( $\dot{m}$ ), positive for sublimation. Table 1 quantifies the preferential accumulation of  $N_2$  ice in the depressions on Pluto, as predicted by Trafton et al. (1988), a result that has since been observed. Note that the dark side deposition flux is greater in the valleys than in the mountains, while the subsolar sublimation flux is greater in the mountains than in the valleys. This reflects the net volatile transport to the dark hemisphere, as well as to

local depressions. The sublimation winds arise to maintain global hydrostatic equilibrium. Finally, note that the volatile transport between hemispheres is balanced mountain to mountain, but is unbalanced valley to valley in favor of deposition into the dark side valleys. Net deposition in the topographic depressions is more efficient than net deposition at higher altitudes at maintaining the dark side temperature (i.e., warming the surface). Conversely, net sublimation from the mountains is more efficient than from the depressions for maintaining the day side temperature (i.e., cooling the surface).

At perihelion conditions, the equilibrium temperature in the valley is 0.77 K warmer than on the mountain, and that the night-time condensation rate is higher in the valley by  $3.7 \times 10^{-8} \text{ kg m}^{-2} \text{ s}^{-1}$ , equivalent to a rate of  $0.117 \text{ cm year}^{-1}$  or 30 cm per Pluto year, or about  $3.6 \text{ cm (Pluto year)}^{-1} \text{ km}^{-1}$ .

Young et al. (2017) found a similar result, that 1.5-km deep depressions at  $57^\circ \text{ N}$  are 0.13 K warmer than the surrounding uplands, with a net condensation rate of 5 cm per Pluto year, also giving  $3 \text{ cm (Pluto year)}^{-1} \text{ km}^{-1}$ . Over one Pluto year,  $\text{N}_2$  accumulation at depth can affect albedo, and thus energy balance. It may also be detectable in near-IR spectra through wavelength shifts in the  $\text{CH}_4$  absorption. It is likely too small to affect the detectability of  $\text{N}_2$  by its weak  $2.15\text{-}\mu\text{m}$  feature.

The enhanced condensation rate fills up depressions at a rate proportional to the depth of the depression, or  $\dot{h} = h/t_{\text{infill}}$ . The scale factor can be found from simple scale analysis (Trafton et al. 1998). In a depression of depth  $h$ , the pressure will be higher because of hydrostatic equilibrium, by  $dp/dz = -p/H$ , where  $H = RT/g$  is the pressure scale height, and  $g$  is the gravitational acceleration,  $0.62 \text{ m s}^{-1}$ . Since the depressions are small, typically a few km, the increase in the pressure will depend only weakly on the details of the atmospheric temperature structure. The equilibrium temperature will also be higher, according to the Clausius-Clapeyron equation,  $dp_{\text{eq}}/dT_{\text{eq}} = (p/T)(L/RT)$ . Together, the equilibrium temperature follows the wet adiabat, with lapse rate  $-dT_{\text{eq}}/dz = \Gamma_w = T_{\text{eq}}g/L$ . For Pluto at 37 K,  $\Gamma_w \approx 0.09 \text{ K km}^{-1}$ . The surface at the bottom of the depression, being warmer by  $\Delta T = \Gamma_w h$ , emits more thermal radiation than the surface at the top of the depression by  $\Delta F = 4\varepsilon\sigma T^3 \Gamma_w h$ , or, for  $T = 37 \text{ K}$  and  $\varepsilon = 1$ , an additional energy flux of  $\Delta F = 1.05 \text{ mW m}^{-2}$  per 1 km of depth. If the absorbed insolation is the same at the top and bottom of a depression, and ignoring thermal conduction, then the additional thermal emission drives a larger condensation rate (Trafton et al. 1998; Trafton & Stansberry 2015). We divide by the latent heat,  $L$ , to get mass flux (mass per area per time), and again by density  $\rho$  ( $\sim 1 \text{ g cm}^{-3}$ ) to get the rate at which a depression fills up:  $\dot{h} = \Delta F/(\rho L)$ . Altogether, the infilling time constant is

$$\text{(Eq. 4)} \quad t_{\text{infill}} = \frac{\rho L^2}{g4\varepsilon\sigma T^4}$$

The infilling can be expressed as a decaying exponential,  $h(t) = h(0) \exp(-t/t_{\text{infill}})$ , demonstrating that  $t_{\text{infill}}$  is a characteristic timescale for infilling that is independent of the depression depth. For temperatures of 30 to 45 K,  $t_{\text{infill}}$  is 19 to 3 Million years. That is, scale analysis predicts that it took  $\sim 7$  Myr to fill up Sputnik Planitia from a depth of 5.5 km to its current depth of 2 km. The infilling of the deep Sputnik Planitia basin could also be explained by this process (independent of the Milankovitch cycles), with  $\text{N}_2$  filling the basin in simulations in typically in 10 My (Bertrand and Forget 2016; Bertrand et al. 2018).

Comparing the infilling timescale to the rate of glacial flow (Fig. 9), we see that infilling of depressions by atmospheric transport is more important than glacial flow on regional to global scales ( $100$ 's to  $1000$ 's

890 of km), both because of timescale arguments, and because the atmospheric transport can fill in depressions even when high topography separates the depression sinks from N<sub>2</sub>-ice sources.

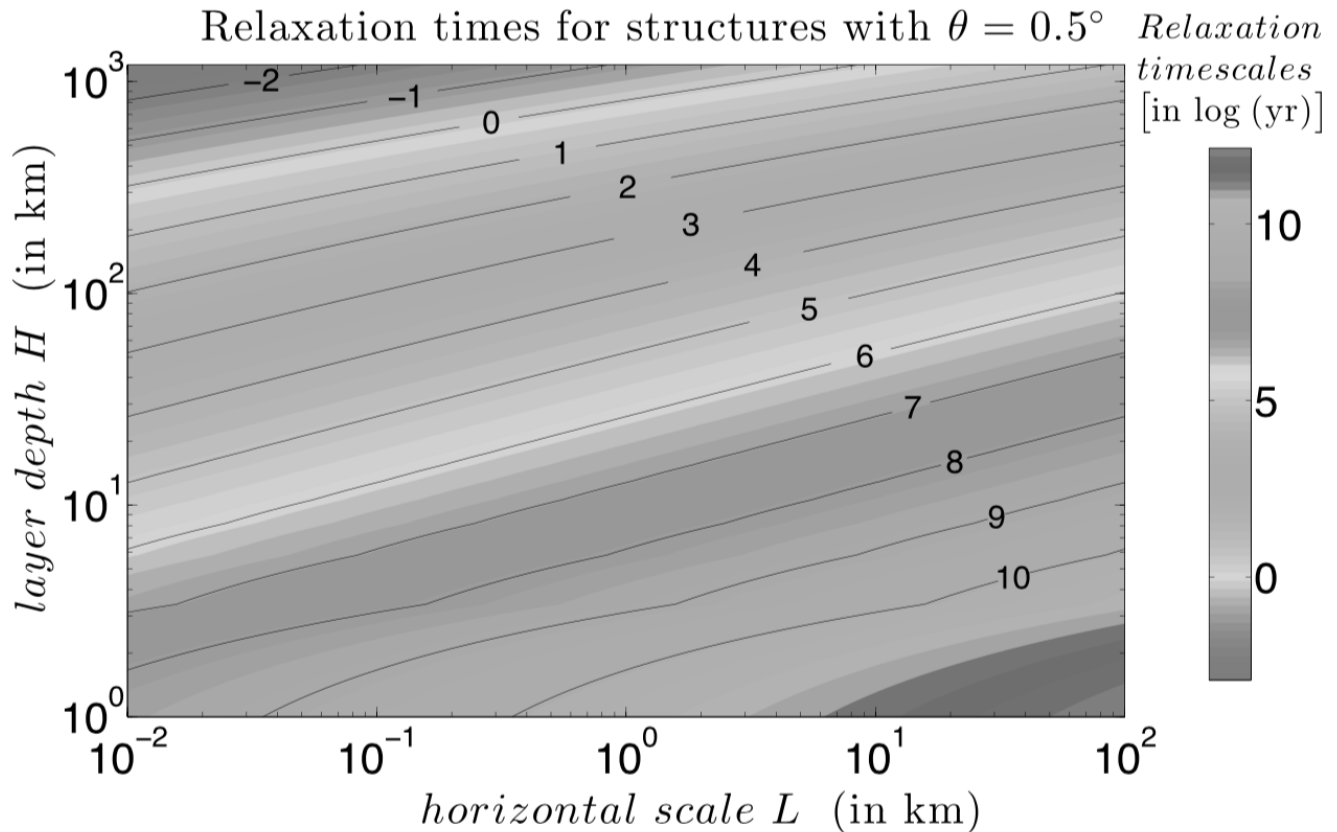


Fig. 9 From Umurhan et al. 2017 (see Umurhan et al. 2017 for color version). Relaxation timescale for glacial flow over shallow slopes. The timescale for filling in depressions by atmospheric transport at current Pluto temperatures is about  $10^7$  years. Thus, atmospheric transport is quicker (more efficient) than glacial flows for shallow deposits or deposits separated by large distances. Moreover, atmospheric transport operates even when the source and sink areas are discontinuous, as is more likely for shallow deposits and large separations.

900

### 3.3 CO cycle

CO is almost as volatile as N<sub>2</sub>, but it is found only in trace amounts in the atmosphere as a consequence of its low mixing ratio in the N<sub>2</sub>-rich ices and the ternary phase diagram (Tan & Kargel 2018). No CO-rich ices have been detected on Pluto from either New Horizons or ground-based observations, and the strong CO bands are seen co-located with the N<sub>2</sub>-rich ice (Schmitt et al. 2017). This is also seen in how CO and N<sub>2</sub> vary with sub-observer longitude in ground-based spectra, for both Pluto (Grundy et al. 2013) and Triton (Holler et al. 2016). This is also the case for Triton (Tegler et al. 2019), on which a rarely seen N<sub>2</sub>-CO combination band at 2.239  $\mu\text{m}$  was detected, indicating simultaneous excitation of nearby N<sub>2</sub> and

CO in ice. The existence of the band indicates that CO and N<sub>2</sub> molecules are intimately mixed in the ice  
 910 on Triton, rather than existing as separate regions of pure CO and pure N<sub>2</sub> deposits.

### 3.4 CH<sub>4</sub> cycle

Great progress has been made on the equilibrium behavior of N<sub>2</sub>:CO:CH<sub>4</sub> mixtures (Trafton 2015; Tan  
 and Kargel 2018). However, CH<sub>4</sub> is observed to be in disequilibrium on Pluto, and the CH<sub>4</sub> cycle is still  
 not well understood. The cycles of N<sub>2</sub> and CH<sub>4</sub> are entwined, and the drivers of disequilibrium of CH<sub>4</sub>  
 occurs on multiple timescales (Young et al. 2019; Trafton et al. 2019). Methane can condense at warmer  
 temperatures than N<sub>2</sub>. Since fresh ice of either species is probably bright, areas of high-albedo CH<sub>4</sub> may  
 then be able to cool down enough to allow N<sub>2</sub> condensation. This process could explain the presence of  
 N<sub>2</sub>-rich deposits observed by New Horizons outside the deepest depressions, such as Eastern Tombaugh  
 Regio, if the deposited N<sub>2</sub> were also high-albedo (Bertrand et al. 2019). Also, the CH<sub>4</sub> cycle affects the  
 920 atmospheric chemistry. In Pluto's current atmosphere, the first step in haze production is the absorption  
 of Lyman- $\alpha$  by CH<sub>4</sub>. If the atmosphere becomes optically thin to Lyman- $\alpha$ , because of lower CH<sub>4</sub> mixing  
 ratio or smaller surface pressure, this will fundamentally change haze formation. Since haze can alter  
 surface properties (albedo, emissivity), this can have a positive or negative feedback on volatile cycles.  
 Processing of the surface by energetic particles or UV photons can also affect surface properties (see  
 reviews by Salama 1998 and Strazulla 1998). Thus, the CH<sub>4</sub> cycle is important for understanding how  
 Pluto works.

Models of the CH<sub>4</sub> volatile cycle should strive to explain the following observed phenomena. (1) The  
 atmospheric mixing ratio of CH<sub>4</sub> is ~0.3% (Young et al. 1997; Young et al. 2018), 10 to 100 times higher  
 than expected by 3-phase equilibrium (where the three phases are N<sub>2</sub>-rich ice saturated with CH<sub>4</sub>, CH<sub>4</sub>-  
 rich ice saturated with N<sub>2</sub>, and vapor). (2) The dilution of CH<sub>4</sub> in the N<sub>2</sub>-rich terrains is only ~0.3 to 0.5%  
 930 (Protopapa et al. 2017; Douté et al. 1999), rather than the ~4% expected for 3-phase equilibrium. (The  
 dilution of N<sub>2</sub> within CH<sub>4</sub> is not measurable from near-IR spectra). (3) CH<sub>4</sub>-rich terrains dominate the  
 surface northward of 55° N, with significant CH<sub>4</sub>-rich terrain at low northern latitudes (20°N to 35°N)  
 (Protopapa et al. 2017; Schmitt et al. 2019). (4) The fraction of CH<sub>4</sub>-rich ice is slightly larger in northern  
 Sputnik Planitia, where the dilution of CH<sub>4</sub> in N<sub>2</sub>-rich ice is also larger (Protopapa et al. 2017; Schmitt et  
 al. 2019). (5) CH<sub>4</sub> is seen near the equator in eastern Tombaugh Regio, and in the Bladed Terrain. (6) CH<sub>4</sub>  
 is seen at high altitude, particularly striking on Pigafetta Montes (previously termed Enrique Montes).

#### 3.4.1 Enhanced CH<sub>4</sub> atmospheric mixing ratio

The enigma of Pluto's high atmospheric CH<sub>4</sub> mixing ratio has been recognized since the early models  
 of atmospheric energy balance, and since gaseous CH<sub>4</sub> was first discovered on Pluto (Lellouch et al. 1994;  
 940 Stansberry et al. 1996b; Young et al. 1997; Spencer et al. 1997; Trafton et al. 1998). In the context of  
 observations by New Horizons and new N<sub>2</sub>-CO-CH<sub>4</sub> thermodynamics, the observed atmospheric CH<sub>4</sub>  
 mixing ratio (0.28% to 0.35%; Young et al. 2018) is much higher than the CH<sub>4</sub> mixing ratio for 3-phase  
 equilibrium (0.003% to 0.013%; Tan and Kargel 2018; Young et al. 2019). As reviewed in Trafton et al.  
 (1998), two models were proposed that alternatively explain the observations, termed "detailed balance"  
 (Trafton 1990) and "methane patch" (Stansberry et al. 1996b).

950 The term “detailed balance” refers to a near-balance between the competing processes of sublimation and condensation on the molecular scale, all occurring in a state near thermal equilibrium, where every kinetic ice-gas transition at the surface is balanced by its inverse transition. Owing to the coupling of hydrostatic and phase equilibrium in this model, a thin layer of CH<sub>4</sub>-rich ice is maintained dynamically on the surface of the volatile ice. In this model, CH<sub>4</sub>- and N<sub>2</sub>-rich ice in the layer are separately in phase equilibrium, where their equilibrium vapor pressures balance the atmospheric partial pressures at the surface. During net sublimation or deposition, this solid layer “rides” on the ice surface, with its molecular membership continuously changing. The thickness of the layer is limited by the depth to which it interacts with the atmosphere. A surface discontinuity in the ice composition thus results from satisfying hydrostatic and phase equilibrium simultaneously. This detailed balance layer may be too thin to be detected spectroscopically.

960 N<sub>2</sub> may diffuse through this layer during net sublimation. However, its vapor pressure will be reduced by the ratio of the mole fraction of N<sub>2</sub> at the surface vs. below the layer. With fewer N<sub>2</sub> molecules on the surface, the N<sub>2</sub> vapor pressure must be lower. Since N<sub>2</sub> is the dominant species in Pluto’s atmosphere, the “detailed balance” model predicts that the total atmospheric pressure could be smaller than that over pure N<sub>2</sub> ice by one or two orders of magnitude. Take for example CH<sub>4</sub>-rich ice at 38 K, for which the CH<sub>4</sub> equilibrium pressure is 0.17 mPa (Fray & Schmitt 2009). For a 0.3% gaseous CH<sub>4</sub> mixing ratio and CH<sub>4</sub>-ice at 38 K, the N<sub>2</sub> pressure would be suppressed by a factor of 49, reduced from a pure vapor pressure of 2.2 Pa to a partial pressure of only 0.045 Pa (Tan, personal communication). But the measurements of Pluto’s actual surface pressure and radius from the REX Radio Experiment (Hinson et al. 2017) is consistent with a surface in equilibrium with N<sub>2</sub>-rich or pure N<sub>2</sub> ice. How much could the N<sub>2</sub> pressure be reduced and still be in equilibrium? As discussed in Section 2.1.2, the N<sub>2</sub> ice temperature is less than 41 K ( $p_{eq} = 10.9$  Pa) from the shape of the 2.15 μm feature, and the 3-σ lower limit on the surface pressure was measured to be 0.9 Pa, for a reduction of pressure by at most a factor of 12.

970 Calculations of the three-phase equilibrium state of Pluto’s N<sub>2</sub> and CH<sub>4</sub> ice vs. temperature by Tan (Young et al. 2019), based on the EOS of Tan & Kargel (2018), revealed an equilibrium atmospheric CH<sub>4</sub> ratio several orders of magnitude lower than the ~0.3% observed (Young 2018), implying that Pluto’s ice is not in a state of three-phase thermal equilibrium, where both saturated phases of N<sub>2</sub> and CH<sub>4</sub> exist with the atmospheric gas phase. Up to this time, the equation of state for these ices was unknown, so vapor pressures of the solid solution were approximated by Raoult’s law, which was, in some instances, an oversimplification given the easily saturated solid phases. Using the EOS of Tan & Kargel (2018) and the detailed balancing model, Trafton et al (2019) extended this calculation to the two-phase equilibrium case, covering the N<sub>2</sub>-rich ice with an unsaturated CH<sub>4</sub>-rich layer. They confirmed the disequilibrium for CH<sub>4</sub>:  
 980 The observed partial pressure of Pluto’s CH<sub>4</sub> remained far in excess of the two-phase equilibrium CH<sub>4</sub> vapor pressure in this model. The CH<sub>4</sub>-rich layer would have to have a temperature of 42.5 K to explain the observed mixing ratio. This disequilibrium is likely a result of the much lower volatility of CH<sub>4</sub> than N<sub>2</sub>. Moreover, as a minor constituent, CH<sub>4</sub> gas may not be fully in hydrostatic equilibrium.

The CH<sub>4</sub> patch model (Stansberry et al. 1996b) considers the impact on the atmospheric CH<sub>4</sub> mixing ratio of pure or CH<sub>4</sub>-rich areas, perhaps 15 K warmer than the N<sub>2</sub> ice temperature. As a minor species, the

CH<sub>4</sub> mass flux is not given by energy balance (Eq. 2) or by the Knudsen-Langmuir expression, but by turbulent diffusion of CH<sub>4</sub> through N<sub>2</sub>, Eq. 5:

$$(Eq. 5) \quad \dot{m} = -\rho U_* C_m (\chi_z - \chi_0),$$

where  $\rho$  is the atmospheric density at the surface,  $\chi_z$  is the atmospheric molar mixing ratio of CH<sub>4</sub> at a level near the surface,  $z$  (described below),  $\chi_0$  is the atmospheric molar mixing ratio in equilibrium with the surface (that is, the equilibrium partial pressure of CH<sub>4</sub> at the local surface temperature and composition divided by the local surface pressure,  $\chi_0 = p_{eq,CH_4}(T)/p_s$ ),  $U_*$  is the friction velocity, and  $C_m$  is the mass transfer coefficient. Forget et al. (2017) uses a similar formulation,  $\dot{m} = -\rho U_1 C_d (q_1 - q_0)$ , where  $U_1$  is the horizontal wind,  $C_d$  is the drag coefficient computed for the first atmospheric layer, and  $q_1$  and  $q_0$  are the mass mixing ratios at the first atmospheric layer and at the surface, respectively, defined by  $q = (\mu_{CH_4}/\mu_{N_2})\chi$ , where  $\mu$  is the molecular weight of CH<sub>4</sub> or N<sub>2</sub>. Stansberry et al. (1996b) and Forget et al. (2017) took different approaches to the choice of  $z$ . Stansberry et al. (1999b) integrated the empirical expressions used by Monin-Obukhov similarity theory from the surface to  $z$  to find  $C_m$ . The upper boundary,  $z$ , was chosen to be large enough that the computed  $C_m$  was insensitive to the choice of  $z$ . They used  $z = 2$  km, which was much larger than the depth of the sublayer dominated by eddy diffusion ( $\sim 14$  cm). Forget et al. (2017) explicitly computed the exchange very near the surface. In their model,  $z$  is the altitude of the first layer of the 3-D GCM, or 7 m.

For typical values of  $U_* C_m$ , turbulent diffusion is about 2000 to 10,000 times slower than Knudsen-Langmuir sublimation (as used by Moore et al. 2018). The observed atmospheric mixing ratio at the time of the New Horizons flyby was  $\chi_z \sim 0.3\%$ , and models typically predict  $\chi_z \sim 0.001\%$  to 1% (Bertrand et al. 2019). While modelers (Stansberry et al. 1996; Forget et al. 2017; Bertrand et al. 2019) have not yet applied the new EOS results, this will have little effect on the calculated mass flux from Eq. 5. First consider the current atmosphere above N<sub>2</sub>-rich ice. Even with CH<sub>4</sub> saturated in N<sub>2</sub>-rich ice, the EOS gives atmospheric mixing ratios of  $\chi_0 \sim 50$  ppm; smaller mixing ratios or the (inappropriate) use of Raoult's law will only decrease this value. Since  $\chi_z \approx 0.3\% \gg \chi_0$ , the deposition rate onto N<sub>2</sub>-rich ice calculated in Eq. 5 depends negligibly on the value of  $\chi_0$ . For sublimation of CH<sub>4</sub> from warm CH<sub>4</sub>-rich patches,  $\chi_0$  is calculated from the ratio of CH<sub>4</sub> partial pressure at some elevated temperature to the local surface pressure (e.g., the REX measurement of 1.15 Pa). Sublimation would occur for pure CH<sub>4</sub> at 42.1 K or hotter, but it is thermodynamically unlikely that pure CH<sub>4</sub> exists on Pluto. If the CH<sub>4</sub>-rich ice were saturated with N<sub>2</sub>, the calculated critical temperature for CH<sub>4</sub> sublimation would be 42.4 K, only 0.3 K warmer than if the CH<sub>4</sub>-rich ice were pure. Considering the uncertainties in albedo and emissivity, this is a small difference. At just a few degrees warmer,  $\chi_0 \gg \chi_z$  for all pure CH<sub>4</sub> or CH<sub>4</sub>-rich terrains.

Observations appear to support some version of a warm CH<sub>4</sub> patch model: New Horizons directly detected distinct areas of CH<sub>4</sub>-rich and N<sub>2</sub>-rich ice (Schmitt et al. 2017; Protopapa et al. 2017; Moore et al. 2018); and models of globally isothermal N<sub>2</sub>-rich ice and locally warmer CH<sub>4</sub> ice are consistent with ISO, Spitzer, and Heschel thermal measurements (Lellouch et al. 2000, 2011, 2016). Because Pluto's thermal light curve is likely to be heavily influenced by the thermal contrast between the non-volatile and volatile terrains, it will be useful to model existing or new thermal measurements in light of New Horizons observations of albedo and surface composition, and to model separate thermal inertias for non-volatile

and CH<sub>4</sub>-rich areas. In this context, there is no mystery in the observed atmospheric methane mixing ratio, because there are many CH<sub>4</sub>-rich deposits that are too warm to allow much N<sub>2</sub> in them. Rather the enigma is why all CH<sub>4</sub> does not get permanently cold-trapped in cold N<sub>2</sub>-rich deposits.

1030 Stansberry et al. (1996b) showed that sublimation from warm CH<sub>4</sub>-rich patches was, in general, much more efficient than the condensation onto N<sub>2</sub>-rich areas, both because the mass transfer coefficient is larger for sublimation than condensation, but also because  $\chi_0$  increases exponentially with temperature. Equating the global integral of CH<sub>4</sub> sublimating from patches to the global integral of condensation, Stansberry et al. (1996b) showed cases for which a patch area covering only a few percent of Pluto's surface sufficed to explain atmospheric CH<sub>4</sub> mixing ratios between 0.2% and 1%, given N<sub>2</sub> ice at 38 - 40 K with warm CH<sub>4</sub> patches at 53-54 K. Colder N<sub>2</sub> ice temperatures and lower atmospheric mixing ratios favored smaller areas covered by the patches.

1040 However, Pluto's surface has CH<sub>4</sub> patches on regional scales, as deduced from Earth-based observations and confirmed by New Horizons (Schmitt et al, 2017; Protopapa et al. 2017). Trafton (2015) argued that continent-sized CH<sub>4</sub> patches are too big to be explained by the CH<sub>4</sub> patch model. This conclusion would also apply to Pluto's CH<sub>4</sub>-rich polar and high latitudes, for which the CH<sub>4</sub>-rich ice would need to be at ~42.5 K (Trafton et al. 2019) to explain the global CH<sub>4</sub> mixing ratio of ~0.3% (Young et al. 2018).

1050 Thus, some version of the CH<sub>4</sub> patch model remains a viable explanation of Pluto's CH<sub>4</sub> enhancement, as it is supported by the observed CH<sub>4</sub>-rich ices (Protopapa et al. 2017) and works well in some post-flyby models (Forget et al. 2017; Bertrand et al. 2019). However, small temperature deviations from thermal equilibrium are still capable of explaining Pluto's atmospheric CH<sub>4</sub> enrichment and surface pressure, in terms of warmer and cooler regional temperature deviations that give rise to the distinct CH<sub>4</sub>-rich and N<sub>2</sub>-rich ice deposits, respectively (Trafton et al. 2019). Thus, the detailed balance model may also play a role but with separate thermal equilibria for the N<sub>2</sub>-rich and CH<sub>4</sub>-rich ice, respectively, having different temperatures and possibly confined to specific regions or latitudes. But, the detailed balance model cannot explain the observed CH<sub>4</sub> enhancement in terms of global thermal equilibrium covering both N<sub>2</sub>-rich and CH<sub>4</sub>-rich ice deposits simultaneously.

### 3.4.2 Undersaturated CH<sub>4</sub> in N<sub>2</sub>-rich ices

1060 Because all three phases exist at Pluto (CH<sub>4</sub>-rich ice, N<sub>2</sub>-rich ice, and vapor), in equilibrium the CH<sub>4</sub>-rich ice would be saturated with a few percent N<sub>2</sub>, and the N<sub>2</sub>-rich ice would be saturated with a few percent CH<sub>4</sub>. This is not what was seen in Hapke modeling of the New Horizons observations (Protopapa et al. 2017), in which there is only ~0.3% to 0.5% CH<sub>4</sub> in N<sub>2</sub>-rich ice. The disequilibrium is aided by the longer timescale for equalizing CH<sub>4</sub> between vapor and ice. The equilibrium timescale is over a Pluto day in length because atmospheric CH<sub>4</sub> has to diffuse through N<sub>2</sub> (Young et al. 2019). While the long timescale can help maintain the disequilibrium, the initial cause of the disequilibrium is not yet clear. It is intriguing that the CH<sub>4</sub> mixing ratio in the atmosphere is the same as in the N<sub>2</sub>-rich ice. This might have been the case had the atmosphere been escaping while being replaced by the volatile reservoir, or subsequently condensing from a large atmospheric mass in the past. What is unclear is why this has not evolved toward equilibrium, and the answer may be a matter of timescales (Young et al. 2019).

### 3.4.3 Formation of CH<sub>4</sub>-rich ice

Outside of Sputnik Planitia, there is a striking latitudinal dependence of the CH<sub>4</sub>-rich ice. CH<sub>4</sub>-rich ice dominates from 20° N to 35° N and 55° N to 90° N, with N<sub>2</sub> dominating the intervening latitudes (Protopapa et al. 2017; Schmitt et al. 2017), with the interpretation that Pluto is showing two sublimation fronts, with N<sub>2</sub> subliming from low latitudes near equinox, and from high latitudes more recently (Fig. 6, Middle left).

1070 CH<sub>4</sub>-rich ice is also seen at high altitude in various locations (Fig. 2): on isolated mountaintops within Cthulhu, such as Pigafetta Montes; on crater rims and the edges of scarps west of northern Sputnik Planitia; on the uplands in the N<sub>2</sub>-rich latitudes east of northern Sputnik Planitia (the “smooth uplands” and “eroded smooth uplands” of Howard et al. 2019b); and on the low-latitude bladed terrains (Moore et al. 2018).

From the equilibrium phase diagram (Tan & Kargel 2018; Trafton et al. 2019), whether CH<sub>4</sub>-rich ice or N<sub>2</sub>-rich ice dominates locally depends on the direction that the thermodynamic state of the ice deviates from the globally set thermal equilibrium. When the state locally deviates isothermally to lower pressures relative to the global equilibrium hydrostatic pressure, or deviates isobarically to higher temperatures, the CH<sub>4</sub>-rich phase of ice forms as the local N<sub>2</sub>-rich ice sublimates. Conversely, opposite local deviations from global equilibrium drive the formation of the N<sub>2</sub>-rich ice phase, as the local atmosphere N<sub>2</sub> condenses.  
 1080 Thus, CH<sub>4</sub>-rich ice may form where N<sub>2</sub>-rich ice preferentially sublimates, such as at subsolar latitudes, where the insolation is greater, or for ice at high elevations, where the equilibrium temperature is lower. Pressure deviations could result from regional circulation patterns while temperature deviations could result from the arrival of winds warmed over broad non-icy areas that drive the regional formation of the CH<sub>4</sub>-rich phase – or from the arrival of cooler dense air, such as occurs at Sputnik Planitia, driving in the formation of the N<sub>2</sub>-rich phase there.

Another mechanism may be at play for equatorial CH<sub>4</sub>-rich deposits at altitude (Bertrand et al 2020b; see Chapter by Forget), involving an enhancement of atmospheric CH<sub>4</sub> (and therefore higher condensation rates of CH<sub>4</sub>) at higher altitudes. The New Horizons UV occultations cannot constrain this, since atmospheric CH<sub>4</sub> was too opaque to be measured below 80 km.

## 1090 3.5 H<sub>2</sub>O and tholin-rich areas

The nonvolatile areas of Pluto are warmer by 10 to 20 K than the N<sub>2</sub>-rich ice (and can be also warmer than the CH<sub>4</sub>-rich ice) because they tend to be covered by materials with a bolometric Bond albedo near 0.1 (Buratti et al. 2017), which is much lower than that of N<sub>2</sub>-rich areas. As nonvolatiles, they are not cooled by the latent heat of sublimation. A positive feedback can be established, in which dark areas can get warm and continue to stay free of volatiles, while bright areas stay cold, and become volatile condensation sites.

The temperature for non-volatile-covered areas are dictated by the insolation (including the effect of local slopes and shadowing), the albedo, the thermal inertia, and the emissivity. All areas with very low albedos are volatile free, but not all volatile-free areas have very low albedos. If the thermal inertia and the mean insolation are both high enough then the non-volatiles will remain clear over an entire Pluto orbit. Otherwise, if a nonvolatile area becomes colder than the mean N<sub>2</sub> ice temperature, then the nonvolatile will become condensation sites (so there should be no location colder than the global N<sub>2</sub> ice  
 1100

temperature adjusted for altitude). Because fresh N<sub>2</sub> or CH<sub>4</sub> ice is likely to be bright, new fresh frost may allow areas to remain cold even at summer seasons. In this way, the thermal inertia may be important for the creation of annual nitrogen deposits and the transition of annual deposits into perennial deposits.

## 4. A Review of Models

The processes controlling the volatile and climate cycles, described in Section 3, have been used to model the behavior of volatiles on Pluto over multiple timescales since the first volatiles were detected in Pluto spectra. In this section, we concentrate on those models with simulations of the cyclical or long-term evolution of Pluto’s volatiles. This section is roughly chronological, since there is a general pattern of new observations spurring new models of Pluto’s volatile cycles, leaving the field with new paradigms (Table 2).

Table 2. Models for volatile cycles and trends

Motivating Observations	Models of volatile evolution <sup>a</sup>	New paradigms of volatile evolution
CH <sub>4</sub> spectra	<b>TS:</b> Trafton 1980, 1981, 1984, 1989; Trafton & Stern 1983; Stern & Trafton 1984; Trafton et al. 1988; Stern et al. 1988.	Escape and replenishment of the atmosphere; vapor-pressure and hydrostatic equilibrium; mass & energy transport; conditions for a global atmosphere; atmospheric “laundering.”
Stellar occultation (1988); surface N <sub>2</sub> , CO, CH <sub>4</sub> (CH <sub>4</sub> -rich and diluted in N <sub>2</sub> -rich); surface heterogeneity; gaseous CH <sub>4</sub>	<b>TS:</b> Trafton 1989; 1990; <b>HP:</b> Hansen & Paige 1996 (HP96); <b>Other:</b> Young 1993; Stansberry & Yelle 1999;	Albedo feedback; two-volatile (N <sub>2</sub> /CH <sub>4</sub> ) interaction; N <sub>2</sub> emissivity and phase change; thermal inertia; loss of summer N <sub>2</sub> and the importance of sub-solar latitude.
Gaseous CH <sub>4</sub> , CO; surface N <sub>2</sub> , CO, CH <sub>4</sub> (variation with time); thermal emission; stellar occultations (2002 and beyond).	<b>TPM:</b> Lellouch et al. 2000, 2011, 2016; <b>HP:</b> Elliot et al. 2007; Bosh et al. 2015, Hansen et al. 2015; <b>VT3D:</b> Young 2012; 2013; Olkin et al. 2015; <b>LMD:</b> Vangvichith 2013; <b>TF/PlutoWRF:</b> Toigo et al. 2010; 2015; French et al. 2015.	Low thermal inertia (diurnal skin depth); high thermal inertia (seasonal skin depth); CH <sub>4</sub> variation (surface and gas); atmospheric “breathing.”
New Horizons flyby, including: Composition maps on geologic spatial scales; Surface radius; Atmospheric structure, composition, and surface pressure	<b>PlutoWRF:</b> Moores et al. 2017; <b>VT3D:</b> Young et al. 2015; Lewis et al. 2020; Johnson et al. 2020. <b>EB:</b> Stern et al. 2017, Binzel et al. 2017; Earle et al. 2017; 2018a; <b>LMD:</b> Forget et al. 2017; Bertrand & Forget 2016; Bertrand et al. 2018	Sputnik Planitia as equatorial reservoir; role of topography; geologic expression of volatile cycles; other paths for volatile transport; albedo feedback in the equatorial regions; Milankovitch cycles; question of southern N <sub>2</sub> ; puzzle of widespread CH <sub>4</sub> ; cold CH <sub>4</sub> ice enabling N <sub>2</sub> condensation.

---

(B18), 2019 (B19); Meza et al. 2019;

---

<sup>a</sup> Sorted by model category: TS: Papers by Trafton, Stern, and colleagues. HP: Papers by Hansen, Paige, and colleagues. TPM: Thermophysical models by Lellouch and colleagues. VT3D: 3-dimensional volatile transport model. LMD: Laboratoire de Météorologie Dynamique. TF: Papers by Toigo, French. EB: Papers by Earle, Binzel. PlutoWRF: National Center for Atmospheric Research (NCAR) Weather Research and Forecasting GCM. Other papers also mention volatile evolution. An emphasis is given in this table to papers with predictions of volatile behavior over various cyclical timescales.

#### 1120 4.1 Spurred by CH<sub>4</sub>: The first volatile transport models

Volatile transport models for Pluto were inspired by the detection of CH<sub>4</sub> frost on Pluto by Cruikshank et al. (1976), the large amplitude of Pluto's rotational lightcurve, and decade-long changes in Pluto's lightcurve with changes in sub-solar latitude. After the discovery of CH<sub>4</sub> ice on Pluto by Cruikshank et al. (1976), it was assumed that there would be a CH<sub>4</sub> atmosphere based on the volatility of CH<sub>4</sub>. Subsequent observations confirmed the detection of CH<sub>4</sub> absorption in spectra with increasingly better spectral resolution and data quality. Fink et al. (1980) reported an atmospheric CH<sub>4</sub> abundance of 27±7 m-Am (19.3±5.0 kg m<sup>-2</sup>; 12.0±3.1 Pa. Here and throughout we convert column densities in m-Am or kg m<sup>-2</sup> to pressures using the current best value of surface gravity,  $g = 0.62 \text{ m s}^{-2}$ ). Cruikshank & Silvaggio (1980) estimated a vertical column of ~7 m-A CH<sub>4</sub> (5.0 kg m<sup>-2</sup>; 3.1 Pa) for an atmosphere if all the observed absorption were gaseous, but concluded that it was impossible to derive a gas abundance from the data. The first generation of models studied the implications of either a massive CH<sub>4</sub> atmosphere, or a tenuous CH<sub>4</sub> atmosphere supported by the CH<sub>4</sub> ices, with or without another gas species. Although the CH<sub>4</sub> spectral signature turned out to be almost entirely due to the surface ice, not gas (Spencer et al. 1990; Young et al. 1997), a series of early models mainly by Trafton, Stern, and coauthors established some of the critical concepts for volatile transport on Pluto, and were motivators for the 1988 occultation observation that finally definitively detected the atmosphere.

The observed CH<sub>4</sub> spectral signature raised the challenge of volatile retention (See Chapter by Strobel et al.). By 1980, rough values of Pluto's mass and radius were available. Using a steady-state model of Pluto's atmosphere supported by the vapor pressure of CH<sub>4</sub> ice and a bolometric Bond albedo between 0.19 and 0.52 to constrain the ice temperature, Trafton (1980) concluded that Pluto's mass was too small to hold an isothermal CH<sub>4</sub> atmosphere in vapor equilibrium with an ice warmer than 45 K. The excess CH<sub>4</sub> would overflow the gravitational potential well ("blowoff") and escape from Pluto. Three solutions contributed to the resolution to this dilemma. First was the deduction that a heavier gas (such as Ar, N<sub>2</sub>, CO, or O<sub>2</sub>) must be present in greater abundance to reduce the scale height enough to gravitationally bind the atmosphere, and to provide a diffusive barrier great enough to slow the escape rate (Trafton 1980, 1981) — and, in fact, N<sub>2</sub> dominates over CH<sub>4</sub> in Pluto's atmosphere. The second was that Pluto's surface gravity is closer to 0.51 m s<sup>-2</sup> than 0.30 m s<sup>-2</sup> (Fink et al. 1980)—in agreement with the measured value of 0.62 m s<sup>-2</sup>. The third was that the blowoff predicted by the isothermal atmospheric escape model of Trafton (1980) would not occur in such a rapidly expanding atmosphere owing to adiabatic cooling at altitude (Hunten & Watson 1982). Once Hunten & Watson (1982) pointed this out, the relative retention of Pluto's

atmosphere was no longer in doubt; and the cold upper atmosphere, as measured by New Horizons, confirms that Pluto is not undergoing blowoff.

Seminal models describing the structure of the volatile atmospheres of Pluto and Triton (Table 2) assumed both hydrostatic equilibrium and thermodynamic equilibrium for the state of the volatile ice-atmosphere system. Some of these began by taking the Fink et al. (1980) measurement of a thick CH<sub>4</sub> atmosphere (e.g., Trafton & Stern 1983), while others considered a range of volatile gases (e.g., Stern & Trafton 1984). These papers established several key concepts.

1160 First, papers presented arguments for the presence of other volatiles (N<sub>2</sub>, Ar, CO, or O<sub>2</sub>) in addition to CH<sub>4</sub> (Trafton 1981; Stern & Trafton 1984). They discussed the retention and loss of various volatiles. Trafton et al. (1988) calculated that ~0.05 cm of CH<sub>4</sub> would be lost per orbit to escape or chemical destruction (assuming a CH<sub>4</sub> atmosphere with a surface temperature of 43.2 K), and concluded that replenishment is a key element of any volatile cycle.

Second, these papers derived the expressions for how surface pressures and temperatures vary across the surface, including variation with time of day or latitude (in these papers, termed the longitudinal and latitudinal tides). The variation for the latitudinal tide was derived for arbitrary sub-solar latitude in Trafton (1984). These papers found, for example, that 7 cm-Am or more of CH<sub>4</sub> (0.05 kg m<sup>-2</sup>; 0.03 Pa) would maintain global hydrostatic and vapor-pressure equilibrium. This established the central paradigm for Pluto's surface and atmosphere, in which winds transport both mass and energy (through latent heat of sublimation) across the globe, maintaining a surface that is nearly isobaric and isothermal.

1170 Third, these papers predicted that vapor-equilibrium pressures would vary by about a factor of 100 between perihelion and aphelion (a little less variation for CH<sub>4</sub>, a little more for N<sub>2</sub>). They posed a central question that still drives our studies of the volatile cycles on Pluto: when is global uniformity a good approximation, and when is it not? Stern & Trafton (1984) calculated that even CH<sub>4</sub>, the least volatile of the ices they considered, should allow for global uniformity of pressure and volatile ice temperature throughout Pluto's orbit, if the surface were evenly covered by volatile ices. If the surface were unevenly covered by ices, then freeze-out could occur if only a thin veneer of temporary seasonal volatile ices existed at each pole, and sublimed from the summer hemisphere.

1180 Fourth, the aptly titled "Why is Pluto Bright" (Stern et al. 1988) described how the seasonal cycle of volatile sublimation and deposition can drastically alter the surface appearance. Comets and other bodies are darkened as energetic particles and UV photons process ices. CH<sub>4</sub> in particular is converted to larger, darker, less-volatile hydrocarbons. Stern et al. (1988) calculated ~1 cm of clean CH<sub>4</sub> would be deposited each Pluto orbit, freshening or "laundering" the surface, with a possible seasonal phase lag of the refreshing. Thus, they showed that the movement of volatiles can fundamentally alter Pluto's surface.

#### 4.2 Atmosphere confirmed: The first constrained volatile transport models

An atmosphere was definitively discovered by occultation in 1988 (Hubbard et al. 1988, Elliot et al. 1989; Section 2.1.3), yielding refractivity and scale height vs. distance from Pluto's center (not vs. altitude, since the surface radius was still unknown), with the caveat of the unknown influence of hazes on the interpretation of the stellar occultation. After Pluto's N<sub>2</sub> ice was discovered (Owen et al. 1993), refractivity and scale height could be interpreted as pressure and temperature. N<sub>2</sub> had also been detected as the

1190 dominant species in Pluto's sister world, Triton, in 1989. The invaluable 1988 occultation, combined with other breakthrough observations in the 1990's, allowed modeling of Pluto's volatile cycles pinned to concrete observations. Note, however, that the true surface pressure and surface radius were not known until the New Horizons flyby, and the 1988 occultation gave only a single snapshot of Pluto's atmosphere.

Trafton (1990) quantitatively calculated the impact of a two-component atmosphere on Pluto, N<sub>2</sub> and CH<sub>4</sub>. The thermodynamics of that work were discussed in Section 3.4.1. Here, we note the predictions for the time evolution of the volatiles, namely (1) that the escaping atmosphere must be resupplied from the frozen reservoir, with the prediction that the atmospheric bulk composition should resemble that of the reservoir, and (2) for some bulk compositions, the partial pressure of N<sub>2</sub> will not be much different between perihelion and aphelion. Young (1993) modeled an N<sub>2</sub> surface and atmosphere given Pluto mutual-event albedo maps. This work derived the "girdling latitude" approach described in Section 3.2.1 to calculate sublimation wind speeds as a function of latitude. He found that pressures would drop, in one reference case, to a few mPa by 2070, at which time the sublimation winds would have to be supersonic in order to maintain an isobaric surface, likely an untenable situation. His transport model demonstrated the power of albedo feedback, in which bright areas can stay volatile-covered (and bright), even when they are close to the sub-solar latitude. The albedo feedback allows for strong albedo contrasts of bright areas covered with N<sub>2</sub> ice neighboring dark areas of substrate at the same latitude, as seen in mutual event and HST maps. Stansberry and Yelle (1999) describe the effect of N<sub>2</sub> ice emissivity,  $\epsilon$ , on the N<sub>2</sub>-ice temperature. In general, a lower emissivity requires a higher temperature,  $T$ . Because the low-temperature phase of N<sub>2</sub> ice (the  $\alpha$ -phase) has a lower emissivity than the  $\beta$ -phase (Stansberry et al. 1996a; Lellouch et al. 2000), Stansberry and Yelle (1999) argued that Pluto's atmosphere would remain at 35.6 K, the temperature of the  $\alpha$ - $\beta$  phase transition, from a few decades after perihelion through to aphelion. The latent heat difference between the  $\alpha$  and  $\beta$  phases also stabilizes the N<sub>2</sub> frost (Duxbury & Brown 1993).

The most comprehensive and concrete model of this period was by Hansen & Paige (1996; HP96), which built on a similar model applied to Triton (Hansen and Paige 1992), in turn based on a Martian model. For 17 years, HP96 was the only model of Pluto's seasonal behavior that included thermal inertia and mobile N<sub>2</sub> ice. Over 50 cases were run, with thermal inertia ranging from 42 to 2093 tiu, substrate albedo of 0.2 to 0.8, N<sub>2</sub>-ice albedo of 0.2 to 0.8, frost emissivity (constant with phase) of 0.2 to 1.0, and an average global N<sub>2</sub> inventory of 50 to 200 kg m<sup>-2</sup>. This inventory is now known to be very small compared to the N<sub>2</sub> residing in Sputnik Planitia (e.g., Glein & Waite 2018). An important simplification was that only N<sub>2</sub> was included. Seven simulations were plotted in detail (with an eighth showing an example of solstice at perihelion), showing temperatures at selected latitudes, surface pressures, albedo, and frost distribution. Key concepts from the HP96 models were: the importance of thermal inertia, especially for the timing of the formation of winter polar caps; and that the effect of sub-solar latitude can be more important than the change in heliocentric distance (including delaying the atmospheric collapse until after perihelion).

#### 4.3 Signs of change: Modeling the observed volatile cycles

As observations of Pluto's surface spectra improved in quality and frequency, and laboratory data also improved, it became clear that at least three surface components existed and covered large areas on Pluto:

1230 N<sub>2</sub>-rich ice, with dilute amounts of CH<sub>4</sub> and CO; CH<sub>4</sub>-rich ice (indistinguishable in spectra from pure CH<sub>4</sub>); and a third component, presumably tholin (e.g., Grundy & Fink 1996; Grundy & Buie 2002; Grundy et al. 2002; Grundy et al. 2014). Rough composition maps were made by combining HST maps with the changes of spectra vs. sub-solar longitude as Pluto rotated (Grundy & Fink 1996; Lellouch et al. 2000).

1240 Lellouch et al. (2000, 2011, 2016) modeled surface temperatures using these rough composition maps and compared results to observed thermal emission. These thermal models assumed that areas free of volatiles varied their temperatures with latitude and time of day according to thermophysical models that balance insolation, thermal emission, and subsurface conduction. Temperatures of CH<sub>4</sub>-rich ices (or pure CH<sub>4</sub> ices if any) were also varied in the thermal models according to thermophysical models. As shown by Stansberry et al. (1996a), sublimation rates from CH<sub>4</sub>-rich ice at 54 K were large enough that the energy expended for the solid-gaseous phase change (the latent heat of sublimation of CH<sub>4</sub>) slowed down further heating, so the CH<sub>4</sub>-rich ices were capped at 54 K. The N<sub>2</sub>-rich ice was assumed to be isothermal with location and time of day, as required by N<sub>2</sub>'s large latent head of sublimation at Pluto temperatures (Trafton & Stern 1983; Young 2012). Lellouch et al. (2000, 2011, 2016) found a surprisingly small thermal inertia for the diurnal variation, of only ~25 tui, nearly 100 times smaller than the thermal inertia of pure water ice, the likely bedrock. The derived thermal properties applied to the diurnal skin depth (~3 cm). The tholins in these models reached temperatures as high as 63 K, while the CH<sub>4</sub>-rich areas reached their maximum of 54 K, 19 K above the 35 K N<sub>2</sub> temperature (Lellouch et al. 2000).

1250 In 2002, two stellar occultations by Pluto were observed (Elliot et al. 2003; Sicardy et al. 2003), revealing that Pluto's atmospheric pressure had roughly doubled in the 14 years since the previously observed occultation. To many, this was extraordinary (Hubbard 2003), although, as mentioned by both Elliot et al. (2003) and Sicardy et al. (2003), this post-perihelion rise was predicted in many HP96 simulations.

1260 As more stellar occultation observations were observed and analyzed, researchers compared trends with the predictions of HP96 (Fig. 10; Pasacoff et al. 2005; Elliot et al. 2007; Young et al. 2008; Zalucha et al. 2011a,b; Bosh et al. 2015; Gulbis et al. 2015; Dias-Oliveira et al. 2015). Among the runs favored by these authors (Elliot et al. 2007; Young et al. 2008) were HP96 figure 6 & 7, which had small thermal inertia (42 tui) and moderate N<sub>2</sub> inventory (50-100 kg m<sup>-2</sup>). The comparisons were hampered by the uncertainty in Pluto's surface pressure and temperature. By 2006, the trends in pressure could be used to eliminate some of the HP96 runs. The persistent questions—When will Pluto's atmosphere begin its bulk decline? What will the pressure be for the New Horizons flyby?—could not be answered with the small number of cases presented in detail in HP96 and the many unconstrained parameters of the model.

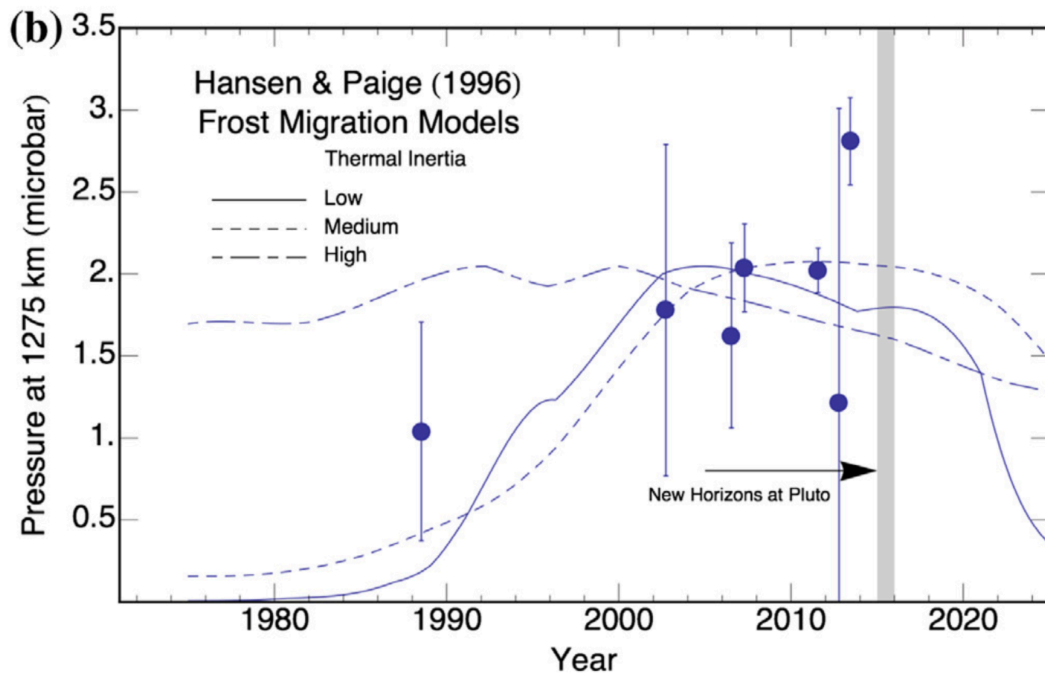


Fig. 10. Measurements of the extent of Pluto's atmosphere, as determined via several stellar occultations between 1988 and 2013 from Bosh et al (2015). The frost migration model predictions of Hansen and Paige (1996) are also included, adjusting the pressure to a radius of 1275 km, to provide context for the differing measurements. The arrival date of the New Horizons spacecraft at Pluto is indicated by the grey vertical bar. (Adapted from Bosh et al. 2015). The pressure at 1275 km radius from the REX radio occultation (Hinson et al 2017) was  $1.948 \pm 0.309 \mu\text{bar}$  ( $0.1948 \pm 0.0309 \text{ Pa}$ ).

1270 Young (2013) developed a new model whose physics was very similar to that of HP96 (mobile  $\text{N}_2$  ices; subsurface conduction; globally isobaric and isothermal  $\text{N}_2$  ice), but with much faster computation time (VT3D; Young 2017). This allowed Young (2013) to cover a grid of thermal inertia from 1 to 3162 tui,  $\text{N}_2$ -ice albedo of 0.2 to 0.8, frost emissivity of 0.55 to 0.8, and an average global  $\text{N}_2$  inventory of 20 to  $640 \text{ kg m}^{-2}$ . Of the 672 cases run, 52 were consistent with the 1988, 2002, and 2006 occultations, and from these, only 19 were also consistent with thermal, visible, and near-IR data. The 52 cases fell into three broad classes. One of these (Exchange with Early Collapse, EEC) had a very small  $\text{N}_2$  inventory, in which the spatially confined northern polar cap was modeled to sublime shortly after equinox. In EEC, the peak occurred before the 2002 occultations, and the predicted pressure plummeted by 2015. The second class (Exchange with Pressure Plateau, EPP) shared many characteristics with Fig 7 from HP96 (one of the favored runs of Elliot et al. 2007 and Bosh et al. 2015): small thermal inertia (10 tui) and small  $\text{N}_2$  inventory ( $8\text{-}16 \text{ kg m}^{-3}$ ), an exchange of  $\text{N}_2$  between northern and southern polar caps, two strong pressure maxima per Pluto orbit, minimum surface pressures below 1 mPa, and a peak pressure near 2002 followed by a very slow decrease. The final class (Permanent Northern Volatiles, PNV) had no equivalent in HP96, and was characterized by: high thermal inertia (typically  $\geq 1000$  tui), large  $\text{N}_2$  inventory (typically  $> 100 \text{ kg m}^{-2}$ ); the presence of  $\text{N}_2$  in the northern hemisphere at every point in Pluto's orbit; one pressure peak per Pluto orbit; minimum surface pressures near 1 Pa, well above the pressure for which the atmosphere

1280

becomes local; and pressures that increase 1988 through 2015. On the basis of a 2013 occultation that showed that the pressure was still increasing (Olkin et al. 2015), the occultation record eliminated the EEC class, and favored the PNV class, which predicted pressures still rising at flyby, with surface pressures near 1.5 to 10 Pa.

Hansen et al. (2015) used the identical model as Hansen & Paige (1996), updated with new observational constraints. As discussed by Hansen et al. (2015), the physics is similar to Young (2013) and Olkin et al. (2015), but the engine was completely independent, and the set and weighting of observational constraints differed. While Young (2013) emphasized the occultation record, and the increase of occultation pressures 1988-2013, Hansen et al. (2015) emphasized the albedo record (Section 2.1.1), especially (1) that HST did not detect bright zonal bands, disallowing models where N<sub>2</sub> ice persisted at a given latitude over a Pluto orbit; (2) that a southern polar cap was detected before and during equinox; (3) that the northern cap was larger than the southern cap at equinox; and (4) that the infrared spectral evidence pointed toward a shrinking northern polar cap, 2001-2012. They found it very difficult to find combinations of parameters that had pressures rising past 2013 and a south polar cap in 1988. Their favored model (run 22) had a thermal inertia of 42 tiu and an N<sub>2</sub> inventory of 50 kg m<sup>-2</sup>, both higher than Fig 7 of HP96, but much lower than the PNV runs of Young (2013). Similar in character to the HP96 models and the Young (2013) EPP models, Hansen et al. (2015) runs 22 and 48 had two pressure peaks per Pluto orbit, a complete exchange between summer and winter poles, and pressure minima near the local/global cutoff. Hansen et al. (2015) predicted, for the time of the flyby, a large summer polar cap extending to low-to-mid northern latitudes that would be in the process of subliming, and pressures between 0.14 and 3.2 Pa that were falling slowly.

Both the Hansen (2015) and Young (2013) papers had trouble reconciling the occultation record with the evidence for a bright southern cap prior to and at equinox. Young (2013) did not try to reproduce that cap, and found high-thermal-inertia solutions with pressures rising past 2015, and northern N<sub>2</sub> ice deposits that persisted through a Pluto year. Hansen et al. (2015) required the southern cap, leading to lower thermal inertia solutions with pressures dropping slowly in 2015, pressures at flyby near 2.4 Pa, and a large but mobile northern cap. Neither model anticipated the large reservoir of N<sub>2</sub> in Sputnik Planitia. Both models highlight one of the persistent questions: the amount and role of volatiles in Pluto's southern latitudes.

Several factors between the 2002 occultations and the 2015 flyby inspired new studies of Pluto's atmospheric dynamics. The anticipated arrival of spacecraft sparked interest. Several occultations showed the signature of wave-like temperature fluctuations. The seasonal models of Young (2013) and Hansen et al. (2015) could provide GCMs with initial conditions of volatile distributions and surface or subsurface temperatures. And some simplified dynamical models could shed light on seasonal effects. Much of this is treated in the Chapter by Forget et al., and so we focus here on where dynamics touch on volatile cycles. In brief, Toigo et al. (2010) and French et al. (2015) calculated the thermal tides on Pluto, quantitatively predicting vertical winds at the surface due to the diurnal cycle of sublimation and condensation. Two GCMs were developed pre-encounter (PlutoWRF; Toigo et al. 2015; LMD, Vangvichith 2013), which also ran their own predictions for seasonal volatile cycles. Vangvichith (2013) showed the interaction between the N<sub>2</sub> and CH<sub>4</sub> cycles. Toigo et al. (2015) showed double-peaked pressures over a Pluto year for lower thermal inertia, and single-peaked for higher, and suggested that the mobile ices in the PNV class

1330

of Young (2013) would become static if the model were run for more Pluto years. As with Young (2013) and Hansen et al. (2015), the PlutoWRF and LMD models pre-encounter could not anticipate the N<sub>2</sub> reservoir of Sputnik Planitia (although some of their simulations used the joint spectra/HST maps that include an equatorial N<sub>2</sub> source near 180° longitude). The themes of southern N<sub>2</sub>, perennial vs. seasonally mobile ices, diurnal tides, minimum pressure, and entwined N<sub>2</sub>-CH<sub>4</sub> cycles all proved to be as important after the New Horizons flyby as they were before.

#### 4.4 Pluto Volatiles after New Horizons

In Table 3, we list those post-encounter models which calculated sublimation/condensation rates or changes in volatile distributions or surface pressures. They are organized roughly by research group, to more clearly show the hierarchy of models. We present these in this section in roughly chronological order, emphasizing their assumptions, and their broad conclusions, particularly how they alter our understanding of the processes most affecting Pluto's interacting surface and atmosphere. A consolidated summary of the model results sorted by the different timescales is given in Section 5.

1340

Table 3. Post-encounter models of volatile cycles and trends

Model	Diurnal	Seasonal	Milankovitch	Topography	Subsurface Conduction	Mobile N <sub>2</sub>	CH <sub>4</sub>	Resolution (km)	Tuned to occultations
Moore et al. (2016)	Yes	Yes	Yes	No	Yes	Yes	No	100	Yes
Earle et al. (2017)	No	Yes	Yes	No	No	No	Yes <sup>d</sup>	20	No
Stern et al. (2017)	No	Yes	Yes	No	No	No	Yes <sup>d</sup>	150	No
Earle et al. (2018a)	No	Yes	Yes	No	No	Yes	Yes <sup>d</sup>	10	No
Young et al. (2015)	No	Yes	No	No	Yes	Yes	No	208	Yes
Lewis et al. (2019)	No	No <sup>a</sup>	No	Yes	No	No	No	1	Yes
Johnson et al. (2019)	No	Yes	Yes	No	Yes	No	No	1	Yes
Bertrand & Forget (2016)	Yes	Yes	No	Yes	Yes	Yes <sup>c</sup>	Yes	190	Yes
Forget et al. (2017)	Yes	No <sup>b</sup>	No	Yes	Yes	Yes <sup>c</sup>	Yes	190	Yes
Bertrand et al. (2018)	Yes	Yes	Yes	Yes	Yes	Yes	No	63&190	No
Bertrand et al. (2019)	Yes	Yes	Yes	Yes	Yes	Yes	Yes	190	No
Meza et al. (2019)	Yes	Yes	No	Yes	Yes	Yes <sup>c</sup>	Yes <sup>e</sup>	95	Yes
Bertrand et al. (2020a)	Yes	Yes	No	Yes	Yes	Yes	Yes	63&190	Yes

<sup>a</sup> Snapshot of mass fluxes at flyby. <sup>b</sup> Calculated on timescale of several earth decades. <sup>c</sup> N<sub>2</sub> allowed to be mobile, but evolves to a static configuration. <sup>d</sup> N<sub>2</sub> and CH<sub>4</sub> modeled independently. <sup>e</sup> CH<sub>4</sub> is implemented, but does not interact with the N<sub>2</sub> cycle in practice.

#### 4.4.1 First models of Sputnik Planitia

The discovery of Sputnik Planitia changed everything. An enormous reservoir of N<sub>2</sub>-rich ice in the diurnal zone affects the volatile and climate cycles on all timescales, from non-cyclic, to Milankovitch cycles, Pluto's seasonal cycle, or Pluto's day.

1350 In pre-encounter models (Young, 2013; Hansen et al. 2015), surface pressures plummeted when the last of the N<sub>2</sub> ice left the summer hemisphere, because the globally averaged insolation onto the N<sub>2</sub> ice dropped to nearly zero. But on the real Pluto, the N<sub>2</sub>-rich Sputnik Planitia straddles the equator, and so there is some insolation onto N<sub>2</sub>-rich ices every Pluto day. Early post-flyby models that imposed an N<sub>2</sub>-ice reservoir at Sputnik Planitia (Young et al. 2015) showed that adding this reservoir delayed the sublimation from the summer hemisphere and raised the minimum pressure for a sample case with low seasonal thermal inertia (Young 2013/EPP14, with 3 tui), but had little effect on the volatile distribution and pressures for a case with high thermal inertia (Young 2013/PNV23, with 1000 tui).

After the New Horizons flyby, researchers soon recognized that Sputnik Planitia was a natural place for N<sub>2</sub> to accumulate, both because of its low elevation (Stern et al. 2015; Moore et al. 2016; cf. Section 3.2.3) and its lower insolation, averaged over a Pluto year (Hamilton et al. 2016; cf. Section 3.1.2).

1360 Two important early post-flyby models (Forget et al. 2017; Bertrand & Forget 2016, hereafter BF16) included an idealized Sputnik Planitia as a circular depression, 3.8-km deep and 1000 km wide. These papers arose from Laboratoire de Météorologie Dynamique (LMD), which developed two related volatile transport models: a full Global Climate Model (GCM; Forget et al. 2017; Chapter by Forget et al.); and a reduced version that used a simple global mixing function for N<sub>2</sub>, CH<sub>4</sub>, and CO in place of 3D atmospheric transport and dynamics (BF16). These two models are complementary. The reduced model ran much more quickly, and was therefore suitable for simulations on the timescale of Pluto's 248-year orbit to tens of thousands of years. The reduced model was used to initialize the surface ice distribution and sub-surface temperatures for the GCM. The GCM calculated the transport between surface and atmosphere, and within the atmosphere from one location to another, on the timescale of Pluto's day to several Earth decades.  
1370 Tests done with the GCM determined the timescales for atmospheric transport of CH<sub>4</sub> (10<sup>7</sup> s, i.e., about 4 Earth months) and N<sub>2</sub> (1 s, instantaneous mixing) used in the reduced model.

The main result from Forget et al. (2017) for the purpose of this chapter was that the cold atmospheric layer seen the lowest kilometers above Sputnik Planitia was due, in part, to the daytime sublimation of N<sub>2</sub> over Sputnik. The winds and atmospheric temperature results from the GCM are covered in the Chapter by Forget et al.

The volatiles on BF16 were initialized with 50 kg m<sup>-2</sup> of each of N<sub>2</sub> and CH<sub>4</sub> distributed uniformly over Pluto. The seasonal model of BF16 captured many of the important points of Pluto's surface volatiles: a migration of N<sub>2</sub> into the Sputnik Planitia basin after several thousands of years; the role of Sputnik Planitia as the dominant N<sub>2</sub> reservoir, the presence of CH<sub>4</sub>-rich ice at higher latitudes, and volatile-free areas near the equator. The model predicted seasonal variation in the CH<sub>4</sub> distribution, with the northern CH<sub>4</sub> cap disappearing by 2030. The modeled CH<sub>4</sub> variation, and, perhaps, the N<sub>2</sub> confinement was a consequence of the model's small volatile inventory.  
1380

BF16 were also able to find combinations of thermal inertia and N<sub>2</sub>-ice albedo that reproduced the surface pressures seen by New Horizons and the occultation record. These models favored high thermal

inertias for roughly the upper 40 m of the subsurface; the reference model was 800 tui, and the BF16 model ruled out thermal inertias lower than 500 tui.

#### 4.4.2 Geological considerations

Pluto's geology revealed evidence of ongoing, recent, and past volatile cycles (See Chapter by Moore & Howard). These include: cryovolcanism (Wright and Picard Mons); the pits within Sputnik Planitia; the albedo variations within Sputnik Planitia; possible wind streaks and dunes in western Sputnik Planitia; high-altitude methane deposits; N<sub>2</sub> glaciers flowing into eastern Sputnik Planitia from the neighboring highlands; km-wide ridges of CH<sub>4</sub>-rich ice in the Bladed Terrain; the smooth Alcyonia Lacus; albedo contrast in the equatorial regions (maculae vs. Tombaugh Regio); evidence for thick, eroded CH<sub>4</sub>-rich mantles in Pioneer and Hayabusa Terrae northeast of Sputnik Planitia; the eroded scarps of Peri Planitia; and erosional valleys north, northeast, and southwest of Sputnik Planitia. The rich geology at Pluto proved that, once again, our imaginations were less wide-ranging than reality. Pre-encounter, modelers considered volatile transport involving sublimation/condensation and atmospheric winds. Because of New Horizons, we now know that Pluto's volatile transport processes additionally include: large-scale convection within Sputnik Planitia; ancient and present-day glacial flow; liquification of N<sub>2</sub> at the base of ancient or current deep N<sub>2</sub> ice, and possible ancient cryovolcanism.

Some of the geologic features observed by New Horizons motivated the possibility that Pluto's pressure may have been much higher in the past (Stern et al. 2017). The importance of the Milankovitch cycles was re-enforced by Pluto's latitudinal variation in albedo (Binzel et al. 2017), which raised the possibility that obliquity and the solar longitude at perihelion,  $L_{S,peri}$ , could be important for Pluto's volatile cycles. This was investigated by Earle et al. (2017), who defined polar caps extending to  $\pm 45^\circ$ ,  $\pm 60^\circ$ , or  $\pm 75^\circ$ , and by Stern et al. (2017), who included a rectangular Sputnik Planitia  $45^\circ$  wide from  $45^\circ$  N to  $30^\circ$  S. Given emissivity of 0.6 or 0.9, and albedo from 0.1 to 0.6, these models calculated pressures vs. time for three epochs: the current epoch; extreme northern summer 0.9 My ago when perihelion coincided with northern summer solstice; and extreme southern summer 2.35 My ago when perihelion coincided with southern summer solstice. They found that the Milankovitch cycles can have a significant effect, which has been borne out by subsequent modelers (e.g., Bertrand et al. 2018, 2019).

The relationship between geology and the Milankovitch cycles (Binzel et al. 2017) was explored quantitatively by Earle et al. (2018a) who calculated the stability of N<sub>2</sub> and CH<sub>4</sub> ices. N<sub>2</sub> and CH<sub>4</sub> were modeled independently, treating each in turn as the dominant volatile. For the N<sub>2</sub>-cycle, they found two very different styles of variation, depending on albedo. For dark N<sub>2</sub> ice ( $A < 0.3$ ), the equator lost its N<sub>2</sub>, and the seasonal cycle was an exchange of N<sub>2</sub> between northern and southern polar caps. For bright N<sub>2</sub> ice ( $A > 0.6$ ), there was still some exchange of the polar caps, since the deposition rate onto a latitude in arctic night is independent of albedo. However, the main result for bright N<sub>2</sub> ice was that the N<sub>2</sub> was trapped near the latitudes where the annual insolation was least. Thus, for high obliquity ( $103^\circ$ , 0.9 Myr ago), when the insolation minimum was at the equator, the N<sub>2</sub>-ice distribution was sharply peaked around the equator, mainly confined to  $\pm 30^\circ$ . For low obliquity ( $126^\circ$ , 2.35 Myr ago), when the insolation minimum was at  $\pm 30^\circ$ , the N<sub>2</sub>-ice distribution was very broad, with maxima near  $\pm 45^\circ$ . Comparing the low and high

albedo cases, Earle et al. (2018a) concluded that, qualitatively, N<sub>2</sub> ice was subject to runaway albedo at low- to mid-latitudes.

The Bladed Terrain may be a sublimation effect, in analogy with terrestrial penitentes (Moores et al. 2016; Moore et al. 2018; see Chapter by Moore and Howard). This motivated the climate calculations in Moores et al. (2016), using the PlutoWRF GCM engine described in Toigo et al. (2015). Moores et al. (2016) incorporated some new model simulations based on early Pluto results, including some latitudinal information but no topography. Their models predicted not just pressure vs. time at different epochs of Pluto's Milankovitch cycles, but also parameters related to the growth of penitentes. The Moores et al. (2016) result that the pressure is a maximum near equinox may be related to early Pluto results that showed the 2015 surface pressure and the latitudinal distribution of surface ices (Stern et al. 2015; Moore et al. 2016; Gladstone et al. 2016), but did not include topography, such as a bowl-shaped depression for Sputnik Planitia (Toigo, personal communication). However, the Moores et al. (2016) models also show the importance of the Milankovitch cycles for Pluto climate studies, and the geologic expression of those cycles.

#### 4.4.3 N<sub>2</sub> cycles on seasonal and Milankovitch timescales

Higher resolution New Horizons data products followed, in 2017 and 2018, including the near-surface pressures vs. altitude, and high-resolution geologic, topographic, color, and composition surface maps (See Section 2.2).

Using these products, Bertrand et al. (2018; henceforth B18) modeled the N<sub>2</sub> cycle on Pluto with a model based on BF16, including thermal conduction into the substrate. Additions to the BF16 model included the Milankovitch cycles, topographic information, glacial flow, a larger N<sub>2</sub> inventory, and higher spatial resolution for some runs focused on Sputnik Planitia. Simplifications include averaging insolation over diurnal cycle (which should have minimal impact; Young 2012), and consideration of only a small set of seasonal thermal inertias (generally 800 tui, with a few cases at 400 or 1200 tui) and albedo (generally 0.7, with a few cases at 0.4). B18 included a much larger N<sub>2</sub> inventory than BF16, which takes much longer to equilibrate. Thus, B18 considered two related problems: a study of the sublimation patterns within Sputnik Planitia, run at higher spatial resolution, with an initial distribution of N<sub>2</sub> confined to the Sputnik Planitia basin; and a study of the stability of N<sub>2</sub> outside Sputnik Planitia, with a variety of initial N<sub>2</sub> distributions. The experiments of B18 on N<sub>2</sub> stability included N<sub>2</sub> inventories with global averages of 200 m, 500 m, or 1000 m ( $2 \times 10^5$ ,  $5 \times 10^5$ , or  $10^6$  kg m<sup>-2</sup>), consistent with the expected volume of N<sub>2</sub> ice within Sputnik Planitia (Glein and Waite 2018), with various initial distributions of N<sub>2</sub> that were global, confined to low latitudes, or confined to high latitudes.

Lewis et al. (2020) calculated energy balance and mass fluxes using high-resolution maps of bolometric albedo (Buratti et al. 2017) and N<sub>2</sub> presence (Schmitt, personal communication), based in part on the CH<sub>4</sub> spectral shifts, and extrapolating ice coverage to unmapped areas. By matching the observed 2015 surface pressure, they derived N<sub>2</sub> emissivity of 0.47-0.78, with the exact value dependent on assumptions of the unmapped hemisphere (the non-encounter longitudes, and the southern latitudes). From this, they produced a map of the current sublimation and condensation rates. Like B18, they found a trend of north-to-south transport within Sputnik Planitia, similar to B18. However, the maps of Lewis et al. (2020) also

included N<sub>2</sub> observed outside Sputnik Planitia. They found high sublimation rates of 3 g cm<sup>-2</sup> yr<sup>-1</sup> (0.52 mm (Pluto day)<sup>-1</sup>) for N<sub>2</sub> at mid latitudes.

Johnson et al. (2020) used similar maps as Lewis et al. (2020), and calculated pressure vs. time over a Pluto year given four assumptions of a static N<sub>2</sub> ice distribution. This work made a systematic search over albedo ( $A$ ), emissivity ( $\epsilon$ ), and thermal inertia ( $\Gamma$ ), and identified those triplets of  $A$ ,  $\epsilon$ , and  $\Gamma$  that satisfied the New Horizons pressure constraints (surface pressure 1.15 Pa) and 1988 pressure constraints ( $3.14 > P_{2015}/P_{1988} > 1.82$ ). The motivation for this work was to study the minimum pressures reached over Milankovitch timescales, to see if haze production would be disrupted. As described in Section 5.2 (Milankovitch cycles) and 5.3 (Seasonal cycles), these models found that the presence of Sputnik Planitia tended to maintain a minimum pressure that was high enough to allow haze production.

While the LMD models in Meza et al. (2019) formally include CH<sub>4</sub> ice, we treat them in this section. The three simulations with rising pressures 1988-2015 in Meza et al. (2019) had perennial N<sub>2</sub> in Sputnik Planitia and in the depressions in the northern hemisphere, with low-albedo CH<sub>4</sub> ice ( $A_{CH_4} = 0.5$ ). Because the low-albedo CH<sub>4</sub> remained warm, there was very little seasonal deposition of N<sub>2</sub> ice. In the southern hemisphere, the CH<sub>4</sub> deposits were very thin and the albedo remained low. Thus, the N<sub>2</sub> ice distribution in Meza et al. (2019) was essentially static, and directly comparable to the runs of Johnson et al. (2020).

#### 4.4.4 N<sub>2</sub> - CH<sub>4</sub> cycles on seasonal and Milankovitch timescales

Bertrand et al. (2019, henceforth B19) addressed Pluto's climate with both the N<sub>2</sub> and CH<sub>4</sub> volatile cycles. Surface units are treated as either volatile-free, N<sub>2</sub>-rich with 0.5% CH<sub>4</sub>, or pure CH<sub>4</sub>. In reality, the CH<sub>4</sub> mixing ratio within N<sub>2</sub>-rich ice was observed to vary with location on Pluto (Protopapa et al. 2017), which is not tracked by this model. As described in Section 3.4.1, this simplification should have little effect on the calculated N<sub>2</sub> or CH<sub>4</sub> mass fluxes over N<sub>2</sub>-rich areas or the CH<sub>4</sub> mass fluxes over CH<sub>4</sub>-rich areas. However, N<sub>2</sub> fluxes over CH<sub>4</sub>-rich areas is more problematic. For condensation, the model simply assumes that a cold CH<sub>4</sub>-rich area can become a N<sub>2</sub> condensation site when the temperature is low enough, at which point the area is modeled as N<sub>2</sub>-rich. N<sub>2</sub> sublimation from CH<sub>4</sub>-rich areas is not modeled. B19 explored the complex ways in which modeled changes in surface albedos, emissivities and thermal inertias affected volatile transport, surface distributions, and atmospheric pressure and composition. B19 presented a variety of runs to show the range of modeled outcomes; in Meza et al. (2019), runs were fine-tuned (e.g., in N<sub>2</sub> albedo) to match the occultation record.

This work demonstrates the challenge of how to explain the observed widespread presence of CH<sub>4</sub> outside of Sputnik Planitia, as models such as B19 predict that CH<sub>4</sub> would accumulate in Sputnik Planitia on the timescale of several Myr if CH<sub>4</sub> were allowed to condense into Sputnik Planitia. The mechanism for preventing all the CH<sub>4</sub> from accumulating into Sputnik Planitia is unknown, but Bertrand et al. (2019) speculate that the mixing state of the upper layers of the volatiles may be responsible (Section 3.4). It may also be related to the cycle of net N<sub>2</sub> into or out of Sputnik Planitia over Milankovitch cycles (Bertrand et al. 2018, 2019).

One initial state in B19 began with N<sub>2</sub> ice filling Sputnik Planitia basin, and with a 4-meter thick layer of CH<sub>4</sub> ice covering the entire globe. This was particularly applicable to long-term trends, including over a timespan of several Milankovitch cycles. An alternate initial state also began with N<sub>2</sub> in Sputnik Planitia,

but included an infinite reservoir of CH<sub>4</sub> roughly at the latitudes of the Bladed Terrains (excluding Cthulhu). This initial state represented the Bladed Terrains as a perennial CH<sub>4</sub> source. These runs allowed different CH<sub>4</sub> albedos for equatorial CH<sub>4</sub> vs. CH<sub>4</sub> at mid-latitudes or the poles, and are particularly applicable to the current Pluto season or Milankovitch cycle. The results of these model runs are described in Section 5.2 (Milankovitch cycles) and 5.3 (Seasonal cycles).

## 5. Volatile Transport at Short and Long Timescales

In this section, we summarize the results of the preceding models on several timescales (Table 4). We avoid the term “secular,” which has been applied both to evolutionary changes over 4 billion years, and observed changes on decadal timescales. Sputnik Planitia dominates much of the movement of volatiles at all timescales, as described in Section 4.4, as the surface pressure is heavily influenced by the distribution of N<sub>2</sub>. The N<sub>2</sub> cycle, in turn, interacts with the CH<sub>4</sub> cycle.

The various times scales are intertwined as well. We choose to present the timescales in the order listed in Table 4, because each timescale provides the context for the next-shorter timescale. A non-cyclical process filled in Sputnik Planitia, the presence of which affects all of the subsequent cycles.

Where possible, we emphasize observational constraints. Complementary perspectives on volatile processes can be found in other chapters: the Chapter by Forget et al. covers many issues relating to the diurnal cycles, and the Chapters by White et al. and Moore and Howard cover aspects of the volatile activity on astronomical timescales.

Table 4. Timescales for volatile transport

Timescale	Cycle Duration	Examples
Non-cyclical (aka evolutionary)	10 Myr to 4.5 Gyr duration, not cyclic.	Infilling of Sputnik Planitia; atmospheric escape; formation of Bladed Terrain
Milankovitch cycles,(aka orbit/pole cycles, mega-seasons)	2.8 Myr obliquity cycle; 3.7 Myr eccentricity and libration of argument of perihelion	Variation of pressure extreme; Sputnik Planitia shorelines & erosion; Northern and southern boundaries of Bladed Terrain; glacial flow.
Seasonal (aka orbital, annual)	248 Earth years	N-S flow within Spunik Planitia; Pressure changes; transport of seasonal volatile ice; albedo/color
Diurnal (aka rotational, daily)	6.4 Earth days	Global atmosphere; Cold troposphere above Sputnik Planitia

### 5.1 Non-cyclical timescales

A singular event in Pluto’s volatile history is the infilling of Sputnik Planitia. If Sputnik formed as an impact basin (Stern et al. 2015; Moore et al. 2016) in its current location, then the combined effects of

enhanced condensation in a topographic low and insolation minimum near the equator would cause Sputnik Planitia to fill in about 10 Myr (Fig. 11; Bertrand & Forget 2016; Bertrand et al. 2018), or a rate of  $\sim 1 \text{ km Myr}^{-1}$  ( $10^6 \text{ kg m}^{-2} \text{ Myr}^{-1}$ ). Some modelers find that the insolation effect might be enough, without an impact basin (Hamilton et al. 2016). Some model runs (Bertrand et al., 2018) found that  $\text{N}_2$  could be temporarily stable in low latitudes outside of Sputnik Planitia for tens of Myr, especially for large  $\text{N}_2$  inventories, before finally condensing into Sputnik Planitia. Earle et al. (2018a) found that both dark areas free of  $\text{N}_2$ -free (such as Cthulhu), and bright,  $\text{N}_2$ -rich areas (such as Tombaugh Regio) were stable near the equator on Myr timescales. Considering  $\text{N}_2$  alone, B18 found  $\text{N}_2$  was never stable at high latitudes, but  $\text{CH}_4$  complicates this picture (B19).

1530

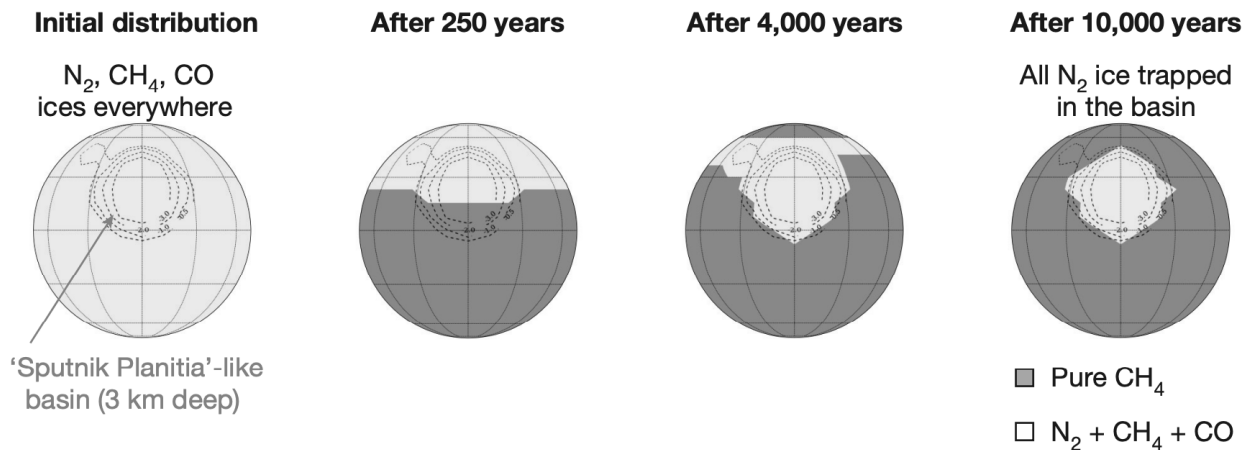


Fig. 11. Surface maps from the reference simulation of BF16 with thermal inertia = 800 tiu. The simulation began with all ices uniformly distributed.

$\text{CH}_4$  is much less mobile than  $\text{N}_2$ .  $\text{CH}_4$  also preferentially condenses near the latitudes of long-term average minimum insolation, but it does it slowly (Bertrand et al. 2019), at a rate near  $1 \text{ m Myr}^{-1}$  ( $1 \times 10^3 \text{ kg m}^{-2} \text{ Myr}^{-1}$ ). The model of Bertrand & Forget (2016) had a mm-veneer of  $\text{CH}_4$  ice, and simulated a pole-to-pole seasonal exchange. Initializing Pluto with  $\text{N}_2$  in Sputnik Planitia and a globally uniform distribution of 4 m of  $\text{CH}_4$  with a uniform  $\text{CH}_4$  albedo (Bertrand et al. 2019; their Section 3), the  $\text{CH}_4$  is modeled to slowly migrate to the equator, mainly by loss of  $\text{CH}_4$  from the poles (Fig. 12). If the modeled  $\text{CH}_4$  ice is more mobile (darker  $\text{CH}_4$  albedo, or lower substrate thermal inertia), then the equatorial deposits cover a wider latitude range.

1540

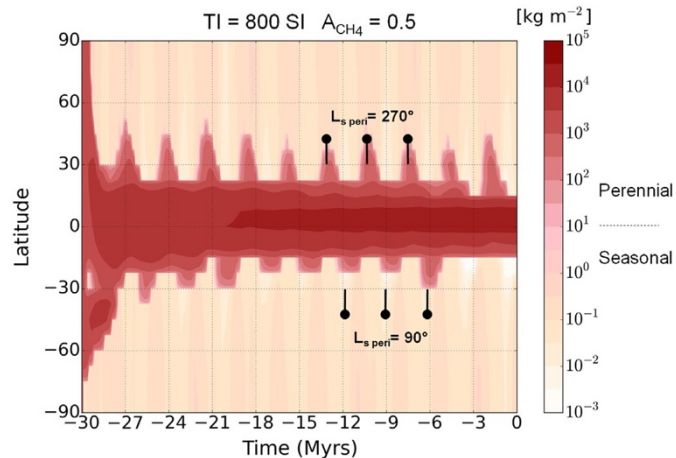


Fig 12. Example run for an initially global  $\text{CH}_4$  with  $A_{\text{CH}_4} = 0.5$ , showing the zonal annual mean of  $\text{CH}_4$  outside of Sputnik Planitia. Figure from Bertrand et al. 2019 (B19).

The modeled  $\text{CH}_4$  deposits tended to occur slightly north of the equator, at the latitudes of the Bladed Terrain on the encounter hemisphere. At these slow rates, it would have had to take millions of years to build up the Bladed Terrains to the observed depths of hundreds of meters crest to base (Moore et al. 2018), and longer if the mass of the Bladed Terrain Deposits were km deep. Even though  $\text{CH}_4$  is less mobile than  $\text{N}_2$ , why  $\text{CH}_4$  is not also mainly sequestered within Sputnik Planitia remains a puzzle. Simulations over tens of Myr (Bertrand et al. 2019) revealed two potential reservoirs of  $\text{CH}_4$ : either at low latitudes similar to the Bladed Terrain; or at mid-latitudes, similar to the  $\text{CH}_4$ -rich mantled terrains. However, only one reservoir or the other is stable at any given time. For current epoch, the models of Bertrand et al. (2019) suggested that the low-latitude  $\text{CH}_4$  is subliming, carving out the blades of the Bladed Terrain and feeding the mid-latitude  $\text{CH}_4$ . At rates of  $1 \text{ m Myr}^{-1}$ , if there is a cyclic exchange between low and mid-latitude  $\text{CH}_4$ , it must occur over hundreds of Myr. The mechanism for such a cycle is unclear.

Prior to the New Horizons encounter, the escape of volatiles over the age of the solar system was expected to be a major component in shaping the landscape of Pluto. However, the escape rate of  $\text{N}_2$  ( $\sim 5 \times 10^{22} \text{ N}_2 \text{ s}^{-1}$ ; Young et al. 2018) was found from New Horizons measurements to be  $\sim 3000$  times lower than expected pre-encounter (Gladstone et al. 2017). Further, the major escaping species was found to be  $\text{CH}_4$  ( $\sim 6 \times 10^{25} \text{ CH}_4 \text{ s}^{-1}$ ; Young et al. 2018), which was also escaping too slowly to sculpt the landscape (see chapter by Strobel). Less atmospheric  $\text{N}_2$  or  $\text{CH}_4$  is lost due to escape than is lost by incorporation into precipitating hydrocarbons and nitriles (Krasnopolsky 2020).

## 5.2 Milankovitch cycles

Since the flyby, there has been a new appreciation for the impact of the Milankovitch cycles, particularly the 2.8-Myr obliquity cycle, and the variation of the solar longitude at perihelion (varying by  $360^\circ$  over 2.8 Myr, with a  $24^\circ$  oscillation superimposed that varies with the 3.95-Myr eccentricity cycle). The location of the equatorial  $\text{CH}_4$  deposits vary with the Milankovitch cycle too. For example, some models of Bertrand et al. (2019) show a steady accumulation of Bladed Terrains, with the boundary of the

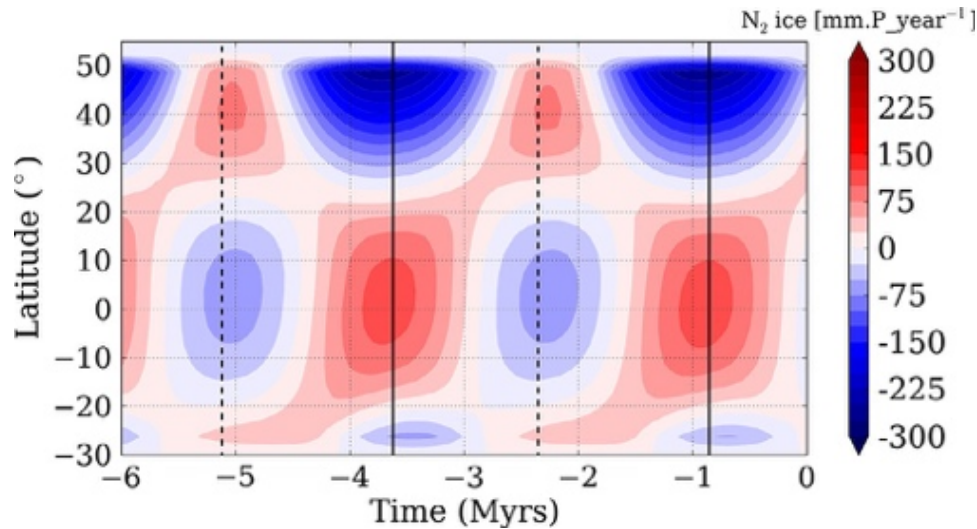
terrains varying such that it favors the perihelion winter hemisphere (e.g., equator and low southern latitudes when  $L_{S,peri} = 90^\circ$ ; Fig. 12).

Even without any variation in the surface distribution of volatile ices, the changing insolation would affect atmospheric pressure and winds (Moore et al. 2016; Earle et al. 2017; Meza et al. 2019; Johnson et al. 2020). In particular, the annual pressure minima and maxima vary with obliquity.

1580 In models based on the observed  $N_2$ -ice distribution, Johnson et al. (2020) found the minimum seasonal pressures varied between 50 and 300 mPa, with lower minimum pressures ( $<6$  mPa) possible for some  $N_2$  albedos and distributions. B18 found minima of  $\sim 10$  mPa for nominal  $N_2$  albedo  $A_{N_2} = 0.7$ , and higher minimum pressures of  $\sim 1$  Pa for darker  $A_{N_2} = 0.4$ . This implies that, for the great majority of parameter space, Pluto's atmosphere remains global throughout its entire year over multiple obliquity cycles, and sublimation winds are able to keep  $N_2$  ice temperatures nearly isothermal (cf Section 3.2.1).

1590 Earle et al. (2017) and Stern et al. (2017) concluded that maximum pressures could be of order kPa, much higher than the current pressure of 1.1 Pa, perhaps tied to lines of geologic evidence for periods of high surface pressure. However, their results required a mechanism for confining  $N_2$  to Pluto's poles, and no such confining mechanism is identified for Pluto's current Milankovitch cycle (that is, the last 2.8 My). In contrast, B18 found maximum seasonal pressures of  $\sim 10$  Pa for  $A_{N_2} = 0.7$ , and only 50 Pa even for dark  $N_2$  with  $A_{N_2} = 0.4$ . B18 argued that periods of high surface pressure (Stern et al. 2017) were not recent. Alternatives include higher pressure very early in Pluto's evolution, or ancient flows at the bottom of deep glaciers (B18).

1600 Regardless of how Sputnik Planitia was established, it is now a deep reservoir of  $N_2$  straddling Pluto's equator, experiencing insolation changes. The difference in insolation at the northern and southern extremes of Sputnik Planitia vs. its center causes differential sublimation or condensation; even with glacial flow, the model of B18 predicts variation of the  $N_2$  topography of up to 300 m over Milankovitch cycles (Fig. 13; B18), but it could be less if a km-deep bedrock is assumed near the edges of the ice sheet. Averaged over 1.3 to 0.1 Myr ago, B18 predicted that the center of Sputnik Planitia accumulated  $N_2$ , so that that the ice sheet currently covers a minimum area, with depressions at the northern and southern boundaries. The modeled rise and fall of the edges of Sputnik Planitia, especially the northern boundary, may have contributed to erosion of the water-ice border, particularly near the enigmatic Al-Idrisi region. Averaged over a 2.8-Myr obliquity cycle, B18 found that Sputnik Planitia lost 1 km from its northern edge by sublimation, and 0.15 km from its southern edge, with net transport to the center. These changes in ice thickness are balanced by glacial flow. By some models, the deep pits within Sputnik Planitia probably formed on timescales of 100,000 yr (Buhler and Ingersoll 2018)—longer than Pluto's orbit, but short on Milankovitch timescales (but see the Chapter by Moore and Howard for suggested formation timescales comparable to or longer than the Milankovitch cycle). A snapshot of the annually averaged insolation suggests a correlation with pit formation (a sublimation process, see Chapter by Moore and Howard), so the latitudes of pit formation may well vary on Milankovitch timescales.



1610 Fig. 13 Evolution of the annual mean condensation-sublimation rate of  $N_2$  ice with time (mm per Pluto year; red is condensation), assuming that the glacier remains flat (same as Fig. 8. The vertical solid and dashed lines correspond to the periods of high ( $104^\circ$ ) and low ( $127^\circ$ ) obliquity, respectively. Figure from Bertrand et al. 2018 (B18).

Outside of Sputnik Planitia,  $N_2$  can be stable over a season at the equator or at mid-latitudes, but the stability varies with obliquity (B19, their Figure 4).

### 5.3 Seasonal cycles

1620 Pluto's present obliquity ( $119.6^\circ$ ) and orbital eccentricity results in pronounced seasonal variations in illumination. These drive significant changes in sublimation and condensation rates of the volatile ices over the course of a Pluto year, and thus affect the atmospheric pressure and composition, and the volatile surface ices. Volatile transport models highlight the sensitivity of the volatile cycles to several unconstrained parameters, such as the initial ice distribution, bolometric Bond albedo, emissivity, and the seasonal thermal inertia of the subsurface (Hansen and Paige 1996; Young 2013; Stansberry and Yelle 1999). An important observational constraint for these free parameters came from the large number of stellar occultations acquired between 1988 and 2016, showing a threefold increase in surface pressure during this period (see Section 2.1.3, and Olkin et al. 2015; Bosh et al. 2015; Meza et al. 2019). In July 2015, New Horizons observations directly measured the surface pressure and volatile distribution, which brought stronger constraints for the free parameters in volatile transport models. The deep permanent reservoirs of volatile ice in Sputnik Planitia fundamentally changed our understanding about the motion of volatiles on Pluto.

1630 New Horizons flew by Pluto during northern spring. Models predicted  $N_2$  transport within Sputnik Planitia from the north ( $15^\circ N$  to  $50^\circ N$ ) to the south ( $30^\circ S$  to  $15^\circ N$ ) in 2015, and more generally a north-to-south transport between equinoxes in 1988 and 2109 (Fig. 14; B18, their Fig 7 & 8), and south-to-north transport during the opposite seasons (the preceding 124 years). Protopapa et al. (2017) found that the abundance and grain size of the  $N_2$ -rich ice increased from the northwest to southeast within Sputnik Planitia, and Schmitt et al. (2017) found a similar trend with the  $N_2$  band depth at  $2.15 \mu m$ . B18 derived that over the last 30 years, a few cm of  $N_2$ -rich ice has moved north-to-south, which is comparable to the

derived grain size of CH<sub>4</sub> in northwest Sputnik Planitia (Protopapa et al. 2017), and may indicate the formation of CH<sub>4</sub>-rich ice during sublimation (Stansberry et al. 1996b; Tan & Kargel 2018). It is less clear whether the deposition of a few cm of N<sub>2</sub> will affect the IR spectra of the N<sub>2</sub>-rich ice in central and southern Sputnik Planitia, where the ice exhibits decimeter-to-meter-scale “grain sizes.” The deposited ice may affect the albedo, emissivity, or the diurnal thermal inertia.

1640

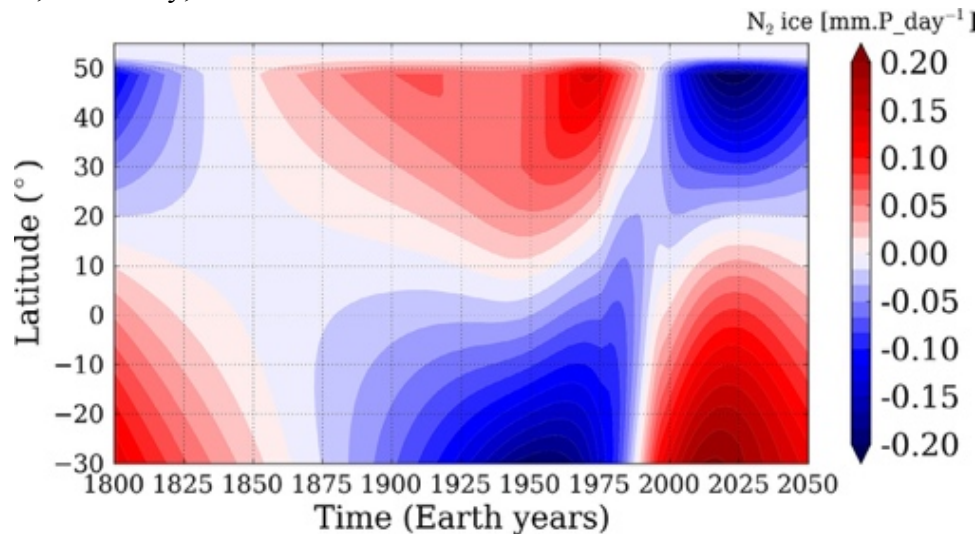


Fig. 14. Evolution of the diurnal mean condensation-sublimation rate within Sputnik Planitia (mm per Pluto day; red is condensation), in current orbital conditions, from 1800 to 2050 assuming that the glacier remains flat. Figure from Bertrand et al. 2018.

The very simple calculation of how a uniform surface covered with N<sub>2</sub>-ice reacts to the heliocentric distance varying from 29.7 to 49.9 AU, and ignoring thermal inertia, indicates that the N<sub>2</sub> equilibrium temperature would change by over 8 K, and the equilibrium pressure would change by three orders of magnitude. Some pre-encounter models predicted pressures that could drop precipitously and dramatically if the ices in the summer hemisphere were allowed to sublime completely, leaving only ices on the winter hemisphere (Trafton et al. 1998, Hansen & Paige 1996; Young 2013; Hansen et al. 2015). The equator receives less sunlight when averaged over a Pluto year, which led Trafton et al. (1988) to predict that the perennial N<sub>2</sub> ice (that persists over a Pluto year) would reside within 32° of the equator. HP96 simulated this with the high-thermal inertia run that they plotted (their Figure 3, 2093 tiu). In the other runs plotted in HP96, the equator is rarely the coldest latitude, and N<sub>2</sub> ice jumps over the equator to the winter polar cap, leaving the equator bare (again, Sputnik Planitia was unknown at this time). Very few runs in HP96 predicted perennial N<sub>2</sub> ice (termed “permanent zonal band” in HP96). Rather, the HP96 models generally showed two polar caps exchanging volatiles, with flow from the summer to the winter cap. The thermal inertia determined the timing of the new winter pole. Most HP96 models showed a steady increase in pressure after each equinox, as the old winter pole became the new summer pole and received more direct sunlight. Then, when the last of the N<sub>2</sub> from the summer pole sublimed away, sometime between perihelion and northern summer solstice, the pressure plummeted. The typical HP96 model runs therefore showed two pressure peaks per Pluto year.

1650

1660

Post-encounter, we see that the N<sub>2</sub> never leaves either summer hemisphere completely, as Sputnik Planitia ensures that there is always N<sub>2</sub> absorbing sunlight every day (Young et al 2015; Bertrand & Forget

2016; Meza et al. 2019; Johnson et al. 2020). This decreases the magnitude of the allowable pressure variation.

1670

Models that are tuned to observed pressure and have N<sub>2</sub> confined to Sputnik Planitia (Fig. 15; BF16; Johnson et al. 2020; Meza et al. 2019) have typical solutions with  $\Gamma \sim 700\text{-}800$  tiu,  $A \sim 0.7$ , and  $\epsilon \sim 0.65$  to 0.9 (or, more generally,  $(1-A)/\epsilon \sim 0.4$ ). In Pluto's current orbit, these models find that: (1) there is only one minimum and maximum every Pluto year, while pre-encounter models with completely mobile ices often had one maximum at each of the southern or northern summers; (2) the pressure maximum occurs near the time of maximum insolation on Sputnik Planitia, sometime between perihelion and northern solstice (that is, near in time of the New Horizons flyby and the writing of this Chapter), with a maximum pressure near 1.1 to 1.3 Pa (with a good match achieved by tuning the albedo and emissivity); (3) the pressure minimum occurs near northern winter solstice, but remains usually large enough to maintain a global atmosphere. Differences between the Meza et al. (2019) and Johnson et al (2020) predictions likely arose from the differences in the observational constraints. To some extent, the spatial resolution may play a role, since many of the N<sub>2</sub>-rich mid-latitude depressions were observed to be tens of km across.

1680

Surface pressures were modeled to peak within a decade of flyby (B16; Meza et al. 2019; Johnson et al. 2020). It is intriguing to think that we can test this observationally by measuring the time of the peak pressure from ground-based occultations, looking for a zero or negative slope in the change of pressure vs. time. Care must be taken in this search. Measuring a slope is more difficult than measuring a value. This is exacerbated because different methods for measuring the pressure have yielded different results (Section 2.1.3).

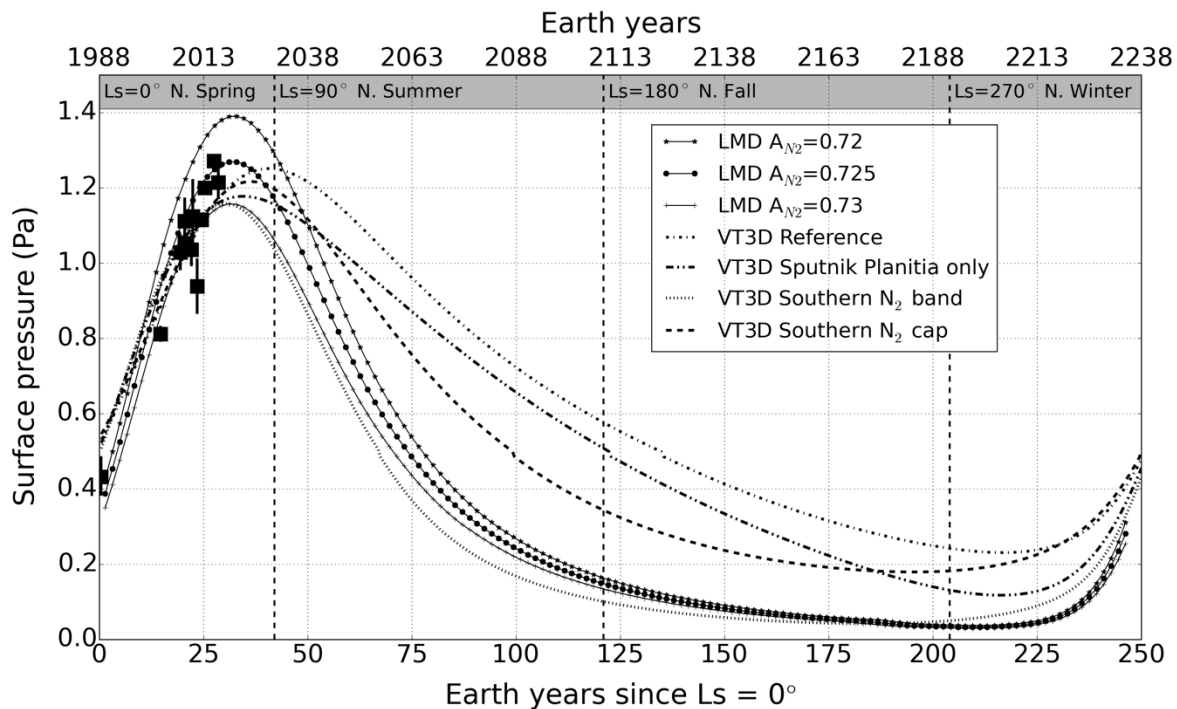


Fig. 15. Dashed: four models of pressure over a Pluto season for four assumptions of a static N<sub>2</sub>-ice distribution from Johnson et al. (2020): Sputnik only; the reference N<sub>2</sub>-presence map of Lewis et al. (2020); the N<sub>2</sub>-presence map plus a southern N<sub>2</sub> polar cap; or the presence map plus a southern N<sub>2</sub> mid-latitude band. Solid: Three models of pressure over a Pluto season from Meza et al. (2019). The vertical dashed lines mark the timing of solstices and equinoxes.

Outside of Sputnik Planitia, copious N<sub>2</sub>-rich ice is observed at mid latitudes, and in isolated spots at equatorial or high northern latitudes. Including these more-northerly deposits in models (Meza et al. 2019; Johnson et al. 2020) delays the timing of the maximum pressure by 5 to 15 years vs. a Sputnik-only N<sub>2</sub> reservoir and raises the highest pressure by ~30% (a consequence of the delayed date of the pressure peak, and the constraint that the 2015 pressure is near 1.1 Pa). Typical thermal inertias are similar to the Sputnik-only case, with very slightly larger albedos, and still with  $(1-A)/\epsilon \sim 0.4$ . Johnson et al. (2020) assumed the N<sub>2</sub>-rich ices controlling the pressure did not change in their locations, equivalent to stating that the pressure is controlled by the perennial N<sub>2</sub> deposits that remain over the course of a Pluto year. This is the case favored also by Meza et al. (2019). If the N<sub>2</sub>-free areas (including CH<sub>4</sub> ice) is relatively dark ( $A \sim 0.5$  for both polar and equatorial), then N<sub>2</sub> is confined in the northern hemisphere to Sputnik Planitia and permanent mid-latitude N<sub>2</sub> deposits in depressions, with almost no condensation in the southern hemisphere. In this case, Johnson et al. (2020) reference case and Meza et al. (2019) describe similar physical situations. The differences in the predicted surface pressure variation between these two models may be due to differences in the details of the distribution of the perennial N<sub>2</sub> deposits, as Johnson et al. (2020) constructed a map based on infrared spectra, and Meza et al. (2019) predicted where perennial N<sub>2</sub> would form self-consistently based on simulations and topographic models.

We have no compositional information south of 40°S. There are three approaches to the question of the distribution and evolution of southern N<sub>2</sub>. One is observational, from the historical albedo record. As described in Section 2.1, there is evidence for a bright southern pole in 1988. But since CH<sub>4</sub>-rich ice and N<sub>2</sub>-rich ice have similar albedos in Pluto's northern hemisphere, deriving composition from only albedo is difficult. For this reason, the historical albedo record has not yet been used to constrain any post-flyby volatile transport models. A second approach is to impose N<sub>2</sub> below 40°S, calculate its effects on pressures or haze production, and compare results to observations (Forget et al. 2017; Bertrand & Forget 2017; Meza et al. 2019; Johnson et al. 2020, Lewis et al. 2020). If too much N<sub>2</sub> is in the southern hemisphere, then pressures would not be increasing since 1988 as observed (Meza et al. 2019; Johnson et al. 2020), but solutions can be found with a southern cap (N<sub>2</sub> from 90°S to 60°S), or southern band (N<sub>2</sub> from 35°S to 55°S) that contain 20% N<sub>2</sub>-rich ice (Johnson et al. 2020). The southern-band solutions have substantially lower thermal inertias than other solutions (Johnson et al. 2020), consistent with the conclusions of Lewis et al. (2020) that solutions that ignore thermal inertia require southern N<sub>2</sub>-rich ice. The third approach is to derive the conditions under which the southern latitudes should be frost-covered or clear—that is, to see if models predict the formation of southern N<sub>2</sub>-rich ice.

Most pre-flyby models predicted seasonal southern N<sub>2</sub> (Hansen & Paige 1996; Young 2013; Hansen et al. 2015), but included no topographical data, as none was available. Post-flyby models with only the N<sub>2</sub> cycle has N<sub>2</sub>-rich ice only in the depression that is Sputnik Planitia (Bertrand et al. 2018), but the addition of CH<sub>4</sub> to models allows CH<sub>4</sub> condensation sites to then become N<sub>2</sub> condensation sites (Bertrand et al. 2019), unless the CH<sub>4</sub> is dark. The stability of N<sub>2</sub> outside of Sputnik Planitia or CH<sub>4</sub> at the equator or mid-

1730 to-high latitudes depends critically on the albedo (Fig. 16). The effect of albedo is particularly important in the diurnal zone (Earle et al. 2018a). Earle et al. (2018a) treated the darkening of ices with time due to haze deposition, and the subsequent brightening when new ice is laid down, and found that runaway albedo may get triggered over a single Pluto season.

For the class of runs with a uniformly dark  $\text{CH}_4$ , ( $A_{\text{CH}_4} \ll 0.6$ , Fig. 16, panel 2), B19 found that the  $\text{CH}_4$  remained too warm for  $\text{N}_2$  condensation. At mid-to-high latitudes, dark  $\text{CH}_4$  was not stable against sublimation, and formed only thin seasonal deposits. This class appeared to match the occultation record. Whether or not this class is viable depends critically on whether the observational evidence is for perennial or seasonal  $\text{N}_2$  or  $\text{CH}_4$  deposits at mid-to-high latitudes.

1740 For the class of runs with bright equatorial  $\text{CH}_4$  ( $A_{\text{CH}_4,eq} \gg 0.6$ , Fig. 16, panel 3), B19 found that  $\text{N}_2$  was able to condense on the Bladed Terrains and to remain very stable in these equatorial regions.  $\text{N}_2$  thus covered  $\text{CH}_4$  and shut down the  $\text{CH}_4$  cycle. No volatile deposits formed outside of the equator in these models, either seasonal or perennial. This did not match the volatile distribution seen at Pluto.

1750 For the class of runs with moderately bright equatorial  $\text{CH}_4$  ( $A_{\text{CH}_4,eq} \approx 0.6$ , Fig. 16, panels 4 and 5), B19 found that  $\text{N}_2$  was able to condense onto equatorial  $\text{CH}_4$ , but only in depressions, leaving high-altitude areas  $\text{CH}_4$ -rich, as observed. If the run also had dark mid-latitude/polar  $\text{CH}_4$  ( $A_{\text{CH}_4,polar} \ll 0.6$ , Fig. 16, panel 4), then the  $\text{CH}_4$  can form seasonal deposits at mid-to-high latitudes. B19 found that if the run has bright mid-latitude/polar  $\text{CH}_4$  (Fig. 16, panel 5), the  $\text{N}_2$  was able to condense onto it, trap more  $\text{CH}_4$  and result in more perennial  $\text{CH}_4$  ice deposits at mid latitudes (the  $\text{CH}_4$  deposits remained seasonal at the poles in all cases). The moderately bright equatorial, bright polar  $\text{CH}_4$  class reproduced some of the observed trends in surface volatiles:  $\text{N}_2$  in depressions; seasonal  $\text{N}_2$  and  $\text{CH}_4$  at midlatitudes; and seasonal  $\text{N}_2$  at the poles.

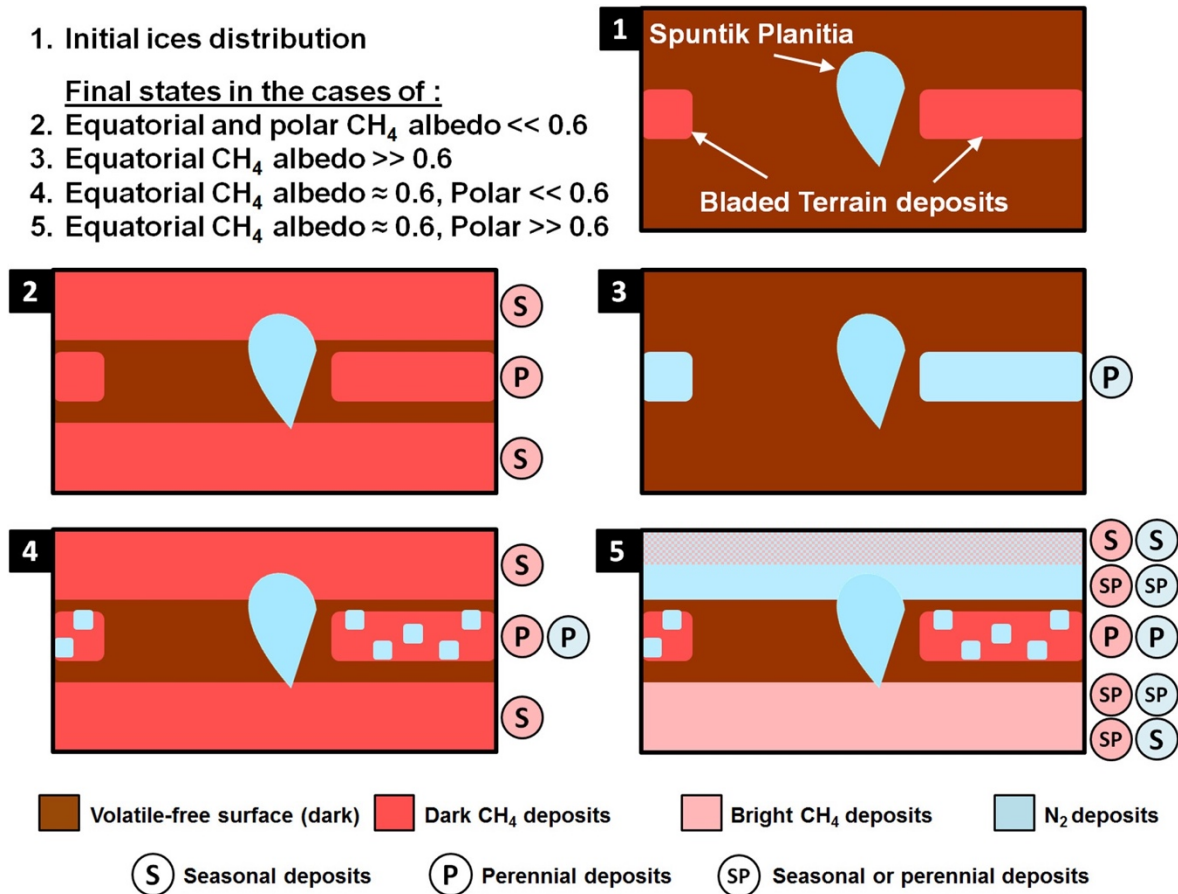


Fig 16. Summary of the simulation results for runs with that were initialized with N<sub>2</sub> in Sputnik Planitia, and an infinite reservoir of CH<sub>4</sub> at the latitudes and longitudes of the Bladed Terrain (Bertrand et al. 2019; their Section 4).

Returning to pressure over a season, Bertrand et al. (2019) found that southern N<sub>2</sub> tended to lead to an earlier peak in pressure, near 2010, but Johnson et al. (2020) were able to find solutions that matched the 1988-2015 occultation record, with either a southern N<sub>2</sub> cap, or a southern mid-latitude band with N<sub>2</sub> areal fraction of 20%. Even with some southern N<sub>2</sub>-rich ice, most post-flyby models predict that Pluto's atmosphere will maintain a global atmosphere over Pluto's year with current obliquity and orbital conditions (Johnson et al 2020; Bertrand & Forget 2016; Meza et al. 2019). This was also indicated by some of the pre-New Horizons models (Trafton 1990; Stansberry & Yelle 1999; Olkin et al. 2015).

Higher minimum pressure is partly due to the effect of the high seasonal thermal inertia of the substrate, which enables the poles to store the heat accumulated during summer and to release it during winter. The poles thus remain too warm for N<sub>2</sub> condensation. It is also partly due to the near-equatorial location of Sputnik Planitia, ensuring insolation on N<sub>2</sub>-ices even during northern winter. The pressure maximum and minimum can be more extreme during times when northern solstice coincides with perihelion (Johnson et al 2020; Bertrand et al. 2018). In the LMD and VT3D models, the minimum surface pressure generally stays above 6 mPa, and so is likely always global, although it is possible to have lower pressures in some Pluto orbital configurations for some model inputs (Johnson et al 2020; Bertrand et al. 2018).

In those post-flyby models that include CO and CH<sub>4</sub> (Bertrand & Forget 2016; Bertrand et al. 2019), the CO tends to follow N<sub>2</sub> and condense where N<sub>2</sub>-rich deposits are already present, in agreement with observations. Bertrand and Forget (2016), showed that 0.3% CO (Merlin et al., 2015) in N<sub>2</sub>-rich ice filling Sputnik Planitia leads to an atmospheric mean gas volume mixing ratio close to 0.04% in 2015, in good agreement with telescopic measurements (Lellouch et al., 2011). They also showed that without the presence of permanent N<sub>2</sub>-rich deposits, the CO gas mixing ratio would reach 20%–30% in 2010, which is unrealistic and reinforces the picture of a permanent cold trap in Sputnik Planitia.

1780 Outside of Sputnik Planitia, New Horizons detected clear latitudinal trends for the volatiles on Pluto. CH<sub>4</sub>-rich ice was seen northward of 55°N, N<sub>2</sub>-rich ice between 35°N and 55°N, and CH<sub>4</sub>-rich ice between 20°N and 35° N (Schmitt et al., 2017, Protopapa et al., 2017, Earle et al., 2018b). The N<sub>2</sub>-rich band may be the seasonally varying remnant of two opposing sublimation fronts (Protopapa et al. 2017): a slowly moving north-bound front driven by low-latitude heating from 1975 to 1995; and a more rapid south-bound front driven by high-latitude heating from 1995 to 2015, particularly 2005 to 2015. The effect of solar insolation on the CH<sub>4</sub> distribution is supported by simulations (Bertrand & Forget 2016; Bertrand et al. 2019) that reproduce, to first order, the spatial distribution of N<sub>2</sub> and CH<sub>4</sub> ices observed in 2015 outside Sputnik Planitia. In these simulations, when the mid-latitude/polar CH<sub>4</sub>-rich ice is bright ( $A > 0.65$ ), it gets cold enough in autumn and winter that N<sub>2</sub> condenses on it and forms seasonal or perennial N<sub>2</sub>-rich deposits at mid-latitudes, as observed. Seasonal or perennial CH<sub>4</sub> deposits may even form on dark, low-latitude terrains during winter, consistent with the low-latitude band of CH<sub>4</sub>-rich ice (Protopapa et al. 2017; Earle et al., 2018b).

1790 Whether the two sublimation fronts will meet (Protopapa et al. 2017) is related to the core question of whether the mid-latitude N<sub>2</sub> ice is seasonal (varying greatly—perhaps completely subliming—every Pluto orbit) or perennial (slowly growing or shrinking over the timescale of many Pluto orbits).

Bertrand and Forget (2016) predicted a range of atmospheric CH<sub>4</sub> mixing ratio from 0.1% to 5% over current Pluto's year. A larger ratio could be expected in northern winter, when most post-flyby models predict that the atmosphere will be thinner by orders of magnitudes and would thus provide less dilution of methane.

#### 5.4 Diurnal

1800 Much of the diurnal volatile cycle involves the winds transporting heat and mass across the surface, and the vertical winds (also sometimes called “atmospheric breathing”) from local sublimation and condensation, as described in the Chapter on atmospheric dynamics by Forget et al. There are few direct observational constraints on the diurnal cycle.

Sputnik Planitia is mainly within the diurnal zone, and so experiences sunrise and sunset every single Pluto day for the last tens of Myr or longer. The higher noontime insolation is balanced by sublimation, with diurnal variation of only ~mK for N<sub>2</sub>-rich ice temperature, or ~mPa for surface pressure (Young 2012; Forget et al. 2017). At the time of flyby, superimposed on the net north-south transport within Sputnik Planitia, tens of g m<sup>-2</sup> of fresh N<sub>2</sub> condensed and sublimed each day (Forget et al. 2017, their Fig 8), equivalent to a depth of several tens of microns of N<sub>2</sub>-rich ice. It is likely that this thin diurnal ice layer

1810 is too thin to be detectable spectroscopically in the near-IR. The N<sub>2</sub>-rich ice outside of Sputnik Planitia, like the ice within Sputnik Planitia, is also likely to stay nearly isothermal.

The daily sublimation of tens of g m<sup>-2</sup> of N<sub>2</sub> corresponds to about 2 km of cold N<sub>2</sub> gas being injected into Pluto's lower atmosphere over Sputnik Planitia each day (Hinson et al. 2017; Forget et al. 2017). The cold boundary layer was directly detected in the REX ingress profile (Hinson et al. 2017; Forget et al. 2017). The daily sublimation and condensation cycles induce vertical winds that vary in magnitude on a daily cycle. These may force waves that are detectable as layers seen in haze images (Forget et al. 2017) or the density and temperature variations seen in ground-based occultations (Toigo et al. 2010; French et al. 2015).

1820 Areas free of N<sub>2</sub> over a day will be warmer than the N<sub>2</sub>-rich ice. The temperatures of non-volatile terrains are not buffered by the latent heat of sublimation, and tend to be warmer due to their lower albedo. The temperatures of CH<sub>4</sub>-rich ices are buffered by latent heat only somewhat. Forget et al. (2017) modeled CH<sub>4</sub> temperatures that range from just slightly warmer than the N<sub>2</sub>-rich ice to 52 K in isolated polar areas. Thermal models based on the pre-encounter composition maps and constrained by ISO, Spitzer, and Herschel thermal observations favor low thermal inertia for the diurnal skin depth, and predict CH<sub>4</sub> temperatures that also reach a localized maximum of 54 K (Lellouch et al. 2000, 2011, 2016).

If a CH<sub>4</sub>-rich or non-volatile area becomes cold enough, it would become an N<sub>2</sub> condensation site. Would volatiles condense overnight and be visible at the dawn limb? Such a search will probably wait for an orbiter, since the equatorial dawn limb was only imaged by New Horizons after the solar occultation, at high phase angle and low spatial resolution.

1830 CH<sub>4</sub>-rich areas that do not become N<sub>2</sub> condensation sites will be warmer than the N<sub>2</sub>-rich ice, and will be CH<sub>4</sub> condensation or sublimation sites depending on whether they are cooler or warmer than the critical temperature (Eq. 5), which is 42.1 K for pure CH<sub>4</sub> ice (slightly warmer for CH<sub>4</sub>-rich ice saturated with N<sub>2</sub>). The CH<sub>4</sub> mass flux will vary with location and time of day. The diurnal variation at a given location is only 3 to 6 K (Forget et al. 2017). Considering a 3 K temperature range around 42.1 K, and using  $U_* C_m \sim 0.22 \text{ cm s}^{-1}$  ( $U_*$  is the friction velocity, and  $C_m$  is the mass transfer coefficient, Forget et al. 2017), the mass rates are about 0.1 micron of condensation per Pluto day at 40.6 K, and 0.3 microns of sublimation per Pluto day at 43.6 K. Thus, the daily cycle of CH<sub>4</sub> sublimation and condensation is small. It is also asymmetric, with sublimation being more efficient than condensation, which will contribute to the net mass flux of CH<sub>4</sub> into the atmosphere averaged over many Pluto days. This asymmetry might impact Pluto's surface and atmosphere on longer timescales (seasonal or longer), but this effect has not  
1840 yet been studied.

## 6. Conclusions and Future Work

Pluto complements Triton, Io, and Mars as examples of vapor-pressure-equilibrium atmospheres. In the outer solar system, Pluto is unique, both for its intrinsic properties (the surface complexity; the presence of Sputnik Planitia; the prevalence of both CH<sub>4</sub> and N<sub>2</sub>), and for the rich collection of observations (the New Horizons surface maps of geology, topography, and critically, composition; the UV and radio occultations and a nearly simultaneous ground-based stellar occultation; the long time-base

of occultations and other Earth-based observations). Pluto has already allowed us to study the effects of albedo, emissivity, thermal inertia, topography, and Milankovitch-like orbital variation on the volatile and climate cycles. It is poised to be a laboratory in which to study the physics of ice mixtures, the N<sub>2</sub> α-β phase transition, albedo feedbacks, and the role of ice contamination by haze particles.

While great strides have been already made, important open questions remain.

- **How do the CH<sub>4</sub>-N<sub>2</sub> thermodynamics impact the volatile transport on Pluto, and the vertical structure of Pluto's ices?** New Horizons found that while both N<sub>2</sub>-rich and CH<sub>4</sub>-rich phases of ice are present, the N<sub>2</sub>-rich ice is not saturated with CH<sub>4</sub>. This is surprising because the N<sub>2</sub>-rich ice is expected to saturate before any CH<sub>4</sub>-rich ice forms. The lack of saturation is even more surprising given the excess of CH<sub>4</sub> in Pluto's atmosphere. Part of the solution may lie in the formation of CH<sub>4</sub>-rich ices during sublimation, as calculated by Tan & Kargel (2018). Part of the solution may also be the complex interplay between the creation of a CH<sub>4</sub>-rich layer at the surface-atmosphere interface (Schmitt et al. 2017; Trafton et al. 1998, 2019), the annealing rate of newly deposited N<sub>2</sub>-rich ice (Eluszkiewicz 1991; Young et al. 2019), and the sublimation of N<sub>2</sub> some cm below the surface and redeposition near the surface from solar gardening (Grundy and Stansberry 2000).

- **Where are the seasonal and perennial ices? Which ices have built up over millions of years?** Prior to New Horizons, many models imagined a small inventory of N<sub>2</sub> ice moving across Pluto, alternately covering up and revealing substrate. One of the many ways in which Sputnik Planitia has shaken our concepts of "how Pluto works" is the new picture of a large reservoir of N<sub>2</sub>, and the transport of atmospheric N<sub>2</sub> between perennial deposits of N<sub>2</sub> ice that last over many Pluto orbits. The CH<sub>4</sub> ice, also, appears to have some deposits that come and go over a Pluto orbit, but also large deposits, such as the Bladed Terrain, that must have taken millions of years to build. When did the Bladed Terrain form, and are they current disappearing? Why is the Bladed Terrain located east of Sputnik Planitia, whereas the regions west of Sputnik Planitia are depleted in volatile ices? How and when did the extensive CH<sub>4</sub> mantles north and east of Sputnik Planitia form? Does the process of CH<sub>4</sub> segregation feed the atmosphere with more gaseous CH<sub>4</sub> that will form CH<sub>4</sub> rich deposits elsewhere, incidentally preventing CH<sub>4</sub> from entirely migrating into Sputnik Planitia? These questions are also tied to estimates of the current total volatile inventory derived from composition maps, since seasonal deposits will be shallower than perennial ones. The depth of current or past deposits is also connected to the question of glacial flows, since N<sub>2</sub> is more ductile (or, perhaps, even liquid) under the pressure of deep ice deposits.

- **What is the composition, history, and evolution of the southern hemisphere?** Historical photometry argues for a bright southern polar cap, pre-equinox. If the bright southern cap was N<sub>2</sub>-rich, then it should have remained an N<sub>2</sub>-rich condensation site during the ensuing darkness. However, many models made after New Horizons suggest that the unseen southern hemisphere should be free of N<sub>2</sub> in order to match the occultation record. It is not clear how to reconcile these. The south pole will not be seen again from Earth until 2109.

- **What are the processes that change albedo, composition, or other thermophysical properties of the volatile ices? What drives the strong contrasts in color on Pluto's surface?** Albedo sets up a positive feedback, particularly in the diurnal climate zone, but, except for Sputnik Planitia, it is unclear how this is triggered. Albedo could be a function of age if ices are processed by UV and energetic particles,

1890 or if ices are contaminated by sedimenting haze particles—all of which are also affected by the atmospheric conditions, so there could be complex feedbacks. Thin (seasonal) deposits may allow the albedo of the underlying material to control the energy balance. The N<sub>2</sub> grain size depends on the deposition rate, and the effect of “solar gardening” can increase porosity (and thermal inertia) at depth and decrease it at the upper-most layer.

1900 One approach to addressing these questions is to improve future models to account for additional processes: the alteration of albedo and other surface properties; the interaction of CH<sub>4</sub> and N<sub>2</sub>; the CH<sub>4</sub> cycle over astronomical timescales. With higher fidelity comes increased complexity, as many elements of these processes remain unknown or not well constrained. In order to further understand the processes at play on Pluto (and on many other KBOs), observations, modeling and experiments will need to be combined. Experiments on ice mixtures are needed, to test the predictions of Tan & Kargel (2018), and to study the behavior of N<sub>2</sub>, CO, and CH<sub>4</sub> in disequilibrium. We only have atmospheric data over a tenth of Pluto’s year, during which time we observed a tripling of the surface pressure. Ground based observations of pressure (stellar occultations), surface temperature (thermal radiometry), atmospheric and surface composition (spectroscopy), and surface albedo (visible imagery) are needed at least every few Earth years in order to further constrain the models. Our current puzzlement would serve well in the design of any future mission to Pluto. While our understanding of Pluto’s volatile cycles has considerably increased thanks to the New Horizons observations, the flyby of Pluto in 2015 only provided a snapshot in time of Pluto’s dynamic and evolving surface and atmosphere, only 40% of the total surface was imaged, and the atmosphere was probed at only a few distinct locations. An orbiter mission is needed to continue to explore and understand Pluto, and in particular how its surface and atmosphere evolve with time and are shaped by complex volatile transport processes. As the breakthrough observations of the 1980’s and 1990’s allowed us to take the first steps toward understanding Pluto’s volatiles, and New Horizons gave Pluto science one giant leap, the combination of new modeling, lab work, observations, and a possible return to Pluto will lift us to new heights.

## Acknowledgments

1920 We are grateful to Candy Hansen, Alan Howard, and Alan Stern for their reviews of this chapter. LY was supported in part by NASA ROSES SSW grant NNX15AH35G and by NASA’s New Horizons mission to the Pluto system. TB was supported for this research by an appointment to the National Aeronautics and Space Administration (NASA) Post-doctoral Program at the Ames Research Center administered by Universities Space Research Association (USRA) through a contract with NASA. LMT was supported by NASA Grant 80-NSSC18K0860. FF and TB benefited from support from CNES. AME was supported in part by the NASA New Horizons mission to Pluto and The Kuiper Belt under SwRI Subcontract 299433Q. The work by BS leading to these results has received funding from the European Research Council under the European Community's H2020 2014-2020 ERC Grant Agreement n°669416 "Lucky Star."

## References

- Andersson, L. E. and J. D. Fix 1973. Pluto: New Photometry and a Determination of the Axis of Rotation. *Icarus* 20, 279-283.
- Aumann, H. H. and R. G. Walker 1987. IRAS Observations of the Pluto-Charon System. *The Astronomical Journal* 94, 1088.
- Bertrand, T. and F. Forget 2016. Observed glacier and volatile distribution on Pluto from atmosphere-topography processes. *Nature* 540, 86-89. [BF19]
- 1930 Bertrand, T. and F. Forget 2017. 3D modeling of organic haze in Pluto's atmosphere. *Icarus* 287, 72-86.
- Bertrand, T., and 14 colleagues 2018. The nitrogen cycles on Pluto over seasonal and astronomical timescales. *Icarus* 309, 277-296.
- Bertrand, T., and 16 colleagues 2019. The CH<sub>4</sub> cycles on Pluto over seasonal and astronomical timescales. *Icarus* 329, 148-165.
- Bertrand T., Forget F., White O., and Schmitt B. 2020a Pluto's beating heart regulates the atmospheric circulation: Results from high resolution and multi-year numerical climate simulations. *J. Geophys. Res.*, 125, e2019JE006120.
- 1940 Bertrand, T., Forget, F., Schmitt, B., White, O. and Grundy, W., 2020b. How seasonal methane snow form on Pluto on mountain's top, crater rims and slopes. Submitted to *Nature Communication*.
- Binzel, R. P. and W. B. Hubbard 1997. Mutual Events and Stellar Occultations. *Pluto and Charon In Pluto and Charon*, eds. S. A. Stern and D. Tholen (U. Arizona Press, Tucson), pp. 85-102.
- Bockelée-Morvan, D., E. Lellouch, N. Biver, G. Paubert, J. Bauer, P. Colom, and D. C. Lis 2001. Search for CO gas in Pluto, Centaurs and Kuiper Belt objects at radio wavelengths. *Astronomy and Astrophysics* 377, 343-353.
- Brosch, N. 1995. The 1985 stellar occultation by Pluto. *Mon. Not. R. Astron. Soc.* Vol 276, 571-578.
- Buhler, P. B. and A. P. Ingersoll 2018. Sublimation pit distribution indicates convection cell surface velocities of ~10 cm per year in Sputnik Planitia, Pluto. *Icarus* 300, 327-340.
- 1950 Buie, M. W. and W. M. Folkner 2015. Astrometry of Pluto from 1930-1951 Observations: the Lampland Plate Collection. *The Astronomical Journal* 149, 22.
- Buie, M. W., W. M. Grundy, E. F. Young, L. A. Young, and S. A. Stern 2010a. Pluto and Charon with the Hubble Space Telescope. I. Monitoring Global Change and Improved Surface Properties from Light Curves. *The Astronomical Journal* 139, 1117-1127.
- Buie, M. W., W. M. Grundy, E. F. Young, L. A. Young, and S. A. Stern 2010b. Pluto and Charon with the Hubble Space Telescope. II. Resolving Changes on Pluto's Surface and a Map for Charon. *The Astronomical Journal* 139, 1128-1143.
- Buratti, B. J., J. K. Hillier, A. Heinze, M. D. Hicks, K. A. Tryka, J. A. Mosher, J. Ward, M. Garske, J. Young, and J. Atienza-Rosel 2003. Photometry of Pluto in the last decade and before: evidence for volatile transport?. *Icarus* 162, 171-182.
- 1960

Buratti, B. J., M. D. Hicks, P. A. Dalba, D. Chu, A. O'Neill, J. K. Hillier, J. Masiero, S. Banholzer, and H. Rhoades 2015. Photometry of Pluto 2008-2014: Evidence of Ongoing Seasonal Volatile Transport and Activity. *The Astrophysical Journal* 804, L6.

Buratti, B. J., and 16 colleagues 2017. Global albedos of Pluto and Charon from LORRI New Horizons observations. *Icarus* 287, 207-217.

Butler, H. J., M. A. Gurwell, E. Lellouch, T. Fouchet, D. Lis, R. Moreno, A. Moullet, S. A. Stern, and L. A. Young 2019. Emission from Pluto and Charon at Long Wavelengths: Observations using ALMA, SMA, and VLA. Submitted to *AJ*.

1970 Carson, J. K., S. J. Lovatt, D. J. Tanner, A. C. Cleland and 2005. Thermal conductivity bounds for isotropic, porous materials. *International Journal of Heat and Mass Transfer* 48, 2150-2158,

Cruikshank, D. P., Pilcher, C. B., and Morrison, D. 1976. Pluto: Evidence for methane frost. *Science* 194, 835-837.

Cruikshank, D. P., and Silvaggio, P. M., 1980. The surface and atmosphere of Pluto. *Icarus* 41, 96-102.

Cruikshank, D. P., and 12 colleagues 2015. The surface compositions of Pluto and Charon. *Icarus* 246, 82-92.

DeMeo, F. E., C. Dumas, C. de Bergh, S. Protopapa, D. P. Cruikshank, T. R. Geballe, A. Alvarez-Candal, F. Merlin, and M. A. Barucci 2010. A search for ethane on Pluto and Triton. *Icarus* 208, 412-424.

Desmars, J., and 15 colleagues 2019. Pluto's ephemeris from ground-based stellar occultation (1988–2016). *Astronomy and Astrophysics Vol 625*, A43

1980 Dias-Oliveira et al. 2015. Pluto's atmosphere from stellar occultations in 2012 and 2013. *Astron. J. Vol* 811, 53

Dobrovolskis, A. R., S. J. Peale, and A. W. Harris 1997. Dynamics of the Pluto-Charon Binary. *Pluto and Charon* 159.

Douté, S., B. Schmitt, E. Quirico, T. C. Owen, D. P. Cruikshank, C. de Bergh, T. R. Geballe, and T. L. Roush 1999. Evidence for Methane Segregation at the Surface of Pluto. *Icarus* 142, 421-444.

Duxbury, N. S. and R. H. Brown 1993. The Phase Composition of Triton's Polar Caps. *Science* 261, 748-751.

Earle, A. M. 2018. Spectral Mapping and Long-Term Seasonal Evolution of Pluto. Ph.D. Thesis. Massachusetts Institute of Technology.

1990 Earle, A. M., R. P. Binzel, L. A. Young, S. A. Stern, K. Ennico, W. Grundy, C. B. Olkin, H. A. Weaver, and New Horizons Geology and Geophysics Imaging Team 2017. Long-term surface temperature modeling of Pluto. *Icarus* 287, 37-46.

Earle, A.M., and 7 colleagues 2018a. Albedo Matters: Understanding runaway albedo variations on Pluto. *Icarus* 303, 1-9.

Earle, A. M., and 19 colleagues 2018b. Methane distribution on Pluto as mapped by the New Horizons Ralph/MVIC instrument. *Icarus* 314, 195-209.

Eglitis, I., M. Eglite, L. V. Kazantseva, S. V. Shatokhina, Y. I. Protsyuk, O. E. Kovylianskaya, and V. M. Andruk 2018. Astrometric and photometric processing of Pluto digitized photographic observations 1961- 1996. *Results of Processing of Digitized Astronomical Photographic Plates* 37-40.

- 2000 Elliot, J. L., E. W. Dunham, A. S. Bosh, S. M. Slivan, L. A. Young, L. H. Wasserman, and R. L. Millis 1989. Pluto's atmosphere. *Icarus* 77, 148-170.
- Elliot, J. L. and L. A. Young 1992. Analysis of Stellar Occultation Data for Planetary Atmospheres. I. Model Fitting Application to Pluto. *The Astronomical Journal* 103, 991.
- Elliot, J.L. and Olkin, C.B. 1996. Probing planetary atmospheres with stellar occultations. *Annual Review of Earth and Planetary Sciences*, Vol 24, 89-124
- Elliot, J. L., and 28 colleagues 2003. The recent expansion of Pluto's atmosphere. *Nature* Vol 424, 165-168
- Elliot, J. L., Person, M. J. and Qu, S. 2003. Analysis of stellar occultation data. II. Inversion, with application to Pluto and Triton. *Astronomical Journal* Vol 126, 1041-1079
- 2010 Elliot, J. L. and 19 colleagues 2007. Changes in Pluto's atmosphere: 1988-2006. *Astronomical Journal* Vol 134, 1-13
- Eluszkiewicz, J. 1991. On the microphysical state of the surface of Triton. *Journal of Geophysical Research* 96, 19217-19229.
- Fink, U., Smith, B. A., Johnson, J. R., Reitsema, H. H., Benner, D. C., Westphal, J. A. 1980. Detection of a CH<sub>4</sub> atmosphere on Pluto. *Icarus* 44, 62-71.
- Forget, F., T. Bertrand, M. Vangvichith, J. Leconte, E. Millour, and E. Lellouch 2017. A post-new horizons global climate model of Pluto including the N<sub>2</sub>, CH<sub>4</sub> and CO cycles. *Icarus* 287, 54-71.
- Forget, F., Hourdin, F., Fournier, R., Hourdin, C., Talagrand, O., Collins, M., Lewis, S.R., Read, P.L., Huot, J.-P. (1999). Improved general circulation models of the martian atmosphere from the surface to above 80 km. *J. Geophys. Res.* **104** (24), 155–176 .
- 2020 Fray, N. and B. Schmitt 2009. Sublimation of ices of astrophysical interest: A bibliographic review. *Planetary and Space Science* 57, 2053-2080.
- French, R. G., A. D. Toigo, P. J. Gierasch, C. J. Hansen, L. A. Young, B. Sicardy, A. Dias-Oliveira, and S. D. Guzewich 2015. Seasonal variations in Pluto's atmospheric tides. *Icarus* 246, 247-267.
- Gabasova, L. et al. 2020. Global compositional cartography of Pluto from intensity-based registration of LEISA data. Submitted to *Icarus*, Nov 11. 2019.
- Gladstone et al. 2016. The atmosphere of Pluto as observed by New Horizons. *Science* Vol. 351, aad8866
- Glein, C. R. and J. H. Waite 2018. Primordial N<sub>2</sub> provides a cosmochemical explanation for the existence of Sputnik Planitia, Pluto. *Icarus* 313, 79-92.
- 2030 Greaves, J. S., C. Helling, and P. Friberg 2011. Discovery of carbon monoxide in the upper atmosphere of Pluto. *Monthly Notices of the Royal Astronomical Society* 414, L36-L40.
- Grundy, W. M. 1995. Methane and Nitrogen Ices on Pluto and Triton: a Combined Laboratory and Telescope Investigation., Ph.D. Thesis, University of Arizona.
- Grundy, W.M. and Buie, M.W., 2002. Spatial and compositional constraints on non-ice components and H<sub>2</sub>O on Pluto's surface. *Icarus* 157, 128–138.
- Grundy, W.M. and Fink, U., 1996. Synoptic CCD spectrophotometry of Pluto over the past 15 years. *Icarus* 124, 329–343.

- 2040 Grundy, W. M., C. B. Olkin, L. A. Young, M. W. Buie, and E. F. Young 2013. Near-infrared spectral monitoring of Pluto's ices: Spatial distribution and secular evolution. *Icarus* 223, 710-721.
- Grundy, W. M., C. B. Olkin, L. A. Young, and B. J. Holler 2014. Near-infrared spectral monitoring of Pluto's ices II: Recent decline of CO and N<sub>2</sub> ice absorptions. *Icarus* 235, 220-224.
- Grundy et al. 2016. Surface compositions across Pluto and Charon. *Science* Vol. 351, aad9189
- Gulbis, A. A. S., J. P. Emery, M. J. Person, A. S. Bosh, C. A. Zuluaga, J. M. Pasachoff, and B. A. Babcock 2015. Observations of a successive stellar occultation by Charon and graze by Pluto in 2011: Multiwavelength SpeX and MORIS data from the IRTF. *Icarus* 246, 226-236.
- Hamilton, D. P., and 19 colleagues 2016. The rapid formation of Sputnik Planitia early in Pluto's history. *Nature* 540, 97-99.
- 2050 Hansen, C. J. and D. A. Paige 1996. Seasonal Nitrogen Cycles on Pluto. *Icarus* 120, 247-265.
- Hansen, C. J., D. A. Paige, and L. A. Young 2015. Pluto's climate modeled with new observational constraints. *Icarus* 246, 183-191.
- Hinson, D. P., and 15 colleagues 2017. Radio occultation measurements of Pluto's neutral atmosphere with New Horizons. *Icarus* 290, 96-111.
- Hofgartner, J. D, B. J. Buratti, P. O. Hayne, L. A. Young 2019. Ongoing resurfacing of KBO Eris by volatile transport in local, collisional, sublimation atmosphere regime. *Icarus*, in press. <https://doi.org/10.1016/j.icarus.2018.10.028>.
- Hourdin, F., P. Le van, F. Forget, and O. Talagrand 1993. Meteorological Variability and the Annual Surface Pressure Cycle on Mars. *Journal of Atmospheric Sciences* 50, 3625-3640.
- Howard, A. D., and 14 colleagues 2017a. Present and past glaciation on Pluto. *Icarus* 287, 287-300.
- 2060 Howard, A. D., and 16 colleagues 2017b. Pluto: Pits and mantles on uplands north and east of Sputnik Planitia. *Icarus* 293, 218-230.
- Howell, S. B., E. P. Horch, M. E. Everett, and D. R. Ciardi 2012. Speckle Camera Imaging of the Planet Pluto. *Publications of the Astronomical Society of the Pacific* 124, 1124.
- Hubbard, W. B., D. M. Hunten, S. W. Dieters, K. M. Hill, and R. D. Watson 1988. Occultation evidence for an atmosphere on Pluto. *Nature* 336, 452-454.
- Hubbard, W. B., R. V. Yelle, and J. I. Lunine 1990. Nonisothermal Pluto atmosphere models. *Icarus* 84, 1-11.
- Hubbard, W. 2003. Planetary science: Pluto's atmospheric surprise. *Nature* 424, 137-138.
- Hunten, D. M., and Watson, A. J. 1982. Stability of Pluto's atmosphere. *Icarus* 51, 665-667.
- 2070 Ingersoll, A.P., Summers, M.E., Schlipf, S.G., 1985. Supersonic meteorology of Io: Sublimation-driven flow of SO<sub>2</sub>. *Icarus* 64, 375-390.
- Jewitt, D. C. 1994. Heat From Pluto. *The Astronomical Journal* 107, 372.
- Johnson, P. E., L. A. Young, S. Protopapa, B. Schmitt, L. R. Gabasova, B. L. Lewis, J. A. Stansberry, K. E. Mandt, O. L. White 2020. Modeling Pluto's Minimum Pressure: Implications for Haze Production. Submitted to *Icarus*.
- Krasnopolsky, V. A. 2020. A photochemical model of Pluto's atmosphere and ionosphere. *Icarus* 335, 113374.

- Leighton, R. B. and Murray, B. C. 1966. Behavior of carbon dioxide and other volatiles on Mars. *Science*, 153, 136-144.
- 2080 Lellouch, E. 1994. The Thermal Structure of Pluto's Atmosphere: Clear vs Hazy Models. *Icarus* 108, 255-264.
- Lellouch, E., R. Laureijs, B. Schmitt, E. Quirico, C. de Bergh, J. Crovisier, and A. Coustenis 2000. Pluto's Non-isothermal Surface. *Icarus* 147, 220-250.
- Lellouch, E., de Bergh, C., Sicardy, B., Ferron, S., and Käufl, H.-U.: Detection of CO in Triton's atmosphere and the nature of surface-atmosphere interactions, *Astronomy and Astrophysics*, Vol 512, pp L8, 2010.
- Lellouch, E., C. de Bergh, B. Sicardy, H. U. Käufl, and A. Smette 2011a. High resolution spectroscopy of Pluto's atmosphere: detection of the 2.3  $\mu\text{m}$  CH<sub>4</sub> bands and evidence for carbon monoxide. *Astronomy and Astrophysics* 530, L4.
- 2090 Lellouch, E., J. Stansberry, J. Emery, W. Grundy, and D. P. Cruikshank 2011b. Thermal properties of Pluto's and Charon's surfaces from Spitzer observations. *Icarus* 214, 701-716.
- Lellouch, E., C. de Bergh, B. Sicardy, F. Forget, M. Vangvichith, and H.-U. Käufl 2015. Exploring the spatial, temporal, and vertical distribution of methane in Pluto's atmosphere. *Icarus* 246, 268-278.
- Lellouch, E., and 11 colleagues 2016. The long-wavelength thermal emission of the Pluto-Charon system from Herschel observations. Evidence for emissivity effects. *Astronomy and Astrophysics* 588, A2.
- Lellouch, E., and 18 colleagues 2017. Detection of CO and HCN in Pluto's atmosphere with ALMA. *Icarus* 286, 289-307.
- 2100 Lewis, B. L., J. A. Stansberry, B. J. Holler, W. M. Grundy, B. Schmitt, S. Protopapa, C. Lisse, S. A. Stern, L. Young, H. A. Weaver, Catherine Olkin, Kimberly Ennico, and the New Horizons Science Team. Distribution and Energy Balance of Pluto's Nitrogen Ice, as seen by New Horizons in 2015. *Icarus*, in production.
- Marcialis, R. L. and L. A. Lebofsky 1991. CVF spectrophotometry of Pluto: Correlation of composition with Albedo. *Icarus* 89, 255-263.
- McKinnon, W. B., and 61 colleagues 2016. Convection in a volatile nitrogen-ice-rich layer drives Pluto's geological vigour. *Nature* 534, 82-85.
- Merlin, F., M. A. Barucci, C. de Bergh, F. E. DeMeo, A. Alvarez-Candal, C. Dumas, and D. P. Cruikshank 2010. Chemical and physical properties of the variegated Pluto and Charon surfaces. *Icarus* 210, 930-943.
- 2110 Merlin, F. 2015. New constraints on the surface of Pluto. *Astronomy and Astrophysics* 582, A39.
- Meza, E., and 169 colleagues 2019. Lower atmosphere and pressure evolution on Pluto from ground-based stellar occultations, 1988-2016. *Astronomy and Astrophysics* 625, A42.
- Moore et al. 2016. The geology of Pluto and Charon through the eyes of New Horizons. *Science* Vol. 351, 1284-1993
- Moore, J. M., and 25 colleagues 2018. Bladed Terrain on Pluto: Possible origins and evolution. *Icarus* 300, 129-144.

Moore, J. E., C. L. Smith, A. D. Toigo, and S. D. Guzewich 2017. Penitentes as the origin of the bladed terrain of Tartarus Dorsa on Pluto. *Nature* 541, 188-190. [Note to typesetter: Yes, this is “Moore,” not “Moore.”]

2120 Nadeau, A. and R. McGehee 2017. A simple formula for a planet's mean annual insolation by latitude. *Icarus* 291, 46-50.

Nadeau, A. and E. Jaschke 2019. Stable asymmetric ice belts in an energy balance model of Pluto. *Icarus* 331, 15-25.

Nimmo, F., and 16 colleagues 2017. Mean radius and shape of Pluto and Charon from New Horizons images. *Icarus* 287, 12-29.

Olkin, C. B., E. F. Young, L. A. Young, W. Grundy, B. Schmitt, A. Tokunaga, T. Owen, T. Roush, and H. Terada 2007. Pluto's Spectrum from 1.0 to 4.2  $\mu\text{m}$ : Implications for Surface Properties. *The Astronomical Journal* 133, 420-431.

2130 Olkin, C. B., and 23 colleagues 2015. Evidence that Pluto's atmosphere does not collapse from occultations including the 2013 May 04 event. *Icarus* 246, 220-225.

Olkin, C. B., and 25 colleagues 2017. The Global Color of Pluto from New Horizons. *The Astronomical Journal* 154, 258.

Owen, T. C., T. L. Roush, D. P. Cruikshank, J. L. Elliot, L. A. Young, C. de Bergh, B. Schmitt, T. R. Geballe, R. H. Brown, and M. J. Bartholomew 1993. *Science* 261,745-748.

Prokhvatilov, A. L. & Yantsevich, L. D. 1983. X-ray investigations of the equilibrium phase diagram of  $\text{CH}_4\text{-N}$ , solid mixtures. *Soviet J. Low Temp Phys.* 9, 94.

Protopapa, S., H. Boehnhardt, T. M. Herbst, D. P. Cruikshank, W. M. Grundy, F. Merlin, and C. B. Olkin 2008. Surface characterization of Pluto and Charon by L and M band spectra. *Astronomy and Astrophysics* 490, 365-375.

2140 Protopapa, S., W. M. Grundy, S. C. Tegler, and J. M. Bergonio 2015. Absorption coefficients of the methane-nitrogen binary ice system: Implications for Pluto. *Icarus* 253, 179-188.

Protopapa, and 22 colleagues 2017. Pluto's global surface composition through pixel-by-pixel Hapke modeling of New Horizons Ralph/LEISA data. *Icarus* 287, 218-228.

Putzig, N. E., Thermal inertia and surface heterogeneity on Mars, Ph. D. dissertation, University of Colorado, Boulder, 2006.

Salama, F. 1998. UV Photochemistry of Ices. The Role of Photons in the Processing of Ices. In *Solar System Ices*, eds. B. Schmitt, C. de Bergh and M. Festou (Dordrecht: Kluwer), pp 259-280.

Schaefer, B. E., M. W. Buie, and L. T. Smith 2008. Pluto's light curve in 1933-1934. *Icarus* 197, 590-598.

2150 Schenk, P. M., and 19 colleagues 2018. Basins, fractures and volcanoes: Global cartography and topography of Pluto from New Horizons. *Icarus* 314, 400-433.

Schmitt, B., and 28 colleagues 2017. Physical state and distribution of materials at the surface of Pluto from New Horizons LEISA imaging spectrometer. *Icarus* 287, 229-260.

Sicardy, B., and 40 colleagues 2003. Large changes in Pluto's atmosphere as revealed by recent stellar occultations, *Nature* Vol 424, 168-170

Sicardy et al. 2016. Pluto's atmosphere from the 2015 June 29 ground-based stellar occultation at the time of the New Horizons flyby. *Astrophys. J. Lett.* Vol 819, L38

Spencer, J. R., L. A. Lebofsky, and M. V. Sykes 1989. Systematic biases in radiometric diameter determinations. *Icarus* 78, 337-354.

2160 Spencer, J. R., M. W. Buie, and G. L. Bjoraker 1990. Solid methane on Triton and Pluto: 3- to 4- $\mu$ m spectrophotometry. *Icarus* 88, 491-496.

Spencer, J. R., Stansberry, J. A., Trafton, L. M., Young, E., Binzel, R. P., Croft, S. K. 1997. Volatile transport, seasonal cycles, and atmospheric dynamics on Pluto. In *Pluto and Charon*, eds. S. A. Stern and D. Tholen (U. Arizona Press, Tucson), pp. 435-473.

Stansberry, J. A. and R. V. Yelle 1999. Emissivity and the Fate of Pluto's Atmosphere. *Icarus* 141, 299-306.

Stansberry, J. A., J. I. Lunine, W. B. Hubbard, R. V. Yelle, and D. M. Hunten 1994. Mirages and the Nature of Pluto's Atmosphere. *Icarus* 111, 503-513.

2170 Stansberry, J. A., D. J. Pisano, and R. V. Yelle 1996a. The emissivity of volatile ices on Triton and Pluto. *Planet. Space Sci.* 44, 945-955.

Stansberry, J. A., Spencer, J. R., Schmitt, B., Benchkora, A., Yelle, R. V., and Lunine, J. I. 1996b. A model for the overabundance of methane in the atmospheres of Pluto and Triton. *Planet. Spa. Sci.* 44, 1051-1063.

Stansberry, J. A., Grundy, W., & Young, L. A. 2014. The influence of topography on volatile transport 2014. 46th meeting of the AAS/DPS Society #46, id.401.08.

Stern, S. A. and L. Trafton 1984. Constraints on bulk composition, seasonal variation, and global dynamics of Pluto's atmosphere. *Icarus* 57, 231-240.

Stern, S. A. and L. M. Trafton 2008. On the Atmospheres of Objects in the Kuiper Belt. *The Solar System Beyond Neptune*, eds Barucci et al. (U. Arizona Press, Tucson) 365-380.

2180 Stern, S. A., L. M. Trafton, and G. R. Gladstone 1988. Why is Pluto bright? Implications of the albedo and lightcurve behavior of Pluto. *Icarus* 75, 485-498.

Stern, S. A., D. A. Weintraub, and M. C. Festou 1993. Evidence for a Low Surface Temperature on Pluto from Millimeter-Wave Thermal Emission Measurements. *Science* 261, 1713-1716.

Stern et al. 2015. The Pluto system: initial results from its exploration by New Horizons. *Science* Vol. 350, aad1815.

Stern, S. A., and 13 colleagues 2017. Past epochs of significantly higher pressure atmospheres on Pluto. *Icarus* 287, 47-53.

Strazulla, G. 1998. Chemistry of ice induced by bombardment with energetic charged particles. In *Solar System Ices*, eds. B. Schmitt, C. de Bergh and M. Festou (Dordrecht: Kluwer), pp 281-301.

2190 Sykes, M. V., R. M. Cutri, L. A. Lebofsky, and R. P. Binzel 1987. IRAS Serendipitous Survey Observations of Pluto and Charon. *Science* 237, 1336-1340.

Tan, S. P. and Kargel, J. S. 2018. Solid-phase equilibria on Pluto's surface, *MNRAS*, 474, 4254-4263.

Telfer, M. W., and 19 colleagues 2018. Dunes on Pluto. *Science* 360, 992-997.

Tegler et al. 2019. A new two-molecule combination band as a diagnostic of carbon monoxide diluted in nitrogen ice on Triton. *Astron. J.* 158, 17.

Toigo, A. D., R. G. French, P. J. Gierasch, S. D. Guzewich, X. Zhu, and M. I. Richardson 2015. General circulation models of the dynamics of Pluto's volatile transport on the eve of the New Horizons encounter. *Icarus* 254, 306-323.

Trafton, L. 1980. Does Pluto have a substantial atmosphere? *Icarus* 44, 53-61.

2200 Trafton, L. 1981. Pluto's atmospheric bulk near perihelion. *Advances in Space Research* 1, 93-97.

Trafton, L. M. 1984. Large seasonal variations in Triton's atmosphere. *Astrophys. J.* 359, 512-523. *Icarus*, 312-324.

Trafton, L. M. 1989. Pluto's atmosphere near perihelion. *Geophysical Research Letters* 16, 1213-1216.

Trafton, L. M. 1990. A two-component volatile atmosphere for Pluto I. The bulk hydrodynamic escape regime. *Astrophys. J.* 359, 512-523.

Trafton, L. M. 2015. On the state of methane and nitrogen ice on Pluto and Triton: Implications of the binary phase diagram. *Icarus* 246, 197-205.

Trafton, L. and S. A. Stern 1983. On the global distribution of Pluto's atmosphere. *The Astrophysical Journal* 267, 872-881.

2210 Trafton, L. M., Stern, S. A., and Gladstone, G. R. 1988. The Pluto-Charon System: The escape of Charon's primordial atmosphere. *Icarus* 74, 108-120.

Trafton, L. M., Matson, D. L., and Stansberry, J. A. 1998. Surface/atmosphere interaction and volatile transport (Triton, Pluto, and Io). In *Solar System Ices*, eds. B. Schmitt, C. de Bergh and M. Festou (Dordrecht: Kluwer), pp. 773-812.

Trafton, L. M., and Stansberry, J. A. 2015. 47th meeting of the AAS/DPS Society, #47, id.210.02.

Trafton, L. M., Tan, S., and Stansberry, J. H. 2019. On the equilibrium state of Pluto's surface ice, LPI Contributions 2133, 7070, Pluto after New Horizons Conference held at APL Laurel, MD July 14-19, 2019.

2220 Trowbridge, A. J., H. J. Melosh, J. K. Steckloff, and A. M. Freed 2016. Vigorous convection as the explanation for Pluto's polygonal terrain. *Nature* 534, 79-81.

Tryka, K. A., Brown, R. H., Anicich, V., Cruikshank, D. P., Owen, T. C. 1993. Spectroscopic determination of the phase composition and temperature of nitrogen ice on Triton, *Science*, 261, 751-754.

Tryka, K. A., Brown, R. H., Cruikshank, D. P., Owen, T. C., Geballe, T. R., and de Bergh, C.: Temperature of Nitrogen Ice on Pluto and Its Implications for Flux Measurements, *Icarus*, Vol 112, pp 513-527, 1994.

Tryka, K. A. Nitrogen on Triton and Pluto, Ph.D. thesis, California Institute of Technology. 1995.

Tucker, O. J., Erwin, J. T., Johnson, R. E., Volkov, A. N., & Cassidy, T. A. 2011. Fluid/Kinetic Hybrid Simulation of Atmospheric Escape: Pluto. AIP Conference Proceedings 1333, 1145.

2230 Vangichith, M. 2013. Modélisation des Atmosphères et des Glaces de Pluton et Triton. Ph.D. Thesis. Université Pierre et Marie Curie.

Vapillon, L., M. Combes, and J. Lecacheux 1973. The beta Scorpii occultation by Jupiter. II. The temperature and density profiles of the Jupiter upper atmosphere. *Astronomy and Astrophysics* 29, 135.

Vetter, M., H.-J. Jodl, and A. Brodyanski 2007. From optical spectra to phase diagrams—the binary mixture N<sub>2</sub>-CO. *Low Temperature Physics* 33, 1052-1060.

Volkov, A. N., Johnson, R. E., Tucker, O. J., Erwin, J. T. 2011. Thermally driven atmospheric escape: Transition to hydrodynamic to Jeans escape. *Astrophys. J. Lett.* 729, L24.

White, O. L., and 24 colleagues 2017. Geological mapping of Sputnik Planitia on Pluto. *Icarus* 287, 261-286.

2240 Young, E. F. 1993. An Albedo Map and Frost Model of Pluto. Ph.D. Thesis. Massachusetts Institute of Technology.

Young, L. A. 2012. Volatile transport on inhomogeneous surfaces: I - Analytic expressions, with application to Pluto's day. *Icarus* 221, 80-88.

Young, L. A. 2013. Pluto's Seasons: New Predictions for New Horizons. *The Astrophysical Journal* 766, L22.

Young, L. A., J. L. Elliot, A. Tokunaga, C. de Bergh, and T. Owen 1997. Detection of Gaseous Methane on Pluto. *Icarus* 127, 258-262.

Young, E. F., K. Galdamez, M. W. Buie, R. P. Binzel, and D. J. Tholen 1999. Mapping the Variegated Surface of Pluto. *The Astronomical Journal* 117, 1063-1076.

2250 Young, L. A., J. C. Cook, R. V. Yelle, and E. F. Young 2001a. Upper Limits on Gaseous CO at Pluto and Triton from High-Resolution Near-IR Spectroscopy. *Icarus* 153, 148-156.

Young, L. A., and 25 colleagues 2018. Structure and composition of Pluto's atmosphere from the New Horizons solar ultraviolet occultation. *Icarus* 300, 174-199.

Young, L. A., F. Braga-Ribas, and R. E. Johnson 2020. Volatiles evolution and atmospheres of Trans-Neptunian objects. In *The Trans-Neptunian Solar System*, eds D. Prialnik, M. Antonietta Barucci and L. A. Young (Elsevier), pp. 127-151.

Young, E. F., R. P. Binzel, and K. Crane 2001b. A Two-Color Map of Pluto's Sub-Charon Hemisphere. *The Astronomical Journal* 121, 552-561.

2260 Young, L. A., S. P. Tan, L. M. Trafton, J. A. Stansberry, W. B. Grundy, S. Protopapa, B. Schmitt, O. M. Umurhan, and T. Bertrand 2019. On the Disequilibrium of Pluto's Volatiles. Presented at Pluto System After New Horizons. LPI Contributions 2133, 7039.

Zalucha, A. M., A. A. S. Gulbis, X. Zhu, D. F. Strobel, and J. L. Elliot 2011a. An analysis of Pluto occultation light curves using an atmospheric radiative-conductive model. *Icarus* 211, 804-818.

Zalucha, A. M., X. Zhu, A. A. S. Gulbis, D. F. Strobel, and J. L. Elliot 2011b. An investigation of Pluto's troposphere using stellar occultation light curves and an atmospheric radiative-conductive-convective model. *Icarus* 214, 685-700.

Zangari, A. 2015. A meta-analysis of coordinate systems and bibliography of their use on Pluto from Charon's discovery to the present day. *Icarus* 246, 93-145.